MULTIPLE OBJECTIVE CO-OPTIMIZATION OF SWITCHED RELUCTANCE MACHINE DESIGN AND CONTROL

A Dissertation Presented for the
Doctor of Philosophy
Degree
The University of Tennessee, Knoxville

Timothy Burress
May 2023

DEDICATION

I would like to dedicate this work to my wife and children who have supported me and been accommodating through the challenges.

ACKNOWLEDGMENTS

I would like to thank my PhD Committee Chair, Dr. Leon Tolbert, for his dedication to his students and for helping me obtain my master's degree and complete my dissertation. His support has led to a significant positive impact on my career and life overall. I would also like to thank my PhD committee members Dr. Hua (Kevin) Bai, Dr. Han (Helen) Cui, and Dr. Franklin Curtis for their willingness to review my work and provide guidance for the completion of my dissertation.

This work would not have been possible without the support of my management at Oak Ridge National Laboratory (ORNL) including Jason Cook, Dr. Brian Damiano, and Dr. Brian Anderson, as well as the Educational Assistance program available to ORNL employees.

Key influences regarding motor theory, control, drive design, fabrication, assembly, setup, and testing in the early part of my career at ORNL's National Transportation Research Center include Curt Ayers, Chester Coomer, Dr. John Chiasson, Dr. Jack Lawler, Dr. John McKeever, George Ott, and Cliff White.

ABSTRACT

This dissertation includes a review of various motor types, a motivation for selecting the switched reluctance motor (SRM) as a focus of this work, a review of SRM design and control optimization methods in literature, a proposed co-optimization approach, and empirical evaluations to validate the models and proposed co-optimization methods.

The switched reluctance motor (SRM) was chosen as a focus of research based on its low cost, easy manufacturability, moderate performance and efficiency, and its potential for improvement through advanced design and control optimization. After a review of SRM design and control optimization methods in the literature, it was found that co-optimization of both SRM design and controls is not common, and key areas for improvement in methods for optimizing SRM design and control were identified. Among many things, this includes the need for computationally efficient transient models with the accuracy of FEA simulations and the need for co-optimization of both machine geometry and control methods throughout the entire operation range with multiple objectives such as torque ripple, efficiency, etc.

A modeling and optimization framework with multiple stages is proposed that includes robust transient simulators that use mappings from FEA in order to optimize SRM geometry, windings, and control conditions throughout the entire operation region with multiple objectives. These unique methods include the use of particle swarm optimization to determine current profiles for low to moderate speeds and other optimization methods to determine optimal control conditions throughout the entire operation range with consideration of various characteristics and boundary conditions such as voltage and current constraints. This multi-stage optimization process includes down-selections in two previous stages based on performance and operational characteristics at zero and maximum speed. Co-optimization of SRM design and control conditions is demonstrated as a final design is selected based on a fitness function evaluating various operational characteristics including torque ripple and efficiency throughout the torque-speed operation range. The final design was scaled, fabricated, and tested to demonstrate the viability of the proposed framework and co-optimization method.

Accuracy of the models was confirmed by comparing simulated and empirical results. Test results from operation at various torques and speeds demonstrates the effectiveness of the optimization approach throughout the entire operating range. Furthermore, test results confirm the feasibility of the proposed torque ripple minimization and efficiency maximization control schemes. A key benefit of the overall proposed approach is that a wide range of machine design parameters and control conditions can be swept, and based on the needs of an application, the designer can select the appropriate geometry, winding, and control approach based on various performance functions that consider torque ripple, efficiency, and other metrics.

TABLE OF CONTENTS

LIST OF TABLES

LIST OF FIGURES

CHAPTER ONE: INTRODUCTION

Motivation for Research

Electrified powertrains have become common in the automotive industry for many reasons including reduced emissions, diversification of energy sources for transportation, and improved performance. In recent years, many governments, manufacturers, consortiums, and other organizations have made significant commitments to promote the transition to electric vehicles. A multi-national agreement was signed in 2016 between eight major nations - Canada, China, France, Japan, Norway, Sweden, the United Kingdom and the United States (U.S.) – that pledged to increase the share of electric vehicles in government fleets [1.1]. The U.S. government owns more than 650,000 vehicles and purchases about 50,000 per year, and an executive order was issued in December 2021 to end purchases of gas-powered vehicles for use in U.S. government fleets by 2035 [1.2]. Other initiatives made by the U.S. government include incentives for customers who purchase electric vehicles and a nearly $5 billion investment in a national electric vehicle (EV) charging network [1.3]. Other nations such as Norway and China have implemented similar purchase incentives, offer discounted traffic and parking costs, and support the electrification of public transportation fleets [1.4]. These countries and many others such as Denmark, Iceland, Ireland, Israel, South Korea, Netherlands, Portugal, Scotland, Singapore, and Spain have established timelines for reaching 100 percent electrified sales, 100 percent zero-emission vehicles, and net-zero emissions.

Many automotive manufacturers have set goals to significantly increase the electrification of their product lineups over the next 10-15 years [1.5, 1.6]. BMW estimates approximately half of its global sales will be battery powered by 2030. Ford launched the F-150 Lightning in Spring 2022 that has a range of 230 miles with a base price less than $40,000 and is investing $22 billion in EV research and production capabilities through 2025. General Motors (GM) announced plans to invest $35 billion into electrification through 2025, stop selling vehicles with gas and diesel engines by 2035, and transition all models of the Cadillac brand to be fully electric by 2030. Honda intends to sell only hybrid EVs (HEVs) and EVs in Europe after 2022 and by 2030, 40 percent of its North American vehicle sales are anticipated to be powered by batteries or hydrogen fuel cells, with 2040 being targeted for all Honda vehicles being fully electric. Hyundai announced that it would invest $7.4 billion through 2025 to produce EVs in the U.S. and plans to broadly expand its HEV and EV product line through the 2020's, including some fuel cell-based powertrains. Jaguar Land Rover, Mazda, and Mercedes-Benz anticipate having battery electric versions of all their models by 2030, with a significant pledge by Mercedes-Benz to invest $47 billion into electrification through 2030. Nissan has been one of the early leaders in the EV market with the Nissan LEAF and plans to have eight EVs by the end of 2023. Stellantis (formerly Fiat Chrysler) plans to invest $35.5 billion in EV's through 2025, with an all-electric Ram 1500 and performance car planned for release in 2024. Toyota has sold more than 18 million hybrids and plug-in hybrids since 1997 [1.7] and plans to have 70 electrified models by 2025 with 15 of those being battery EVs. Volkswagen announced an investment of $86 billion into electrification through 2025, and by 2030 anticipates EVs reaching 70 percent of its sales in Europe and 50 percent of its sales in the U.S. and China. Volvo projects that half of its global sales will be fully electric by 2025, and plans to for all powertrains to be electric by 2030.

In addition to being used for vehicle propulsion, electric machines are implemented in secondary systems such as power steering assist, air conditioning compressors, and oil pumps, and the number of electric machines on modern vehicles has increased significantly, even on platforms without hybrid or electric powertrains [1.8-1.9]. Many electric machines in HEV and EV powertrains function as both a motor and generator, and in this context, electric machines may be referred to as electric motors since this is the most commonly used term used for electric machines.

Almost all mass-produced HEVs and EVs have permanent magnet (PM) motors with Neodymium Iron Boron (NdFeB) magnets [1.10-1.12]. Although these magnets have the compound formula, "NdFeB", the actual molecular formula is $BFe_{14}Nd_2$. Other rare-earth elements such as Dysprosium (Dy) are added to improve resistance to corrosion, and more importantly, to improve performance at elevated temperatures and to reduce sensitivity to demagnetization, also known as coercivity. Research on alternatives [1.13-1.14] to rare-earth permanent magnet (PM) motors indicates that they are not easily surpassed in terms of efficiency, power density, and specific power. Therefore, almost all HEVs and EVs use them. However, the cost of rare-earth PM material accounts for at least 30% of the entire motor cost [1.15] and in the past 10-15 years, there has been volatility in the price and availability of rare-earth materials like neodymium, dysprosium, and praseodymium that are used in PM motors. As a result, there have been significant efforts made by automotive manufacturers and researchers in seeking motor technologies without rare-earth permanent magnets that facilitate cost stability and effectiveness as HEV and EV markets continue to expand [1.16-1.18].

High grade NdFeB magnets are often used for hybrid and electric vehicle propulsion motors, and they can contain between about 8.5 and 11% Dy by mass [1.19]. The trend of rare earth magnet raw material price is generally considered to be comprised of Praseodymium Neodymium (PrNd) mischmetal, DyFe alloy, and Terbium (Tb) metal price trends, as shown in Figure 1.1 [1.20] for a time period between 2009 and 2022. Significant price increases occurred in 2011, as DyFe prices reached over $2,000 per kg and PrNd prices reached about $240 per kg. The selling price of DyFe increased by more than a factor of 20, while PrNd prices increased by a factor of 10 in about a 1.5-year span. Although prices reduced and stabilized by 2015, they stabilized at relatively higher values when compared to levels prior to 2011. Prices of PrNd steadily increased beginning in 2020, and reached over $200 per kg in March 2022, near the peak levels in 2011. Considering these pricing trends, implications of price volatility can be realized when considering the Toyota Prius and Nissan LEAF total motor magnet mass of 0.8 and 1.9 kg [1.21], respectively. Using quantities for the Nissan LEAF and assuming 8% Dy, raw magnet material costs are roughly $105 versus $745 when using prices in 2015 versus peak prices in 2011, respectively. This raw material cost does not include the cost of processing, sintering, grinding, and installation of the magnets in the motor. Efforts are being made to reduce the amount of Dy in high grade NdFeB magnets. For example, a new grain boundary diffusion process is being used to reduce the amount of Dy by 30-40% while maintaining the same coercivity [1.22].

Other types of PMs are being researched, such as AlNiCo and ferrites, which have low energy products, and consequently, they are challenging candidates for use in high power density traction drives. Using magnets with lower coercivity requires thicker magnets to avoid demagnetization [1.23]. Therefore, power density and mechanical integrity are a challenge with low coercivity magnets because more magnet volume and mass is required, and the structure for retaining magnets is often more complex [1.24-1.25] as speed limitations are reached more readily than with

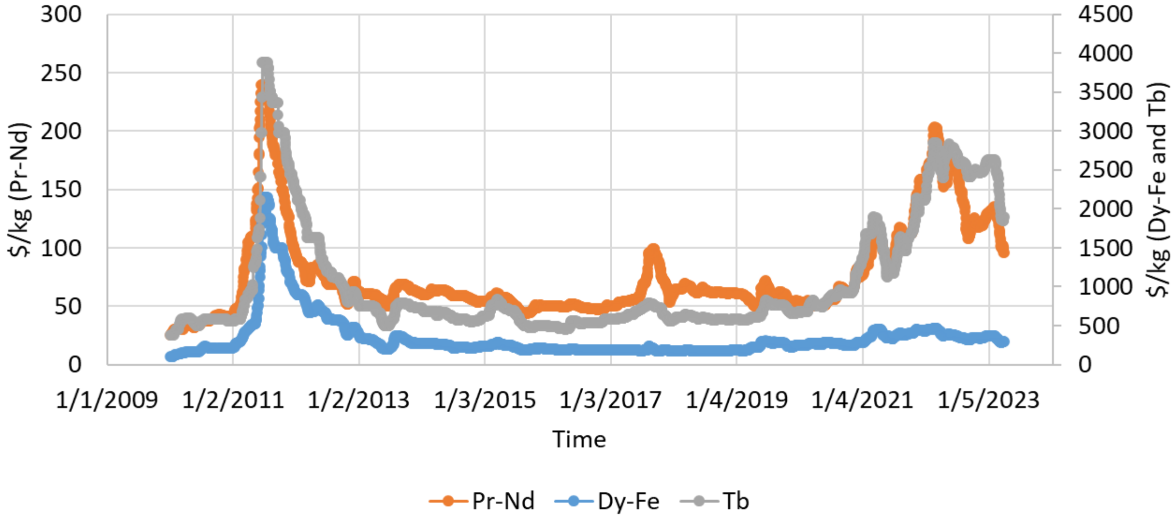

Figure 1.1 Selling price of rare-earth materials between October 2009 and April 2022 [1.20].

magnets with higher coercivity and lower size and mass. Samarium Cobalt magnets have the highest coercivity and energy product of all the NdFeB magnet alternatives, but when compared to NdFeB, they only have about 50-75% of the performance with only a slight cost advantage [1.26].

While the primary motivation for non-PM motors is the high and unstable price of rare-earth materials, there are other negative aspects related to the operation of PM motors. For variable speed and variable load applications like EV and HEV propulsion, the residual induction of the PMs yields a disadvantage in terms of core losses, since the magnitude of the rotating flux density in the stator is always present even if no current is applied [1.27]. The same residual induction of the PMs results in challenges with back-EMF, as field weakening or voltage phase advance is required to drive current in the windings at high speeds [1.28]. Therefore, PM motor operation at low and moderate loads and high speeds can result in lower efficiencies than other alternatives that do not have residual magnetic fields from PMs [1.29]. Another issue associated with back-EMF is the fault mode of powertrains in which the electric motor is always connected to the drive wheels. In the event of a winding or converter failure on platforms that have the drive motor directly linked to the drive train, induced back-EMF voltage can act as an energy source until the vehicle comes to a stop, and this can lead to worse fault conditions due to uncontrolled current in the windings.

Alternatives to Rare-Earth PM Motors and their Drive Requirements

Induction motors have been used in industrial applications for over a century. They produce torque as currents in the stator windings react with the magnetic field created by rotor currents, which are induced as a result of the rotor not being synchronized with the rotating stator magnetic field. Due to the asynchronous relationship between the rotating magnetic fields of the stator and rotor of an induction motor, more core losses are typically generated in the rotor versus synchronous motors [1.30]. Resistive losses associated with current in the rotor conductors further inhibit the potential of the induction motor to achieve high efficiencies [1.31]. Industrial motors rated for high efficiency typically involve the use of more copper in the stator windings, and/or more material (aluminum or copper) in the rotor to reduce the resistance of the rotor bars [1.32]. This often increases the volume and cost of the motor, and peak efficiencies are typically below 94% [1.33] (for motors sized for vehicle propulsion), and efficiencies are relatively low at low and moderate speeds and load levels. While induction motors are a valid solution for vehicle propulsion, they generally have greater manufacturing complexities and lower efficiencies when compared to other motor types. Rotor conductors are typically made by either die casting or brazing bar conductors, and both approaches involve specialized manufacturing processes to ensure reliability at high-speed operation. Requirements associated with the retention of rotor bars during rotation and for differing coefficients of thermal expansion also introduce mechanical limitations and reliability issues. Fully electric vehicles facilitate the ability to achieve acceptable efficiencies with induction motors, as the motors can be made larger since space is not as limited due to the absence of the combustion engine. While more copper mass is generally required for higher efficiency operation, the price of copper is much more stable relative to rare earth magnet prices.

Switched reluctance machines (SRMs) are often reported to have higher efficiency and power density than induction motors since there are no rotor conductor losses, but high torque ripple and acoustic noise levels are inherent negative characteristics associated with the fundamental way torque is produced [1.34-1.35] in a SRM. A conventional SRM geometry with 12 stator poles and 8 rotor poles is shown in Figure 1.2 (a). Torque ripple arises from the transition of torque production from one set of active stator teeth to the next. Automotive manufacturers have invested significant resources to decrease vibration and acoustic noise levels generated from conventional vehicles with combustion engines, and therefore there is concern regarding the utilization of an electric motor which adds additional challenges in these areas. Even the low torque ripple levels of a PM motor are studied and mitigated [1.36], as vibrations are transferred throughout various transmission components and ultimately to the passenger. The reduction of torque ripple in SRMs has been a key focus of research since the beginning of their commercial viability.

Another challenge for the implementation of SRMs is that they require unconventional power electronic converters/drives, as opposed to conventional variable frequency inverters that are used for PM motors and induction motors. The most commonly used type of converter is an asymmetrical half-bridge converter, as shown on the right in Figure 1.2. Although power modules

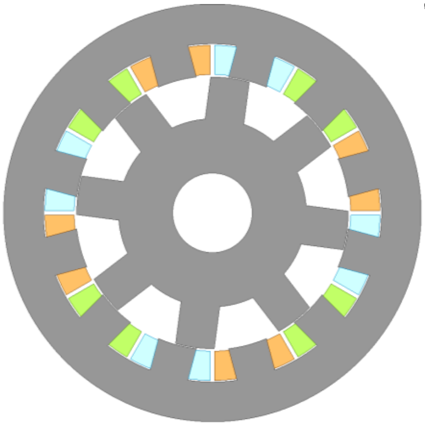

(a)

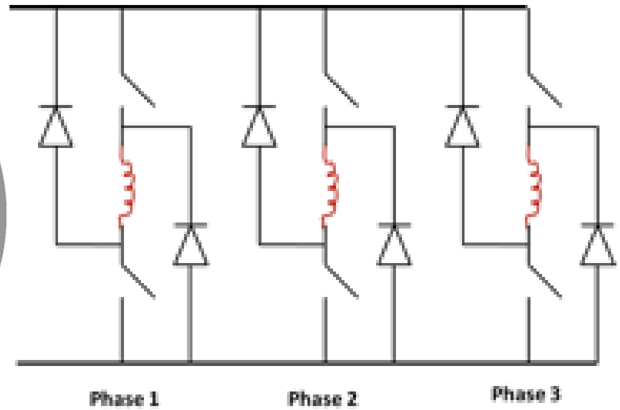

(b)

Figure 1.2 (a) SRM with 12 stator poles and 8 rotor poles and (b) asymmetrical half-bridge 3-phase SRM inverter.

with this configuration are not widely commercially available, only 2 switches and 2 diodes are required per phase for unidirectional current flow, so device and module costs in large custom productions would be similar to that of a conventional inverter. In comparison to drives for other motor types, slightly larger DC link capacitances and power devices are typically required to protect the battery from current ripple and harmonics associated with the transient nature of SRM operation [1.37]. Additionally, the control of SRMs can be quite challenging and may require current sensors and position sensors with higher bandwidths [1.38] compared to that of a PM machine with an equivalent speed range. Nonetheless, while these challenges inhibit prototyping, many of these issues can be mitigated prior to mass production, where the cost of unconventional converter and controller development becomes less significant. Since SRM rotors are not complex and do not need to retain magnets or conductors, they have outstanding mechanical integrity and greatly facilitate high-speed operation, which can be particularly effective in increasing power density [1.39, 1.40]. The inherent torque ripple and acoustic noise of the SRM may hinder integration in small and medium sized passenger vehicles, but these characteristics may be less of a concern in other platforms and applications such as large passenger and freight vehicles, off-road machinery, and small economic vehicles with low-cost powertrains.

Synchronous reluctance motors are quite different from SRMs and have the advantage of utilizing a conventional variable frequency inverter, and within the past decade, industrial motor manufacturers started marketing synchronous reluctance motor solutions which are purportedly more efficient than induction motors of the same size and application [1.41]. SRMs also operate synchronously, and could be referred to as synchronous reluctance, but the transient nature of the SRM control scheme is quite different than controls for the relatively smooth and balanced rotating field of most synchronous reluctance motors. A primary drawback of synchronous reluctance motors is the inferior mechanical integrity of the rotor, which limits maximum operating speed, and therefore reduces opportunities for power density improvements [1.42-1.44]. The rotor must be designed to guide the magnetic field with maximum magnetic saliency, and this typically involves large openings within axially stacked lamination stampings, or complicated mounting techniques for laminations that are stacked radially [1.45], such as those shown in Figure 1.3 [1.46]. Stray magnetic flux across these members results in a lower saliency ratio, and therefore lower torque capability, when compared to a similarly sized SRM.

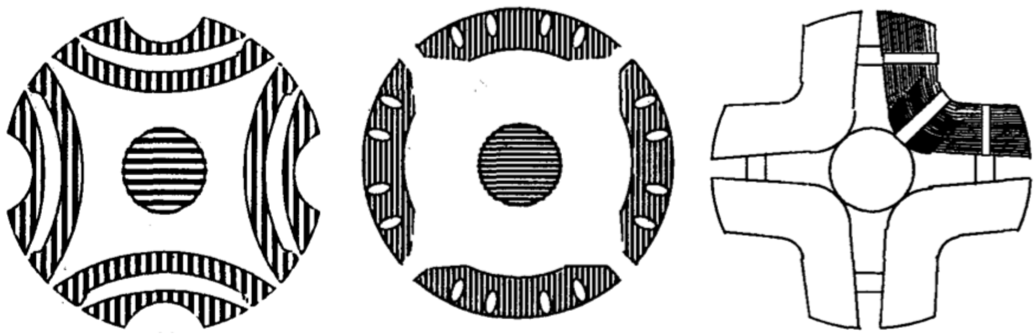

(a) (b) (c)

Figure 1.3 Synchronous reluctance rotors: (a) lamination with flux barriers, (b) isolated segmental lamination, and (c) axial laminations (right) [1.39].

Synchronous reluctance torque is a considerable contributor to the overall torque in most interior PM motors used in EVs and HEVs today. One advantage of the synchronous reluctance motor rotor is that weak non-rare earth magnets can be used in the rotor without subjecting them to magnetic fields that would otherwise demagnetize them in conventional PM motor arrangements. Some Chevrolet Volt designs include a generator with a ferrite magnet assisted synchronous reluctance motor [1.47]. Full optimization of these types of motors can be difficult since many geometric features are present in the design. Additionally, a multi-physics simulation approach that includes detailed mechanical stress analysis is required since there is a key tradeoff between mechanical integrity and magnetic performance [1.48]. For example, small support pieces are often required in locations that contribute to lower inductance and saliency ratios, and therefore lower reluctance torque capability. Some comparisons [1.49] show that the peak efficiency of a synchronous reluctance motor is 3-5% higher than a similarly sized induction motor, but 3-5% lower than a PM motor. Recent research efforts on synchronous reluctance motors have been aimed at improving efficiency and reducing the torque ripple [1.50-1.52]. Since the tractive effort of this type of motor is based on reluctance torque, it is susceptible to torque ripple, but typically not at the magnitude of SRMs.

Brushless field excitation (BFE) techniques have been used to supplement weak non-rare earth PMs or to serve as a replacement for a magnetic field source in designs that do not use PM material. This technique has been applied to various types of motors and is typically achieved by either supplying additional flux directly from a stationary coil, or using a receiving coil, rectifier, and windings located on the rotor. The former commonly involves complex magnetic flux paths and additional air gaps, as shown in Figure 1.4 [1.53]. In many cases, these features of the magnetic circuit can lead to an increase of stray paths for magnetic flux, and therefore inhibit the capability to achieve high efficiency and power density, particularly when losses and size of the coil are considered. It is common for these types of motors to require materials with the capability to transfer flux in three-dimensions. These materials, such as soft-magnetic composites (SMCs), typically reach magnetic saturation at a low flux density, and have higher core losses than electrical steel for low frequencies.

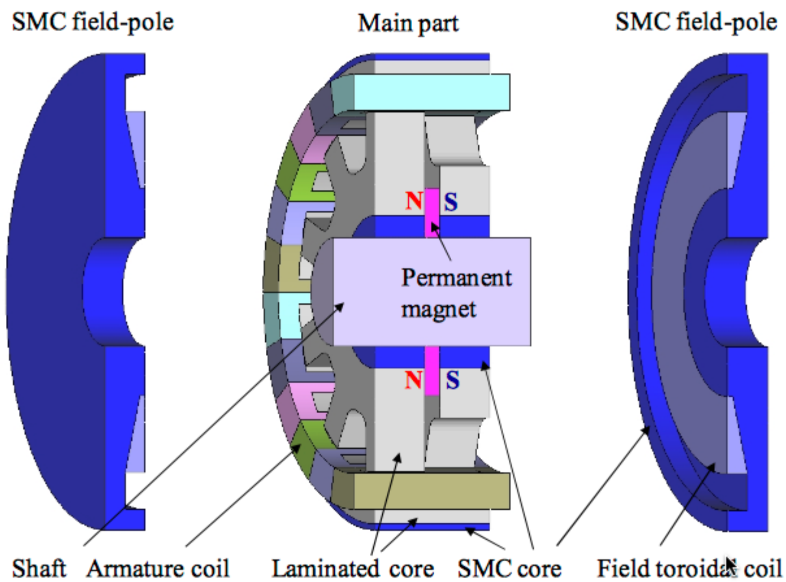

Figure 1.4 Example of BFE motor [1.46].

In most cases, brushless field excitation (BFE) techniques allow for variable control of the magnetic field, which has some advantages in comparison to the residual magnetic field generated by PMs. Research has shown that this field control facilitates the possibility to eliminate or mitigate field-weakening control requirements and therefore can yield a broad range of high efficiency operation [1.54]. The additional volume, cost, and power loss of transmission coils, receiver coils, controls, and electronics when targeting power density, efficiency, and cost metrics are a key consideration for the viability of this approach. Furthermore, the wound-field rotor approach has the additional challenge of reliability concerns for coils and electronics that rotate, resulting in considerable speed limitations. While there are challenges with both BFE techniques, they have potential for vehicle propulsion applications, especially since they can be applied to various types of motors.

There has recently been a considerable amount of research into flux-switching motors (FSMs) and examples of FSM configurations are shown in Figure 1.5 [1.55]. FSMs typically have a simple rotor that is similar to that of SRMs, and PMs in the stator, as indicated by a green color. A key advantage of this motor type is that this configuration allows for large magnets to be incorporated into the design without concern for retaining rotating magnets. Additionally, the applied magnetic field is in the same direction of the PM magnetic field, whereas conventional PM motors involve the application of a field that opposes the PM field in the rotor. Therefore, PMs in this configuration are less susceptible to demagnetization, and the use of non-rare-earth magnets such as AlNiCo, Ferrites, and Dy-free NdFeB is greatly facilitated. Recent publications [1.56] indicate that an efficiency above 94% is possible, which is very close to conventional IPM motor peak efficiencies. However, these designs used high efficiency steel and very thin laminations because FSMs have inherently high fundamental electrical frequencies. For example, the designs shown in Figure 1.5 have 14 and 10 rotor poles, and based on the operation of the motor, this is equivalent to the number of pole pairs in a conventional PM motor. Most PM motors in EV and HEVs have 4-6 pole pairs. Therefore, this motor not only inherently has a large amount of core losses, but requirements of the inverter are also similar to that of an SRM. High frequency power electronics and controller bandwidths are typically required for this type of motor, and this may hinder acceptability in applications with power levels above 30kW. For example, the 14-pole and 10-

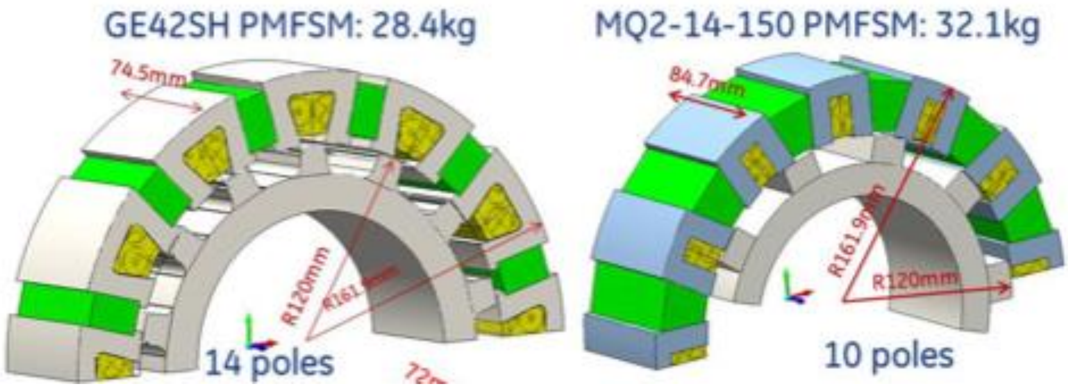

Figure 1.5 Example of flux-switching motors [1.48].

pole designs shown below have fundamental electrical frequencies of about 1.4 kHz and 1.0 kHz, respectively, for operation at 6,000 rpm.

Summary

Governments, automotive manufacturers, consortiums, and other organizations have recently made strong commitments regarding the pursuit of passenger vehicle electrification, and many are targeting the 2030's for the total elimination of gasoline and diesel powertrains. Most of the largest automotive manufacturers have announced plans for significant investments in research and product development as well as production facilities for HEVs and EVs. Nearly all HEV and EV powertrains currently use PM motors with neodymium magnets, but recent price trends, volatility, and growing demand result in concern for cost stability as 100 percent electrification is being targeted in 10-15 years.

A brief assessment of alternatives to rare-earth PM motors was conducted for motor types that are commonly researched by leading organizations and academic institutions. A comparison of the characteristics and parameters of various electric motors is provided in Table 1.1. Of all the alternatives, it is difficult to achieve the same power density, specific power, and efficiency as a PM motor. Induction motors have complicated manufacturing processes, moderate efficiency, and limited operation speed associated with rotor bars. Synchronous reluctance motors have considerable geometric complexities that lead to challenges in modeling, design optimization, and mechanical robustness. BFE approaches offer additional operational capability and potential net-efficiency improvements, but the size, cost, and reliability of additional excitation components may negate these advantages. SRMs have very low cost, moderate efficiency, and excellent mechanical robustness, but have inherent torque ripple, acoustic noise, and controller complexity that is the focus of most SRM research. SRMs and some FSMs require unconventional inverter configurations. Some FSMs may utilize conventional inverter configurations, but often require higher switching frequencies relative to PM or synchronous reluctance counterparts.

Thesis Objectives and Outline

While the SRM is not the ideal solution for all applications, its simplicity, robustness, and low cost make it a viable solution for some powertrain and ancillary needs. This work is fully applicable to various applications such as vehicle propulsion, residential appliances, industrial processes, oil

Table 1.1 Comparison of various motor technologies.

	Rare Earth Permanent Magnet Motor	**Induction Motor**	**Switched Reluctance Motor**	**Synchronous Reluctance**	**Flux Switching**
Cost ($/kW)	$$$	$$	$	$$	$$
Power density (kW/L)	Highest	Moderate	Moderate	Moderate	Moderate
Specific power (kW/kg)	Highest	Moderate	Moderate	Moderate	Moderate
Efficiency (%)	High	Low	Good	Good	Good
Noise and vibration	Good	Good	Challenging	Good	Challenging
Manufactura bility	Mature	Mature	Easy	Moderate	Difficult
Inverter and Controls Requirements	Conventional	Conventional	Unconven.	Conventional	Unconven.
Potential for improvement for automotive applications	Moderate	Minimal	Significant	Significant	Significant

extraction/processing, earth moving equipment, and electrified agricultural equipment and implements. The focus of this dissertation proposal is on the establishment and demonstration of a design framework for co-optimization of geometric features, windings, and control of SRM that minimize torque ripple and maximize efficiency.

Fundamentals of SRM design, operation, and control methods are discussed in Chapter 2 along with a detailed review of new and advanced design and control optimization methods. A novel optimization and modeling approach is presented in Chapter 3 that uses a unique method to perform co-optimization of both SRM design and control by determining control conditions at low and high speeds without extensive FEA time domain simulations. In Chapter 4, this SRM optimization technique is implemented with consideration of the entire torque-speed operation range as a detailed design process is proposed and demonstrated and a final design is selected for testing. In Chapter 5, the process of scaling, fabricating, and testing the final design is discussed. A summary and conclusions are provided in Chapter 6 along with a discussion of the applicability and limitations of the proposed design and control co-optimization method.

References

[1.1] International Energy Agency, (2022, March 22), "Electric Vehicles Initiative", https://www.iea.org/areas-of-work/programmes-and-partnerships/electric-vehicles-initiative.

[1.2] D. Shepardson and B. Klayman, Reuters, (2021, December 8), "U.S. government to end gas-powered vehicle purchases by 2035 under Biden order", https://www.reuters.com/world/us/biden-pledges-end-gas-powered-federal-vehicle-purchases-by-2035-2021-12-08/.

[1.3] Department of Energy, (2022, February 10), "President Biden, DOE and DOT Announce $5 Billion over Five Years for National EV Charging Network", https://www.energy.gov/articles/president-biden-doe-and-dot-announce-5-billion-over-five-years-national-ev-charging.

[1.4] International Energy Agency, (2021), "Global EV Outlook 2021", Paris, https://www.iea.org/reports/global-ev-outlook-2021/policies-to-promote-electric-vehicle-deployment.

[1.5] A. White, Car and Driver, (2021, June 26), "Here are All the Promises Automakers Have Made about Electric Cars", https://www.caranddriver.com/news/g35562831/ev-plans-automakers-timeline/.

[1.6] J. Motavalli, Forbes, (2021, October 4), "Every Automaker's EV Plans Through 2035 and Beyond", https://www.forbes.com/wheels/news/automaker-ev-plans/.

[1.7] J. O'Dell, Forbes, (2021, November 17), "2023 Toyota bZ4X Kicks Off the Company's Electrical Parade", https://www.forbes.com/wheels/news/2023-toyota-bz4x/.

[1.8] "Hybrid Electric and Electric Cars - Electromobility driven by Semiconductor Innovations", Infineon Technologies AG, 2014.

[1.9] S. Constantinides, "Rare Earth Elements in Transportation", Arnold Magnetic Technologies, 2013.

[1.10] T. Burress, et. al., "Evaluation of the 2010 Toyota Prius Hybrid Synergy Drive System", ORNL/TM-2010/253.

[1.11] T. Burress, "Evaluation of the 2008 Lexus LS 600h Hybrid Synergy Drive System", ORNL/TM-2008/185.

[1.12] T. Burress, "Evaluation of the 2007 Toyota Camry Hybrid Synergy Drive System", ORNL/TM-2007/190.

[1.13] K. Kiyota, H. Sugimoto, and A. Chiba, "Comparing electric motors: An analysis using four standard driving schedules," *IEEE Ind. Appl. Mag.*, vol. 20, no. 4, pp. 12–20, Jul./Aug. 2014.

[1.14] D. G. Dorrell, A. M. Knight, M. Popescu, L. Evans, and D. A. Staton, "Comparison of different motor design drives for hybrid electric vehicles," in *Proc. IEEE ECCE*, Sep. 2010, pp. 3352–3359.

[1.15] P. Campbell, “System Cost Analysis for an Interior Permanent Magnet Motor”, AMES Laboratory, 2008.

[1.16] S. Constantinides, “The Demand for Rare Earth Materials in Permanent Magnets”, Arnold Magnetic Technologies, 2015.

[1.17] M. Rahman, “Status Review of Advances in Hybrid Electric Vehicles”, *IEEE PES General Meeting*, 2014.

[1.18] Nakada, T., Ishikawa, S., and Oki, S., "Development of an Electric Motor for a Newly Developed Electric Vehicle," *SAE Technical Paper 2014-01-1879*, 2014, doi:10.4271/2014-01-1879.

[1.19] S. Constantinides, “The Important Role of Dysprosium in Modern Permanent Magnets”, Arnold Magnetic Technologies, 2012.

[1.20] SDM Magnetics website, “https://www.magnet-sdm.com/raw-material-price-trend/”, accessed April 28, 2022

[1.21] T. Burress, “Benchmarking EV and HEV Technologies”, FY14 DOE Vehicle Technologies Kickoff Meeting, 2013.

[1.22] K. Hirota, et. al., “Coercivity enhancement by the grain boundary diffusion process to Nd–Fe–B sintered magnets,” *IEEE Trans. Magn*., vol. 42, no. 10, pp. 2909–2911, Oct. 2006.

[1.23] L. Ferarris, “PM fractional machines adopting bonded magnets: Effect of different magnetizations on the energetic performance”, *IEEE ENERGYCON Conference & Exhibition*, 2012.

[1.24] “Permanent Magnets Materials and Magnet Systems”, IBS Magnet, www.ibsmagnet.com, 2007.

[1.25] “Magnet Guide and Tutorial”, Alliance LLC, https://studylib.net/doc/8298999/magnet-guide-and-tutorial, 2009.

[1.26] S. Constantinides, “Measurement and Evaluation of (Neodymium-Iron-Boron) Magnets”, Magnetics 2007.

[1.27] T. Jahns, "Interior permanent magnet synchronous motors for adjustable-speed drives," *IEEE Trans. Ind. Appl.*, vol. IA-22, pp. 738-747, July/Aug. 1986.

[1.28] T. M. Jahns, “Flux-weakening regime operation of an interior permanent magnet synchronous motor drive*”, IEEE trans. on Ind. Appl*, vol. IA-23. pp.681-689, 1987.

[1.29] J. S. Hsu, et. al., “16,000-rpm Interior Permanent Magnet Reluctance Machine with Brushless Field Excitation,” ORNL/TM-2007/167, Oak Ridge National Laboratory, Oak Ridge, Tennessee, 2007.

[1.30] I. Boldea, "Automotive Electric Propulsion Systems with Reduced or No Permanent Magnets: An Overview", *IEEE Transactions on Industrial Electronics*, VOL. 61, NO. 10, OCTOBER 2014.

[1.31] D. G. Dorrell, A. M. Knight, M. Popescu, L. Evans, and D. A. Staton, "Comparison of different motor design drives for hybrid electric vehicles," *in Proc. IEEE ECCE*, Sep. 2010, pp. 3352–3359.

[1.32] "Introduction to Premium Efficiency Motors", www.copper.org, July 2015.

[1.33] C. Shumei, L. Chen, S. Liwei, "Study on efficiency calculation model of induction motors for electric vehicles," *Vehicle Power and Propulsion Conf.*, Harbin, 2008, pp.: 1-5.

[1.34] T.J.E. Miller, "Switched Reluctance Motors and Their Control", Magna Physics Publishing, 1993.

[1.35] R. Krishnan, "Switched Reluctance Motor Drives: Modeling, Simulation, Analysis, Design, and Applications", CRC Press, 2001.

[1.36] Z. Azar, Z. Q. Zhu, and G. Ombach, "Influence of electric loading and magnetic saturation on cogging torque, back-EMF and torque ripple of PM machines," *IEEE Trans. Magn.*, vol. 48, no. 10, pp. 2650–2658, Oct. 2012,

[1.37] W. Suppharangsan and J. Wang, "Experimental validation of a new switching technique for DC-link capacitor minimization in switched reluctance machine drives," *International Electric Machines & Drives Conference (IEMDC)*, 013 IEEE International, 2013, pp. 1031-1036.

[1.38] L. Zhengyu, S.R. Donald, W.W. Barry, and H. Xiangning, "*Torque ripple reduction in switched reluctance motor drives using B-Spline neural networks*," *IEEE Trans. Industry Appl.*, Vol. 42, No. 6, Nov./Dec. 2006.

[1.39] T. Nonaka, "Inverter Improving Motor Efficiency of Switched Reluctance Motor for Electric Vehicle", *Power Electronics and Applications (EPE)*, 2013.

[1.40] J. Kim, "Non-Linear Calculation of High-Power Density and High-Speed Permanent Magnet DC Motor Including Demagnetization Effects", *Electromagnetic Field Computation*, 2006.

[1.41] "Synchronous reluctance motor-drive package for machine builders", https://library.abb.com, May 2023.

[1.42] T. A. Lipo, T. J. Miller, A. Vagati, I. Boldea, L. Malesani, and T. Fukao, "Synchronous reluctance drives," *Tutorial Presented at IEEE IAS Annual Meeting*, Denver, Co, Oct. 1994.

[1.43] S. Taghavi, “A Mechanically Robust Rotor with Transverse-Laminations for a Wide Speed Range Synchronous Reluctance Traction Motor”, *IEEE Transactions on Industry Applications*, 2015.

[1.44] M. Palmieri, “High-speed scalability of synchronous reluctance machines considering different lamination materials”, *Industrial Electronics Society*, IECON 2014.

[1.45] X. Feng, “Reluctance motor with a radially-laminated rotor using anisotropic material”, *Electrical Machines and Drives*, 1993.

[1.46] Matsuo, T.; Lipo, T.A. "*Rotor design optimization of synchronous reluctance machine*”, *IEEE Transactions on Energy Conversion*, On page(s): 359 - 365 Volume: 9, Issue: 2, Jun 1994.

[1.47] S. Jurkovic, K. Rahman, B. Bae, N. Patel and P. Savagian, "Next generation chevy volt electric machines; design, optimization and control for performance and rare-earth mitigation," *2015 IEEE Energy Conversion Congress and Exposition (ECCE)*, Montreal, QC, Canada, 2015, pp. 5219-5226, doi: 10.1109/ECCE.2015.7310394.

[1.48] Y. Wang, D. M. Ionel and D. Staton, "Ultrafast steady-state multi-physics model for PM and synchronous reluctance machines," *2014 IEEE Energy Conversion Congress and Exposition (ECCE)*, Pittsburgh, PA, USA, 2014, pp. 5152-5159, doi: 10.1109/ECCE.2014.6954108.

[1.49] R. Vartanian, Y. Deshpande and H. A. Toliyat, "Performance analysis of a rare earth magnet based NEMA frame Permanent Magnet assisted Synchronous Reluctance Machine with different magnet type and quantity," *2013 International Electric Machines & Drives Conference*, Chicago, IL, USA, 2013, pp. 476-483, doi: 10.1109/IEMDC.2013.6556139.

[1.50] S. Yamamoto, H. Hirahara, A. Tanaka, T. Ara and K. Matsuse, "Maximum efficiency drives of Synchronous Reluctance Motors with on-line stator resistance estimator," *2013 IEEE Energy Conversion Congress and Exposition*, Denver, CO, USA, 2013, pp. 3140-3145, doi: 10.1109/ECCE.2013.6647111.

[1.51] Bomela, X.B.; Kamper, M.J. "Effect of stator chording and rotor skewing on average torque and torque ripple of reluctance synchronous machine”, *Africon, 1999 IEEE*, On page(s): 687 - 690 vol.2 Volume: 2, 1999.

[1.52] R. -R. Moghaddam, F. Magnussen and C. Sadarangani, "Novel rotor design optimization of Synchronous Reluctance Machine for low torque ripple," *2012 International Conference on Electrical Machines*, Marseille, France, 2012, pp. 720-724, doi: 10.1109/ICElMach.2012.6349952.

[1.53] T. Kosaka, T. Hirose and N. Matsui, "Brushless synchronous machines with wound-field excitation using SMC core designed for HEV drives," *The 2010 International Power Electronics Conference - ECCE ASIA*, Sapporo, Japan, 2010, pp. 1794-1800, doi: 10.1109/IPEC.2010.5543569.

[1.54] J. S. Hsu et al., "16,000-RPM Interior Permanent Magnet Reluctance Machine with Brushless Field Excitation," *2008 IEEE Industry Applications Society Annual Meeting*, Edmonton, AB, Canada, 2008, pp. 1-6, doi: 10.1109/08IAS.2008.67.

[1.55] T. Raminosoa et al., "Reduced Rare-Earth Flux-Switching Machines for Traction Applications," *in IEEE Transactions on Industry Applications*, vol. 51, no. 4, pp. 2959-2971, July-Aug. 2015, doi: 10.1109/TIA.2015.2397173.

[1.56] X. Liu, D. Wu, Z. Q. Zhu, A. Pride, R. P. Deodhar and T. Sasaki, "Efficiency Improvement of Switched Flux PM Memory Machine Over Interior PM Machine for EV/HEV Applications," *in IEEE Transactions on Magnetics*, vol. 50, no. 11, pp. 1-4, Nov. 2014, Art no. 8202104, doi: 10.1109/TMAG.2014.2323556.

CHAPTER TWO: FUNDAMENTALS OF SRMS, CONVERTERS, AND CONTROL METHODS

Abstract

After a brief historical background of the SRM is provided, fundamentals of SRM operation including the physical principles on which it operates, basic equations, converter topologies, and control techniques are discussed. A review of both new and well established methods for design and control optimization is given, and the deficiencies of existing methods are identified.

SRM History and Usage

The SRM dates to the 19th century and its first documented use was for locomotive propulsion in Scotland in 1838. To achieve reasonable performance, SRMs must have position and speed dependent commutation and current regulation. Therefore, the SRM only began to be a viable motor technology in the late 1970s and 1980s when microprocessors and power electronics started becoming commercially available. Due to their simple construction, SRMs have been used in a wide range of low-cost applications such as vending machine dispensers and parking brake engagement for passenger vehicles. Since SRM rotors do not contain magnets or windings, they have the simplest construction and are the most mechanically robust of all electric machines, and this facilitated their use in high-speed applications such as commercial hand dryers and vacuum cleaners. Furthermore, due to the ability of many SRM configurations to continue to operate with a fault in one of the phases, they have been used in rugged applications such as agriculture, mining, earth moving, or deep-well drilling where there is a need for the machine to continue to operate after a phase fault occurs.

Fundamentals of SRM Operation

Torque production in SRMs is based on reluctance torque which is developed by magnetically salient teeth made of soft-magnetic material on both the rotor and the stator. The magnitude of the torque is directly related to magnetic saliency, and stator teeth are energized to attract the nearest rotor tooth, and they must be de-energized upon alignment to avoid negative torque. Conventional SRM windings are referred to as concentrated windings, as each stator pole is formed by a single coil wrapped around a single stator tooth, as opposed to distributed windings that are common in multi-phase machines, which span multiple teeth to form a stator pole. An example of an SRM with 12 stator teeth and 8 rotor poles (referred to as 12-8) is provided in Figure 2.1. Three rotor positions are shown beginning with the four stator teeth and orange windings of phase ‘a’ being unaligned with the rotor teeth. With the positive angular speed defined to be in the counterclockwise direction, current applied to phase ‘c’, indicated by the blue windings, produces positive torque at this position. As rotor position increments counterclockwise from the unaligned position shown in Figure 2.1(a), phase ‘a’ current produces positive torque until the rotor teeth are in alignment with the stator teeth of phase ‘a’ as shown in Figure 2.1(c). An intermediate position is shown in Figure 2.1(b) where stator and rotor teeth corresponding to phase ‘a’ are overlapping and positive torque is being produced by phase ‘a’, but rotor teeth corresponding with phase ‘c’ are past alignment and negative torque is produced by phase ‘c’ if current is applied.

Torque production and operational characteristics of the SRM can be derived by applying Faraday’s law. If mutual coupling between phases is neglected, the phase voltage can be expressed by

$$\begin{aligned} v &= Ri + \frac{d\psi(i,\theta)}{dt} \\ &= Ri + \frac{d\psi}{di}\cdot\frac{di}{dt} + \frac{d\psi}{d\theta}\cdot\frac{d\theta}{dt} \qquad (2.1) \\ &= Ri + L_{inc}\cdot\frac{di}{dt} + e\cdot\omega \end{aligned}$$

where i is the current, R is the resistance, ψ is the flux linkage, and L_{inc} is the incremental inductance associated with coils in a phase. Angular position and angular speed are represented by theta and omega, respectively. In the last term, e represents what is referred to as the pseudo back-emf. Flux linkage and L_{inc} are dependent on both phase current and rotor position. An example of flux linkages at various current levels versus rotor position for three phases is shown in Figure 2.2. The flux linkage plot for phase ‘a’ is labeled according to the alignment of the phase ‘a’ stator teeth and corresponding rotor teeth. In the aligned position, flux linkage is higher because the rotor has high magnetic permeability and completes the magnetic circuit, whereas a low level of flux linkage is associated with the unaligned position.

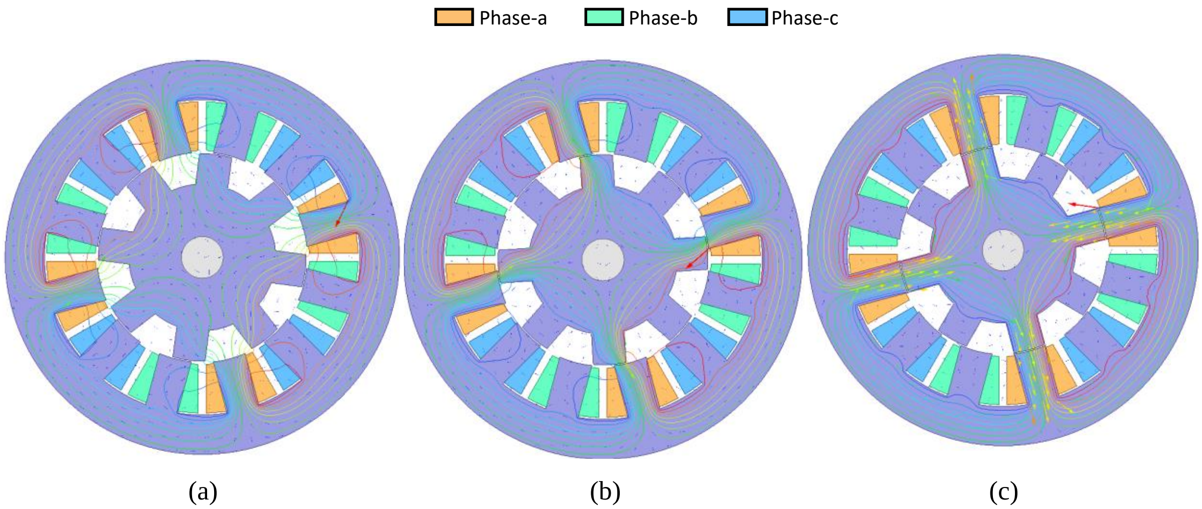

Figure 2.1 SRM simulation showing flux density vectors and contours of magnetic vector potential for phase-a (a) unaligned, (b) intermediate, and (c) aligned rotor positions.

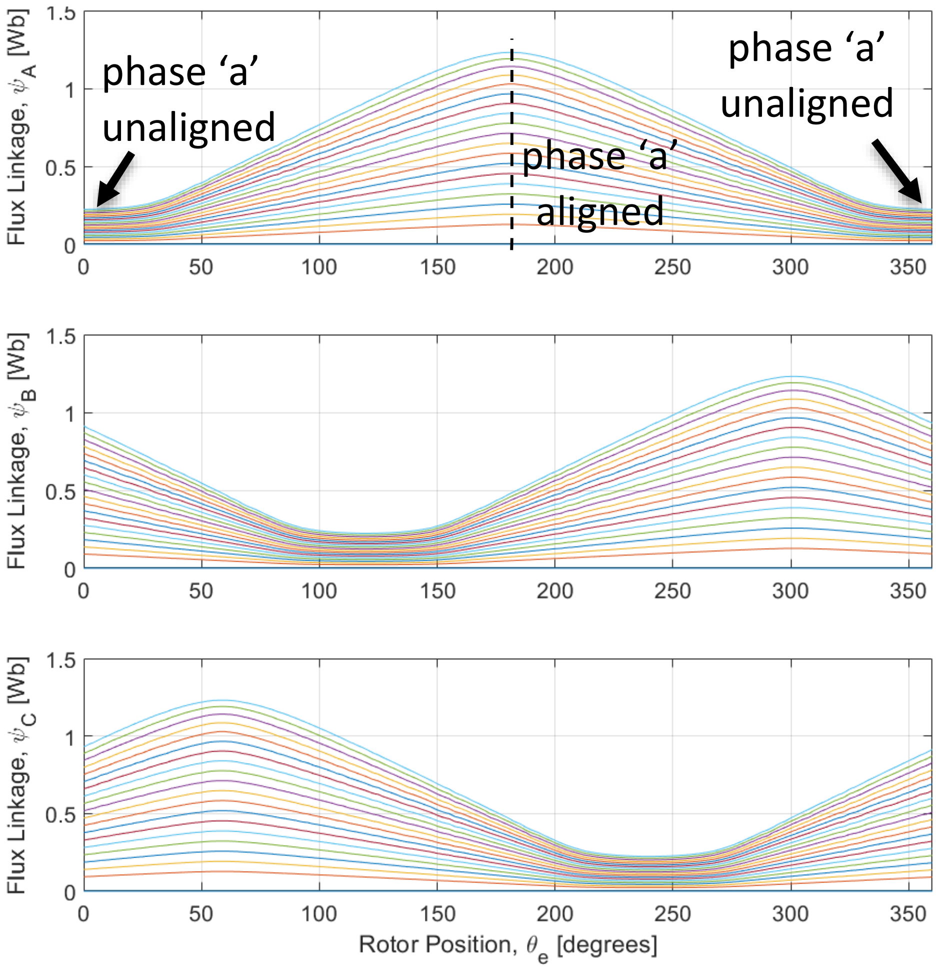

Figure 2.2 Flux linkage versus position for various currents for three phase SRM.

Torque production in SRMs can be analyzed by using a co-energy method, which as shown in Figure 2.3 can be visually represented by graphing flux linkage versus current for each phase for various rotor positions. The energy stored in the system from the phase is obtained by integrating current with respect to the flux linkage, and mutual coupling between phases is neglected, the stored energy associated with a single phase is

$$W_{stored} = \int_0^{\Psi} i(\psi, \theta)\ d\psi \tag{2.2}$$

The co-energy in the system is defined by integrating flux linkage with respect to current:

$$W_c = \int_0^{I} \psi(i, \theta)\ di \tag{2.3}$$

In a magnetically linear system, the co-energy is equal to the stored energy in the system, but in nonlinear systems, they are unequal. Although the co-energy has no direct physical meaning, it can be indirectly used to calculate forces in electromagnetic systems. The relationship between co-energy and stored energy encompasses the relationship between the energy applied, stored, and converted in systems capable of electromagnetic and/or electromechanical energy conversion. As an example, the red point represents an operating point of phase ‘a’, and the co-energy at this point is expressed by

$$W_{a\_c1} = \int_0^{Ia} \psi_a(i_a, \theta)\ di_a \tag{2.4}$$

Similarly, the co-energy at an operation point of a different position is

$$W_{a\_c2} = \int_0^{Ia} \psi_a(i_a, \theta + \Delta\theta)\ di_a \tag{2.5}$$

Instantaneous torque can be defined as the partial derivative of co-energy with respect to position:

$$\tau = \frac{\partial W_c(i, \theta)}{\partial \theta} \tag{2.6}$$

Using equations (2.4) and (2.5), (2.6) can be discretely evaluated:

$$\tau_a = \frac{W_{a\_c2} - W_{a\_c1}}{\Delta\theta} \tag{2.7}$$

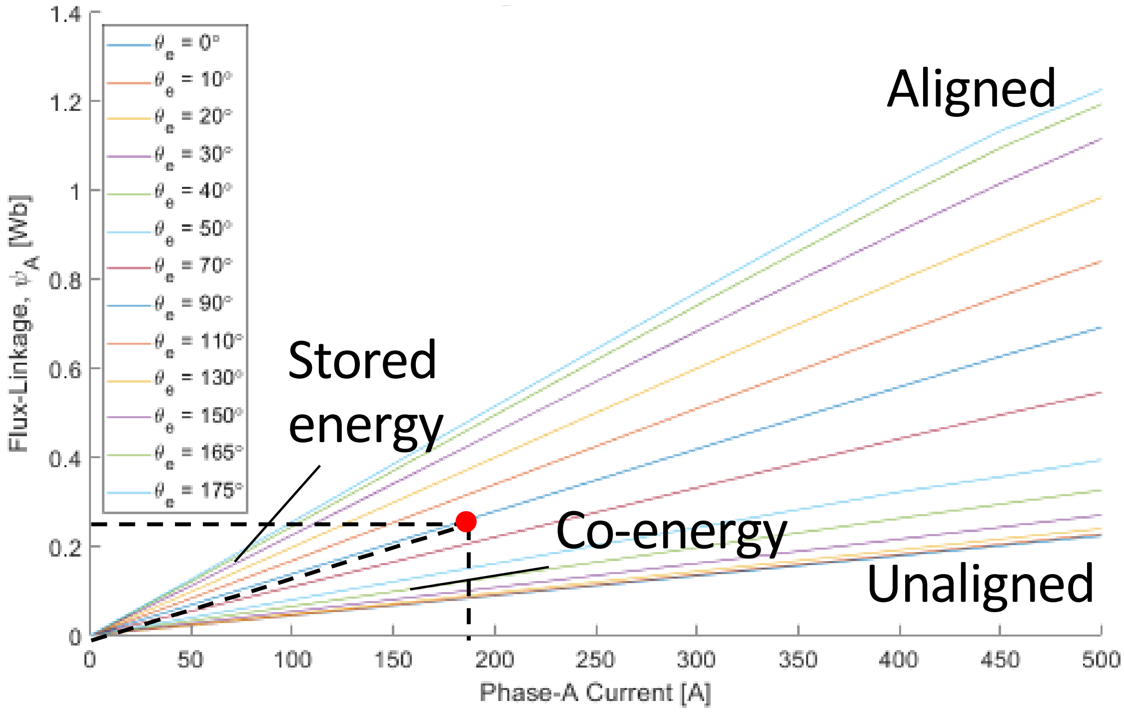

Figure 2.3 Flux linkage vs. current for various rotor positions.

An example of an SRM torque profile is provided in Figure 2.4. Phase ‘a’ produces positive torque across rotor angles between 0 and 180 degrees, and the torque produced by applying a constant current to phase ‘a’ over this range is indicated by the red trace. Phase ‘b’ produces positive torque between 120 and 300 degrees, and the combined torque with constant current applied to phases ‘a’ and ‘b’ is indicated by the green trace. Similarly, phase ‘c’ produces positive torque between 240 and 60 degrees, and the total torque resulting from constant current applied to phases ‘a’ and ‘c’ is indicated by the blue trace. This example illustrates the reason why torque ripple is difficult to avoid in SRMs. The challenge is that in addition to the torque profile being irregular for a given current, this profile changes with current amplitude, especially for saturable designs at higher currents when considerable portions of the steel laminations operate in regions of nonlinear permeability.

Torque ripple propagates to the components connected to the SRM, and in many applications, it is desirable for it to be minimized. Vibrations occur as a result of the forces contributing to torque production as well as strong radial magnetic forces that coincide with the interaction between stator and rotor teeth. These vibrations are one of the main contributors to the acoustic noise of an SRM. Another contributor to acoustic noise is related to a phenomenon called the Barkhausen effect, which is produced by steel laminations as varying fields are applied to the rotor and stator.

Dynamic operation of SRMs is generally similar to that of all electric machines as it relates to the maximum torque versus speed profile shown in Figure 2.5. At low speeds, a torque limit is associated with the maximum current capability (a.k.a rated current), i_{rated} that is largely based on the resistive losses generated in the windings and the characteristics of the thermal management system that transfers heat from the system. For dynamic operation, the second and third terms in the voltage equation (2.1) are the incremental inductance and pseudo back-emf components, and they are dependent on partial derivatives of flux linkage with respect to current and position, respectively. Both terms reflect an increase in the voltage required to achieve a given current as rotational speed increases. The pseudo back-emf term increases directly with speed, and the inductance term increases indirectly with speed due to the partial derivative of current. At a certain speed, the rated current and therefore maximum torque is no longer achievable due to the maximum supply voltage available, and this is referred to as base speed.

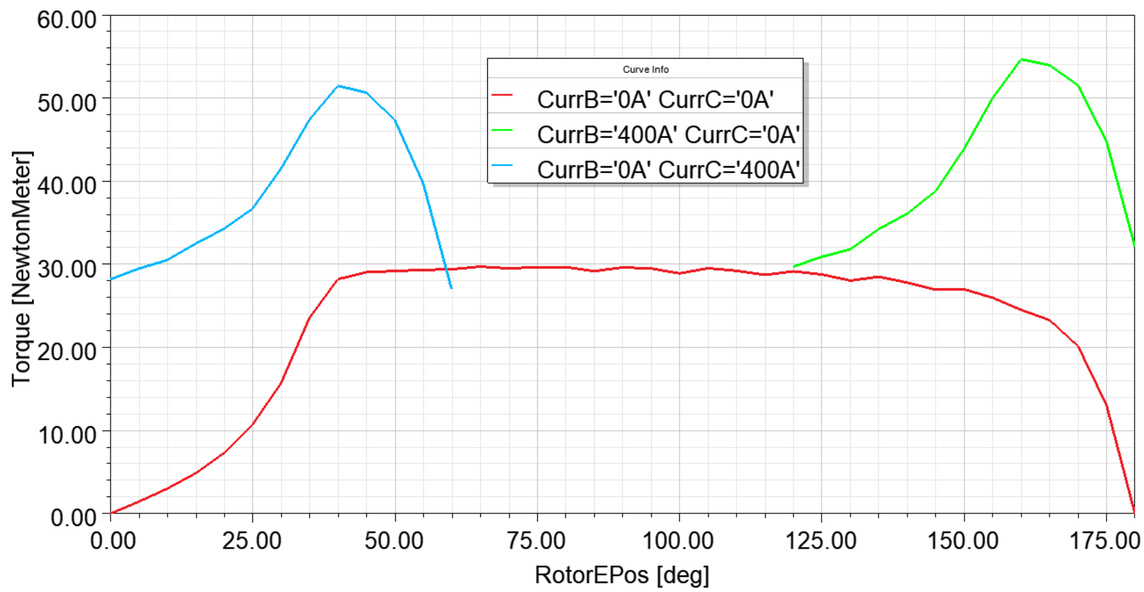

Figure 2.4 Torque versus rotor position for various current conditions.

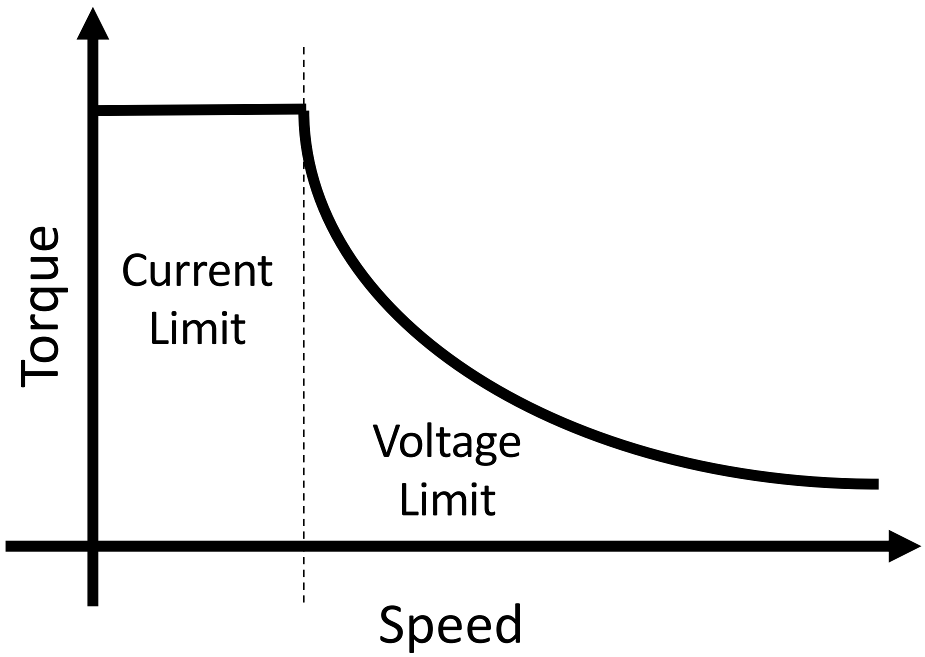

Figure 2.5 Exemplar torque versus speed profile.

As opposed to most multiphase electric machines, the phase windings in conventional SRMs are not connected in a wye or delta configuration. The phases are powered individually since current does not typically flow in alternating directions through the winding as it does in most electric machines. Therefore, SRMs are compatible with a wide range of converter technologies, and many examples are shown in the diagram in Figure 2.6 [2.1]. The most commonly used converter in SRMs is the asymmetric half bridge converter shown in Figure 2.7. Similar to conventional voltage source inverters, it has two switching devices and two diode components per phase. Since the phase windings are not interconnected in SRMs, there is no alternate path for current to flow when the conventional phase leg with anti-parallel diodes is considered. Therefore, diodes are asymmetrically situated such that current in each phase can flow to the DC-link when both switches transition from an on to off state.

The asymmetric half-bridge converter allows for the three primary operation states shown in Figure 2.8. With both upper and lower switching devices on, the DC-link voltage is applied to the phase winding. When both switching devices are in an off state and current is still present in the winding, a negative voltage with a magnitude matching the DC-link voltage is effectively applied to the windings until current reduces to zero and the diodes are no longer forward biased. A free-wheeling state is possible when one switching device is on and the other is off. This is sometimes referred to as a zero-volt loop as approximately zero volts is applied to the winding. When the free-wheeling mode is incorporated into a switching scheme, it is referred to as soft chopping. When the switching scheme only involves both switching states being on or off, it is referred to as hard chopping. The exemplar waveforms in Figure 2.8 [2.1] indicate that soft chopping can lead to reduced current ripple, as the free-wheeling state allows for the phase current to be more readily maintained once a target current is reached.

The most commonly used control techniques used with SRMs are hysteresis band current control and voltage duty cycle control. Current control is particularly applicable at low and moderate speeds when the motor impedance is low and current quickly changes as a result of commutation. It consists of a target current and current band above and below the target current that the measured current is allowed to deviate, as shown in Figure 2.9. Both techniques involve the use of on and

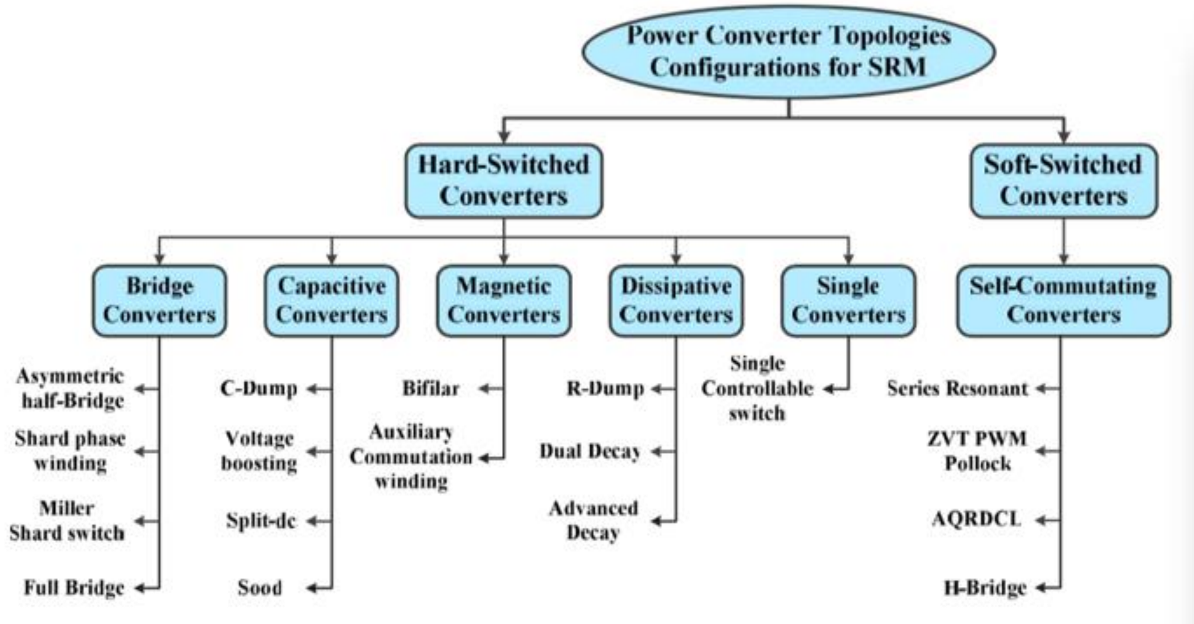

Figure 2.6 Converter technologies applicable to SRMs [2.1].

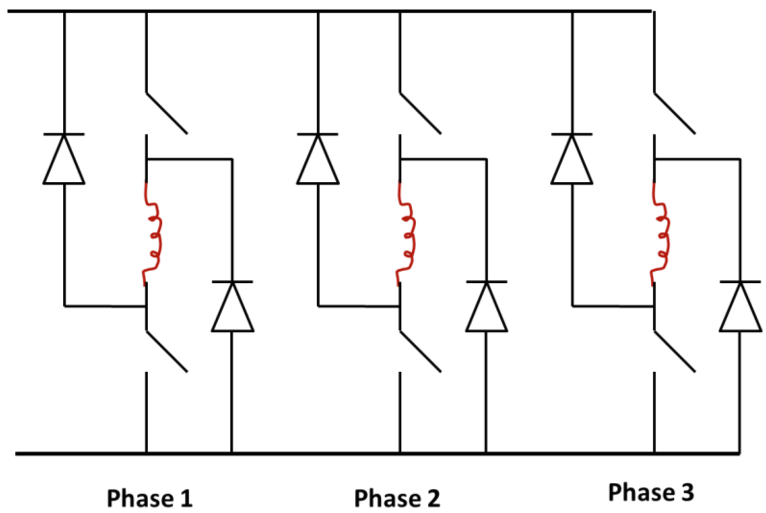

Figure 2.7 Asymmetric half bridge converter for SRMs.

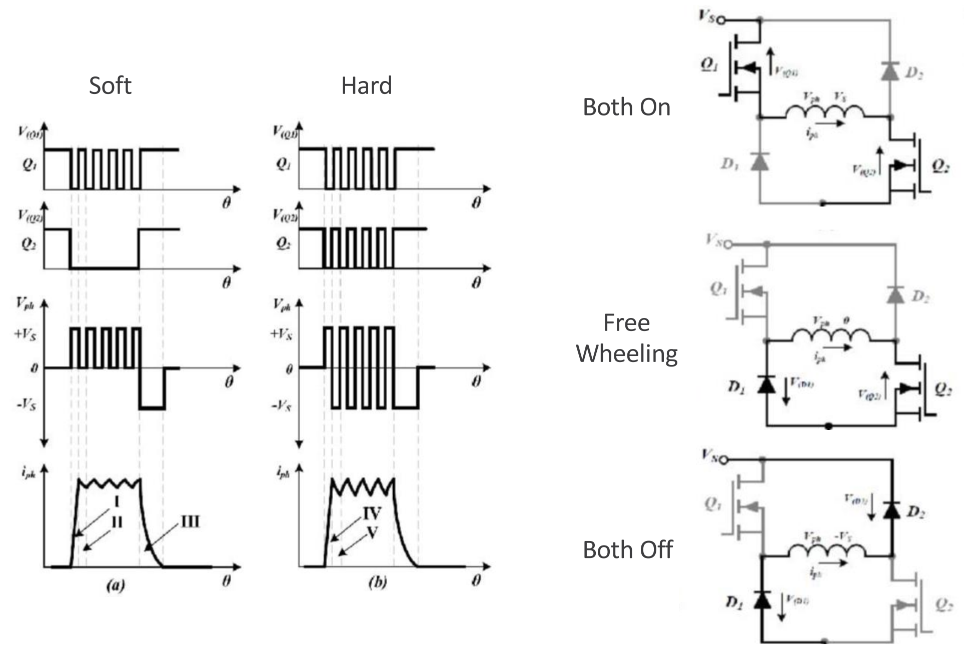

Figure 2.8 Converter operation and exemplar waveforms for soft and hard switching modes [2.1].

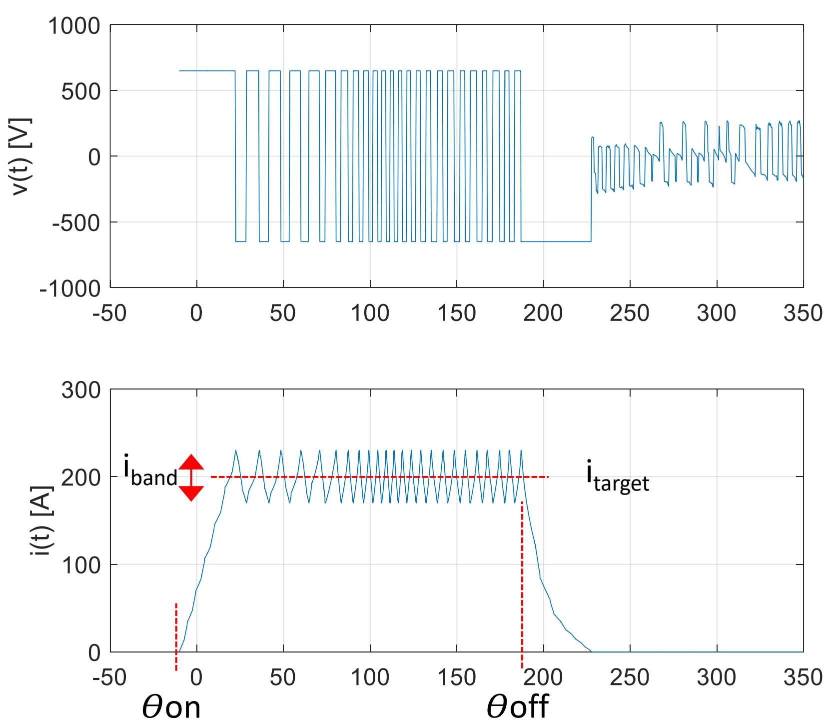

Figure 2.9 Phase voltage and current associated with SRM hysteresis band control.

off angles, θ_{on} and θ_{off}, which represent when a phase should become active and inactive, respectively. These same angles can also be described by the advance angle, θ_{adv} and the dwell angle, θ_{dw}. The advance angle is the angle at which a phase transitions from an “off” to “on” state with respect to the unaligned rotor position, and the dwell angle correlates with the angular range in which a phase is active. The dwell angle remains the same whether the “on” transition is represented directly or indirectly by the advance angle.

Representing the transition angles with advance and dwell angles can be more intuitive as these angles are defined over the torque and speed operating range since average torque closely correlates with the dwell angle, and the requirement for the advance angle to increase varies considerably with speed. For hysteresis band current control, the target current and current band are often defined over the torque-speed operation region by lookup tables or other representative functions. At moderate and high speeds, the voltage control method is often used as SRM operation becomes voltage limited and the duty cycle of the single pulse waveform is varied to control torque or power output. The advantage of using these control techniques is that the voltage method can be implemented with the same basic control structure as the hysteresis band controller, as lookup tables or other functions are used to define the angles throughout the operating range. This conventional controls approach is suitable for some cases, and it has been implemented in many applications. However, the current profile resulting from hysteresis band control at low speeds and the uncontrolled current profile resulting from a single voltage pulse at high speeds does not facilitate mitigation of torque ripple or acoustic noise. Therefore, a review of advanced torque ripple and acoustic noise mitigation methods was conducted.

SRM Geometries and Control Methods

A wide range of research has been conducted to develop and optimize SRM geometries and control methods to reduce torque ripple, acoustic noise, minimize losses, and other operational characteristics. Due to the nonlinearity of the SRM magnetic circuit with respect to both current and position, and an irregular torque profile (Figure 2.4), it is a challenging optimization problem for both SRM design and control techniques. Discussion of SRM research is divided into the following three sections: machine design, advanced control methods, and the last section focuses on references that address both machine design and control.

SRM Design

The FEA method is considered the most accurate motor modeling method for most motors, including the SRM. It was not until the 2000's when computational speeds and memory capacity enabled broad optimization based fully on FEA machine models, and even among recent papers, it is difficult to find publications that involve the optimization of more than 5 machine parameters. Trade-offs and advantages of alternative machine design optimization methods that minimize or eliminate FEA calculations are discussed in the following, and a majority of the references were selected based on the inclusion of FEA results for validation.

Key aspects and features sought out in machine design literature review were the inclusion of nonlinear magnetics, optimization of multiple parameters or objectives, consideration of voltage limitations, advanced optimization algorithms, and/or methods to reduce computational demand and facilitate broad optimization. References involving optimization of both machine and controls are discussed in the last section of the literature review.

Detailed analytical and FEA-based optimization of rotor and stator tooth widths and back iron thickness for maximization of torque density and minimization of acoustic noise is discussed in [2.2]. Analytical models are used to assess the impact of various input design parameters such as rotor radius, stator yoke radius, stack length, and stator pole width output parameters such as rotor hoop stress, current density, inductance overlap ratio, acoustic noise, and torque ripple. Amongst all reviewed literature, this is one of the few references that considers mechanical stresses. For mitigation of acoustic noise, the paper discusses the importance of decreasing the radial force harmonics acting on the stator and making the natural mode frequencies of the stator geometry as high as possible, and if possible, primary modes should be made higher than the audible frequency range (>20kHz). It is noted that a thicker stator yoke yields higher modal frequencies, but there is a trade-off between yoke thickness and power density based on iron utilization (from a magnetic standpoint) and winding thermal considerations. For torque ripple mitigation, the paper discusses the trade-off between decreasing torque ripple and increasing average torque as increasing the number of phases and poles, and increasing rotor and/or stator tooth widths yields lower torque ripple, but also lower average torque. Various geometric design ratios are established and general ranges are provided for achieving low acoustic noise and torque ripple based on analytical models.

Optimization is not discussed in detail and the objective function is set to maximize mean torque. The maximum torque versus speed curve for a resulting design is provided.

Examples of SRMs in various applications are provided in [2.3]. The authors describe how aligned inductance is more straightforward to represent with analytical models and discuss various analytical calculation methods for the unaligned position such as the dual-energy method based on quadrilateral discretization of the slotted region. They note that computations should include the partial linkage effect, where all turns of a coil do not link the same flux, and by using FEA they can be calculated by $\int A \cdot dl$, where A is the average magnetic vector potential across the conductor cross-section and it is integrated along the axial direction of the machine (dl). They point out the importance of including end effects, particularly at the unaligned position where flux can travel in the axial direction which can increase the unaligned inductance by 20-30 percent. The paper includes results of unaligned inductance estimation using end-effect factors that splits the calculation into two parts: $L_u = L_{u0}\ x\ (e_u + f_u)$, where $e_u = L_{end}/L_{u0}$ represents the self-inductance (L_{end}) of the end windings, expressed as a fraction of the uncorrected 2D unaligned inductance, L_{u0}. f_u is a factor that accounts for axial fringing $f_u = (d_r + L_{stk})/L_{stk}$, where d_r is the rotor slot depth, and with the aligned position, a similar factor is used but air-gap length is substituted for d_r. While these 3D end effects are important for final modeling, they comment that the optimization of stator and rotor lamination shapes with 2D FEA is still feasible since end effects would be comparable for each design. A key point they make is that for intermediate positions, calculation of the individual magnetization curves is not practical by analytical methods and that FEA methods should be used.

The effectiveness of genetic algorithms (GA) vs. particle swarm optimization (PSO) is compared in [2.4] regarding optimization by maximizing average torque and minimizing torque ripple with two geometric variables: stator and rotor pole width. An analytical model is used with ANN to determine a reduced solution space prior to FEA modeling used in the PSO and GA optimization. It is shown in Figure 2.10 that the PSO algorithm converges much more quickly than that of the GA and yields an optimal solution that has slightly higher average torque and lower torque ripple. The optimization is carried out with static FEA without consideration of voltage impacts. Since

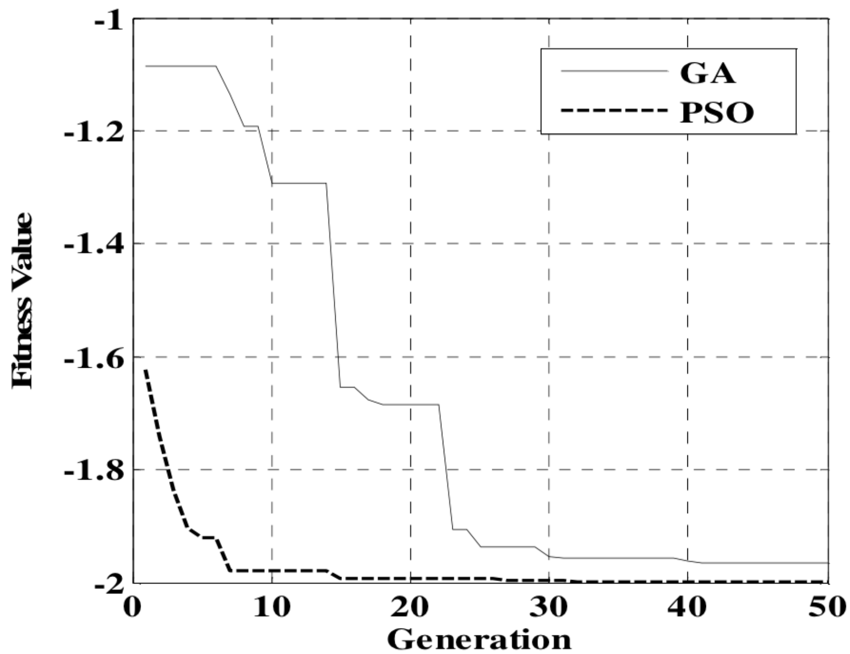

Figure 2.10 Convergence of GA and PSO based methods [2.4].

discussion of control is not provided, it is implied that ideal commutation was assumed, and constant current is assumed for any position where positive torque is produced by a single phase. This results in a design that is optimized at zero speed but is not necessarily optimal at other speeds. A multiple objective evolutionary algorithm is implemented in [2.5], and rotor and stator pole arcs are optimized with the consideration of average torque, torque ripple, and copper loss, using non-dominated sorting GA II (NSGA-II) with well distributed pareto fronts demonstrating trade-offs between objectives. Using the same 8/6 machine as [2.4], PSO is compared with differential evolution (DE) methods with a nearly ten times decrease in execution time for the PSO to generate the Pareto-optimal front.

The authors in [2.6] use PSO with a third order response surface (RS) to predict the impact of variations in 7 independent design variables for multiple objective optimization of various operational characteristics with a significant reduction in required FEA simulations compared to other 1st and 2nd order RS methods. They review various designs of experiment and stochastic evolutionary methods, including a 1st order RS approach requiring FEA simulation for each variation and a 2nd order RS approach that has limited accuracy with increasing number of design variables. Therefore, they proposed and demonstrated an approach that uses definitive screening of designs (DSD) to perform sensitivity analyses to identify significant design variables and reduce the number of design variables accordingly. The DSD approach uses FEA to analyze parameter sensitivity, as shown in Figure 2.11, with ($2N + 1 = 29$ cases) versus ($2^N + 2N + 1 = 16413$ cases) for central composite design (CCD) to construct the RS. Using DSD, the number of variables was reduced from 14 to 7. To improve the accuracy of the RS models, optimal third order RS models were constructed with Audze-Eglais Latin hybpercube designs (AELHD) using 240 experiments. PSO is used both in the selection of significant regression terms as well as the multiple objective optimization generating a Pareto front based on torque ripple, specific torque (Nm/kg), and efficiency, as shown in Figure 2.12. It can be seen that efficiencies above 90% are achieved with torque ripple ranging from 15-20%. Maximum torque density is achieved with efficiencies ranging between 88-90%. The primary benefit of the approach is that multi-objective multi-dimensional optimization is performed based on RS formulated by FEA instead of FEA directly, leading to a significant reduction in computational time. This method must be implemented with caution, as the formulation and accuracy of the RS may not be appropriate depending on the characteristics

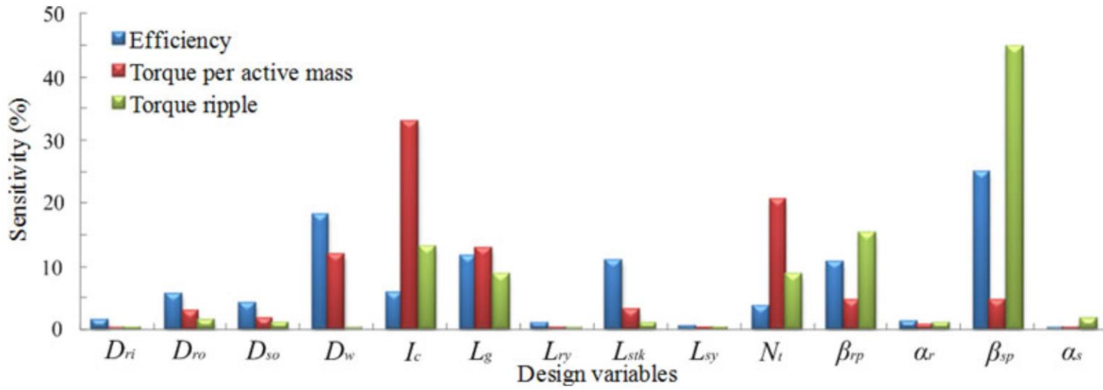

Figure 2.11 Sensitivity indices of torque ripple, efficiency, and torque per active mass to the 14 design variables for a 6/10 SRM [2.6].

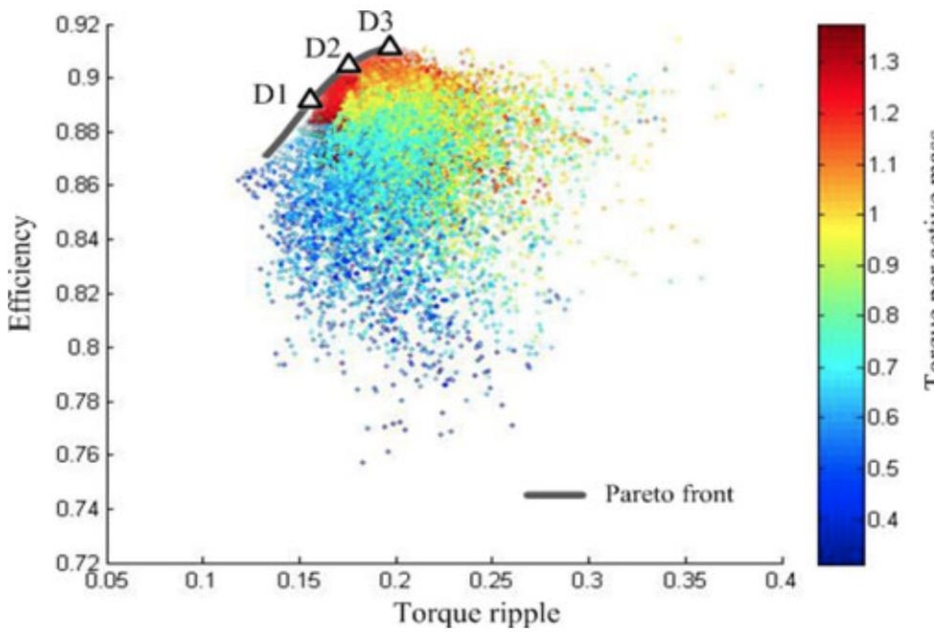

Figure 2.12 Pareto front of multi-objective optimization obtained from the 3rd-order RS method proposed in [2.6].

of the actual response surface and the ability of the 3rd order RS to accurately represent it. The improved accuracy of the proposed method is evaluated and demonstrated against other RS methods by comparing the coefficient of determination (R^2) and root-mean-square error values for torque ripple, mean torque, and efficiency RSs for each method. Dynamic operation was not considered during this optimization, as the only control parameter mentioned is the chopping current, which implies that the current magnitude was assumed to rise and fall instantaneously at the unaligned and aligned positions, respectively.

A combined magnetic equivalent circuit (MEC) and FEA approach for modeling the SRM is presented in [2.7]. Comparisons between the MEC-FEA hybrid model and FEA indicate close agreement in flux linkage for low excitation levels, with increasing error in regions where magnetic saturation occurs, and the higher errors occur at an intermediate position (between aligned and unaligned positions) near the aligned position. Mutual coupling is not accounted for, and while this approach is suitable for some design efforts, the MEC model may need to be significantly modified if geometric features vary far from initial assumptions. Further, more fidelity in the flux linkage mapping may be needed in efforts to minimize torque ripple.

Multi-physics multi-objective design optimization of a bearing-less SRM is discussed in [2.8], where six variables are optimized: stator inner diameter (ID), stator and rotor pole widths, total air-gap flux density, and the ratio of power and flux density generated by motor windings and suspension windings that are used to suspend the motor shaft with electromagnetic forces. During the optimization, 48 particles iterated 180 times to obtain the Pareto front, and convergence was reached at the 175th iteration. Although there is some mention of time transient stepping, there is no mention of the control method used nor is there detail regarding the impacts of voltage limitations, which is perhaps the most important consideration for SRM operation. A lumped parameter equivalent circuit thermal model is used to model the heat transfer characteristics. There is only a mention of a single speed and power specification, and it is therefore assumed that the optimization is for only one operation point. Hysteresis and eddy current losses are post processed from the time-domain simulation based on transient iron loss using the flux density of each mesh. Torque ripple is not addressed in the paper. The Pareto front is graphically portrayed in Figure

2.13 with the reciprocal of torque density (kg/Nm) versus the reciprocal of efficiency, and a maximum efficiency of about 70% and inverse torque density 22.2 kg/Nm is demonstrated.

A comprehensive review of various configurations of mutually coupled SRMs (MCSRM) is provided in [2.9]. This type of mutually coupled SRM is mainly sought after due to the possibility of being driven by conventional voltage source inverter (VSI). Various winding configurations, including single versus double layer windings and short pitched versus full pitched are discussed. Copper loss, iron loss, power factor, efficiency, torque ripple, and torque density are compared for these various winding configurations, and iron loss, copper loss, efficiency, torque density, and torque ripple are compared for various excitation methods. The single layer full pitch MCSRM yielded the highest torque density and lowest torque ripple, and not the highest iron loss and copper loss.

The double layer, short-pitched MCSRM achieved the highest efficiency but also the highest torque ripple, while the single layer short pitch MCSRM generally resulted in quality metrics between the former two. Regarding excitation methods, bipolar 180 provides the highest torque density, moderate torque ripple, while unipolar 180 provides the lowest torque ripple and highest efficiency. Various modeling methods are discussed including lookup tables and an approach that reduces system dimensions by translating the three phase variables to the rotating frame, resulting in dq components. Although some parameters for the reference machine are provided, non-normalized torque metrics are not discussed, and therefore it is difficult to compare conventional SRM performance with the optimized designs. Furthermore, the speed or torque level at which the performance and operational metric comparisons are performed, and the influence of speed upon these metrics is not addressed in detail.

SRM Control

Key aspects and features sought out in a review of SRM control literature were consideration of nonlinear machine characteristics, optimization of multiple parameters or objectives such as torque ripple, consideration of voltage limitations, predictive control, advanced optimization algorithms, self-learning, online optimization, methods to reduce machine model complexity, and evaluation of controller effectiveness across the entire torque-speed operation region. References involving optimization of both machine and controls are discussed in the last section of the literature review.

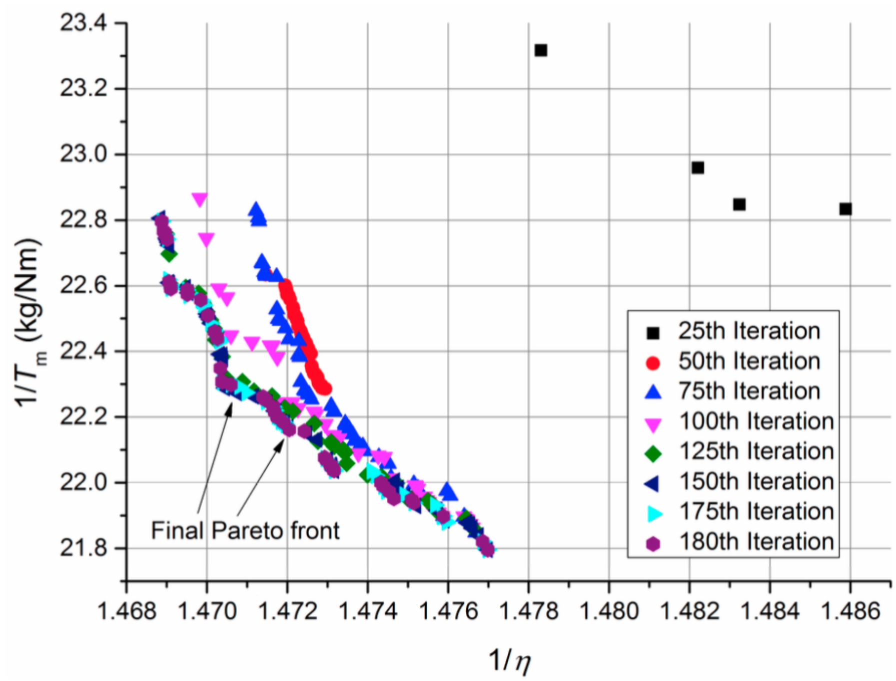

Figure 2.13 Searched Pareto front after different number of iterations [2.8].

The limitations of conventional proportional-integral-derivative (PID) control are discussed in [2.10], and feedback linearization is used to develop expressions of flux linkage and torque with position, speed, and current as state variables. This decouples the effect of voltage on torque to simplify the control problem. In comparison to [2.10], [2.11] applies feedback linearization to a reduced order model with two timescales (mechanical and electrical). Position control is implemented with PID direct torque control (DTC) using measured position and current. Experimental results do not show close correlation between simulated and measured position and speed. Both [2.10] and [2.11] are particularly suited for applications such as direct drive robotics, while applicability over a wide speed and torque range is not addressed.

A method is presented in [2.12] where self-learning of SRM characteristics is implemented before the controller is put into service. The SRM is used as its own loading machine to characterize torque vs. current and position in static (net-zero torque) and dynamic inertia-position tests. However, mutual coupling is not accounted for, and linear assumptions are made to determine optimal current in magnetic saturation.

Random perturbation is used in [2.13] to modify conventional switching angles during online control to reduce acoustic noise. Bi-cubic spline interpolation is used in [2.14] to represent nonlinear experimental data for decoupled linear systems for torque ripple minimization. In [2.15], offline generation of coefficients using bi-cubic spline interpolation of flux linkage vs. current mapping is applied for online computation of flux linkage and torque using measured voltage and current. Results show an increase of 35% and 50% rms current for torque ripple reduction of 60% and 90% for a given torque. These methods do not consider mutual coupling or voltage/speed limitations.

Torque ripple reduction is achieved in [2.16] through current control simplification and improved current tracking by separating the reference current into three sections: rising, falling, and primary. Mutual coupling is considered, and the impacts are described as having a negative impact on operation. Reference [2.17] extends the current control simplification proposed in [2.16] to applications needing high performance motion control. Components of Fourier series expansion are used in [2.18] to represent an inductance profile. The method assumes linearity, no mutual coupling, and the limitation of applicability beyond base speed is acknowledged by the authors.

In [2.19], the simultaneous optimization of switching angles is achieved through brute force calculation of torque, torque ripple coefficient, and drive efficiency for all turn-on turn-off angle combinations. Optimization is achieved in a somewhat manual manner as 2D isovalues of these quantities are plotted for various angles for a given speed, as shown in Figure 2.14 (a-c). While the tradeoff between efficiency and torque ripple is demonstrated, no cost function or optimization function is used in determining optimal conditions, as a weighting method would be needed. A comparison is made between simulation and test data in Figure 2.14(d) showing simulated efficiency contours and measured efficiency points for a targeted 102 kW for an EV propulsion drive. A peak efficiency of 91.6% was measured versus 93% simulated at about 53 kW and 10,000 rpm.

Since common SRM control methods use either precalculated parameters or direct torque control, both of which rely on torque and flux as a function of current and position, [2.20] compares methods for determining flux linkage maps with static FEA and dynamic measurements, where phase inductance and flux-linkage are reduced by eddy current effects in the winding. Conventional hysteresis current control method is used while focus is placed on the impacts of flux linkage determination by comparing direct transient FEA simulation (considered the baseline), model-based simulation using static FEA flux-linkage mapping, and dynamic flux linkage mapping (emulated measurement in FEA). Winding eddy current effects have little direct impact on torque mapping; however, the eddy effects on flux-linkage mapping and corresponding current/voltage behavior do impact the torque as the controller is implemented. Results indicate less than a 2% difference in torque from baseline for both static and dynamic characterization methods at low speeds, while estimated torque using static FEA is 15% lower than baseline compared to only 1.5% less than baseline with the FEA emulated dynamically measured flux linkages. Therefore, the dynamic flux linkage mapping approach was shown to be more effective in predicting high-speed operation than that of direct static FEA flux linkage mapping, as eddy effects resulting from current displacement yield lower phase inductance and allow current to rise faster, yielding higher torque for a given voltage.

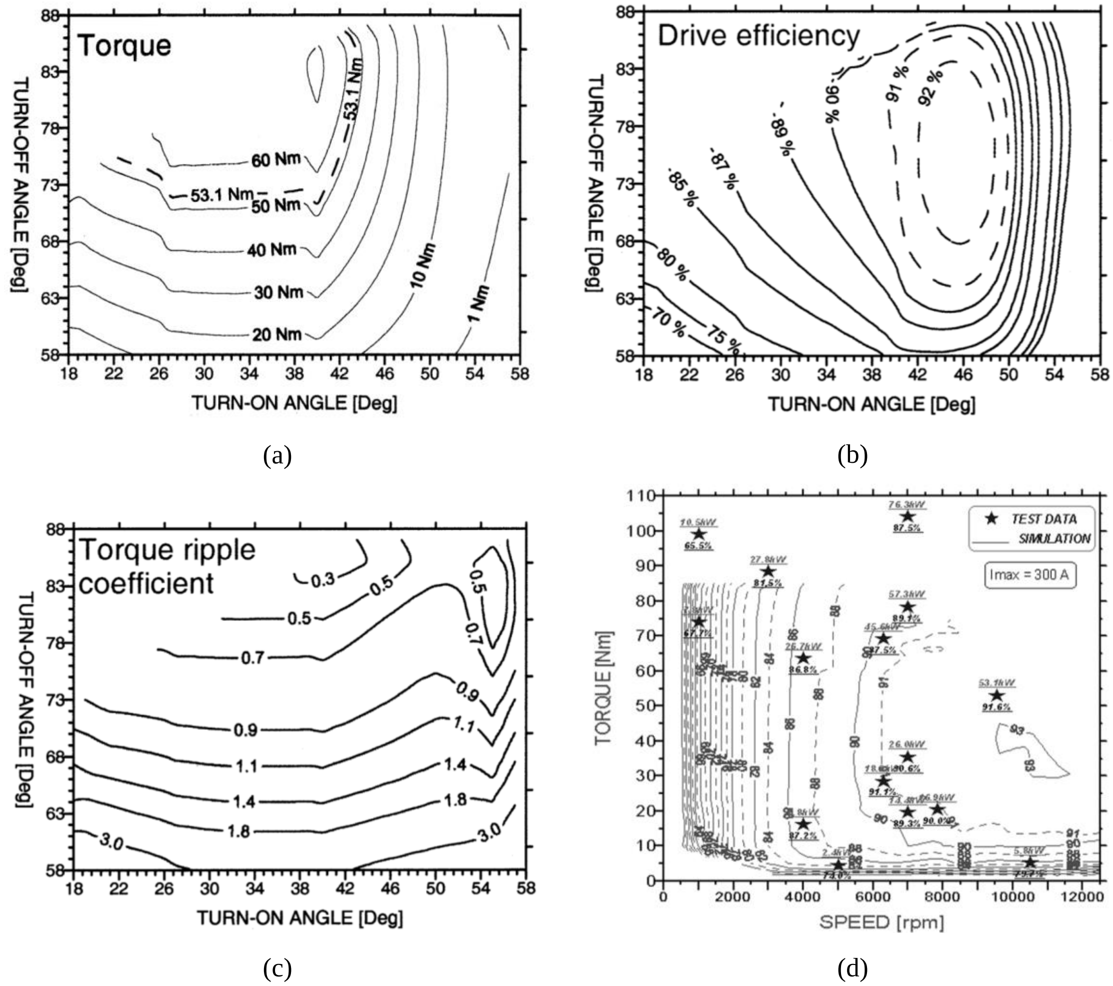

Figure 2.14 Simulated (a) torque, (b) drive efficiency, and (c) torque ripple for various turn-on and turn-off angles, and (d) a comparison of simulated and measured efficiencies across operation region [2.19].

A speed control algorithm is proposed in [2.21] using two-phase excitation to ensure convergence of currents and speed to targeted reference values with consideration of mutual coupling between phases and therefore facilitates minimization of torque ripple and acoustic noise. Past work with torque distribution functions linearly deenergize and linearly energize adjacent phases during the commutation interval neglecting the effects of mutual coupling. A state space model of the SRM with consideration of mutual coupling was implemented with the current of adjacent phases and speed as state space variables, and corresponding control vectors were analytically determined such that asymptotic stability is achieved and is evaluated using a PI controller. Speed tracking is successfully demonstrated at one speed, but performance at various points in the torque-speed operation region are not discussed, which is particularly of interest at high speeds where voltage limitations occur.

Reference [2.22] extends the work in [2.21] to consider the important dependency and nonlinearity of self and mutual inductances as a function of position and current. Design of a feedback linearization controller (FLC) and sliding mode controller was performed using a transformed dynamic model to simplify the state equations. The sliding mode controller is designed with two sliding surfaces, and controllers are defined such that the state variables (which are indirectly phase currents and speed) achieve asymptotic convergence. A comparison showed that the FLC controller tracked speed more quickly, but the SMC maintained speed better after load transients, and both performed considerably better than the linearized PI controller. While the approach used to achieve robust speed control is appealing, it is not clear how the self and mutual inductances were derived and represented (e.g., look-up table or curve-fitting for example), and more importantly, details are not discussed regarding the true challenge in SRM control, namely the position dependent control of current and torque. While torque ripple is mentioned, it is not addressed in the formulation of the control problem. Furthermore, as speed tracking is important in some applications, it is not typically a challenge in vehicle propulsion due to acceleration limitations associated with the large mass/inertia of vehicles and friction between tire and road.

A type of predictive control is implemented in [2.23], where the on-time PWM pulse is calculated for a given reference current in each time step using the machine inductance profile ($L(i,\theta)$) to predict the required flux linkage and pulse duration. It is shown that this method results in close tracking of a reference current profile with a minimal error. The maximum error is observed during the activation of a phase where the reference current has the most significant rate of change and tracking is limited by measurement noise and error from current and position sensors. This method is useful in the implementation of current profile tracking, as shown in Figure 2.15 but may be limited at high speeds and high loads when single pulse or multiple pulse operation may need to be implemented due to voltage limitations, or for cases where operational frequency is similar is closer to that of the switching frequency. The method does not directly (and does not claim or intend to) consider voltage limitations, and a separate method for deriving current profile with consideration of voltage constraints must be implemented.

A control method is proposed in [2.24] that uses a fixed frequency switching scheme with feed-forward voltage control using an asymmetrical half bridge drive for each phase. The paper addresses the fact that the proposed method is particularly applicable at low speeds where torque ripple minimization is implemented, and conventional multi-pulse control is implemented at higher speeds. A voltage reference is determined by the phase voltage equation and flux linkage curves. Predictive control based on flux linkage estimation compensates for the control interval delay, as shown in Figure 2.16. As a result, the average applied voltage during one control interval can vary from -Vdc to +Vdc based on the feed-forward voltage calculation (as opposed to +/-Vdc with hard chopping and +/-Vdc and 0 V with soft chopping). The resulting current ripple is compared with two level hysteresis band (2LHB), or hard chopping, and three level hysteresis band (3LHB), or soft chopping. The resulting RMS error in the current is 0.189 A at a current magnitude of 2 A for the proposed technique versus 0.446 A and 0.465 A for 2LHB and 3LHB switching schemes, respectively. Further, the number of switching events was 186 versus 258 and 230, and converter losses were 63.3 W versus 77.1 W and 76.1 W when comparing the proposed method with 2LHB and 3LHB switching schemes. The resulting acoustic noise spectrum is shown to be much lower, particularly for higher frequencies, as expected since a fixed carrier frequency is used in the proposed approach versus the hysteresis switching schemes.

Elitest mutated multi-objective PSO in used in [2.25] to determine parameters for an adaptive sliding mode speed controller and switching angles for conventional hysteresis control. A multi-

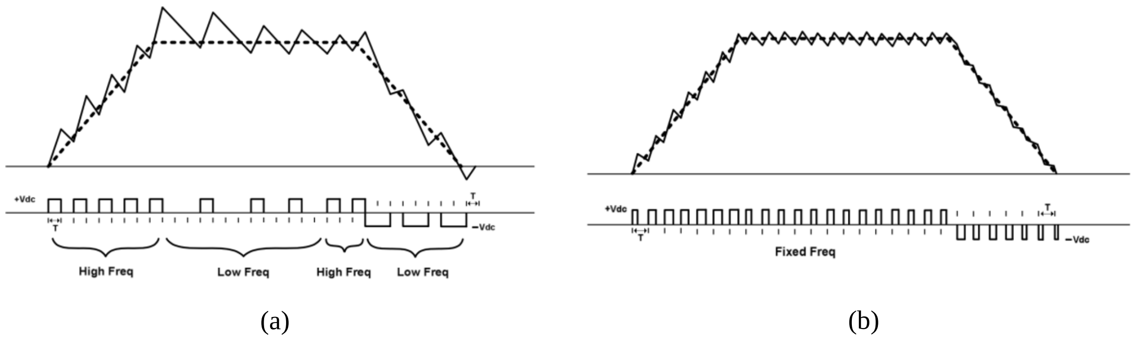

Figure 2.15 Switched current waveform and current reference for (a) conventional soft chopping and (b) predictive control with fixed frequency [2.23].

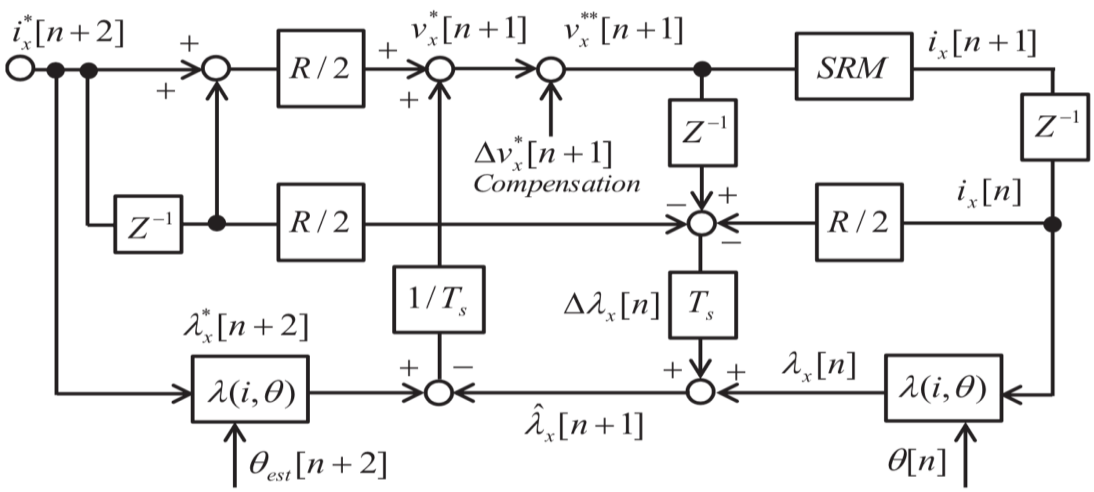

Figure 2.16 Block diagram of proposed fixed frequency controller feed-forward voltage control [2.24].

objective cost function includes integral squared errors of speed and torque ripple. While the approach is clever, only simulations results are presented, and it is not clear if it is intended or able to be implemented for online optimization, offline optimization, or just simulation wherein a lookup table and functions are used in deployment. Furthermore, the output of the optimization is switching angles and current reference values for conventional hysteresis control, which has limited ability to minimize torque ripple since torque ripple reduction requires complex current waveforms.

A fixed frequency sliding mode current controller with consideration of magnetic saturation and mutual coupling is proposed in [2.26] that is based on an equivalent circuit model of the SRM. Experimental results include switching waveforms and a comparison of RMS current error and RMS torque error between 1) a sliding mode controller with 20 kHz switching frequency/40 kHz sampling and 2) a hysteresis controller at 10-30 kHz switching/40kHz sampling and 3) a hysteresis controller at 10-30kHz switching and 200 kHz sampling. The sliding mode current control significantly outperforms the hysteresis controller with 40 kHz sampling and has comparable results with the hysteresis controller with 200 kHz sampling across the entire operating speed range at two different torque levels. The sliding mode current controller is proposed as the inner loop of a torque ripple minimizing control scheme. Little detail is provided regarding torque ripple optimization, as the focus of the paper is on current tracking, and a simple linear TSF is used for instantaneous torque control in both simulation and experiment. While the approach shows similar performance can be achieved with much lower FPGA sampling frequency, predictive control methods may offer an advantage at higher speeds, as considerable tracking error is present at high speeds, particularly near the on and off transition points.

A novel torque sharing function is proposed in [2.27] to minimize torque ripple, copper loss, and maximum absolute value of the rate of change of the flux linkage (RCFL or MR). The objective function involves the sum of currents raised to an undetermined constant power, q, instead of averaged square value of current, with boundary conditions $q \geq 2$ and $q \to \infty$. For this study, the absolute value of RCFL (Wb/rad) was minimal for $r = 4$, where $r = q/(q-2) \rightarrow q = 2.5$. As shown in Figure 2.17(a), the discrete calculation of the TSF for any position is based directly on the ratio of inductances that are a function of position. The optimal TSF is chosen to attain secondary objectives of minimizing copper loss and max flux change. The approach neglects magnetic saturation. The control scheme uses a TSF to generate torque reference for each phase, then a torque to current block to generate the current reference, with current controlled with a classical hysteresis controller. A plot of torque ripple vs. speed shown in Figure 2.17(b) indicates that the proposed method yields comparable torque ripple levels at low speeds (20-30%) but is much lower at high speeds (less than 40%) compared with linear (85%), sinusoidal (75%), and cubic (68%) TSF methods. At a given torque level, current is lower at 3.9 Arms for the proposed method versus 5.4, 5.8, 5.8 Arms for the cubic, linear, and sinusoidal TSF methods, respectively.

Optimization based on differential evolution is implemented in [2.28] to generate optimal current profiles based on minimization of harmonics in the torque ripple and sum of radial forces for acoustic noise minimization. The authors note that the TSF is difficult to define for cases when one phase may be producing negative torque. They also note that two-step excitation (where a second step is applied to cancel vibration from the first vibration) and spreading PWM spectrum across the frequency range for vibration reduction may not avoid resonant frequencies throughout the operating speed range. They propose minimizing radial forces based on a nonlinear model, where radial forces are calculated using a Maxwell stress tensor method which integrates the difference of square radial and tangential flux density across a tooth surface at the air gap.

Similar to torque, radial force is also a function of position and current. The authors point out that the SRM is more prone to low frequency vibration due to resonance with radial force harmonics. To minimize FEA computational requirements, torque and radial forces are represented as the product of the square of the phase current and torque and force factors that are a function of position and current, and these factors are approximated by curve fitting to FEA. Ultimately, the approach is to inject appropriate harmonics in the phase current waveforms to meet tradeoff objectives. However, one key potential limitation of this approach may be the ability to inject higher harmonics at higher speeds where voltage limits are encountered. An optimization function is used to minimize the sum of weighted torque and sum of radial force harmonics. The optimization is subjected to a torque ripple constraint, current rating, and maximum change in flux linkage vs. position, which are grouped together as a penalty function. While this indirectly

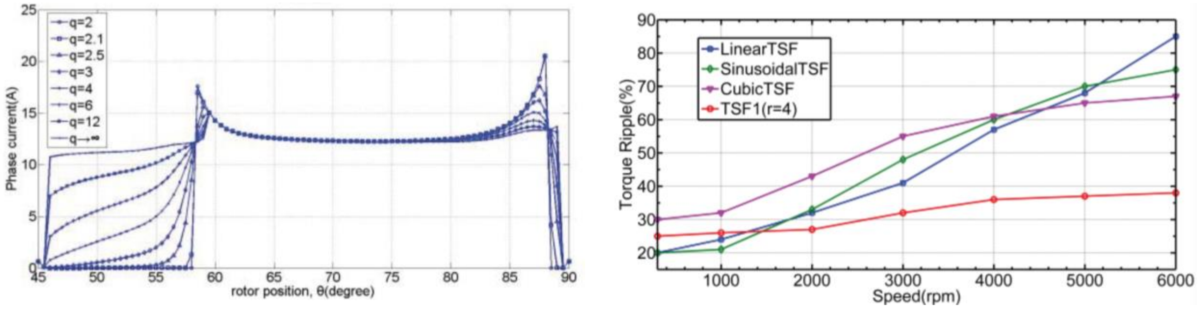

(a) (b)

Figure 2.17 (a) Current reference of the proposed TSFs for various q-values and (b) torque ripple versus speed at 1 Nm torque for various TSF methods [2.27].

considers voltage limitations by minimizing RCFL, it is not an implicit consideration of voltage limits. The initialization procedure for the DE involves a randomization and the cost function is used to determine the first-generation design variable vector. The number of generations in this study was 40, number of individual designs was 40, and number of variables was 13. Simulation results are shown for a speed that is not mentioned, and it is shown in Figure 2.18 that radial force ripple (the variation of the instantaneous sum of radial forces with rotor position) is reduced from 71% to 46% using the optimized current profile with a 240° conduction angle versus conventional duty cycle control ("non-optimized current profile") and to 15.8% by increasing the conduction angle of the current profile to 270°, but at the expense of 14.5% higher copper losses and increased torque ripple.

A sliding mode control technique is applied in [2.29] to achieve robust speed control and mitigates "chatter" phenomenon that can occur in sliding mode controllers through the use of adaptive fuzzy compensation. This avoids potential additional energy consumption, reduced hardware lifetime, and less control accuracy. As shown in Figure 2.19, the adaptive fuzzy control (AFC) is based on speed error, and a torque command is output to a TSF controller using a cubic polynomial function with the torque command shared evenly across all phases. This is a clever implementation for robust speed control, but does not address issues with torque ripple, and is more suitable for applications requiring robust speed control such as in some industrial applications, whereas in direct drive propulsion applications, speed tracking is generally not a challenge due to vehicle inertia and torque limits related to tire-road friction.

The authors in [2.30] discuss how there are performance improvement limitations of previously proposed online TSF methods compared to conventional (offline) TSFs. They present a method in which the conventional TSF is optimized to minimize evaluation criteria, and the optimizing parameters are applied to a corresponding online TSF with a modified current control algorithm. They point out that previous work with linear, cubic, cosine, exponential, and modified TSF lack the ability to track phase current at elevated speeds due to voltage limits. They reference [2.26] regarding the impact of absolute rate of change of flux linkage (ARCFL), and for conventional TSFs two modes exist during phase commutation. For mode I (start of commutation), ARCFL of

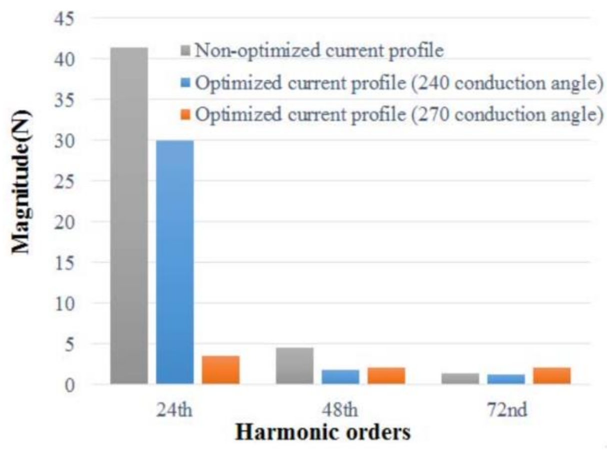

Figure 2.18 Comparison of the first three harmonics of the sum or radial forces with non-optimized and optimized current profiles [2.28].

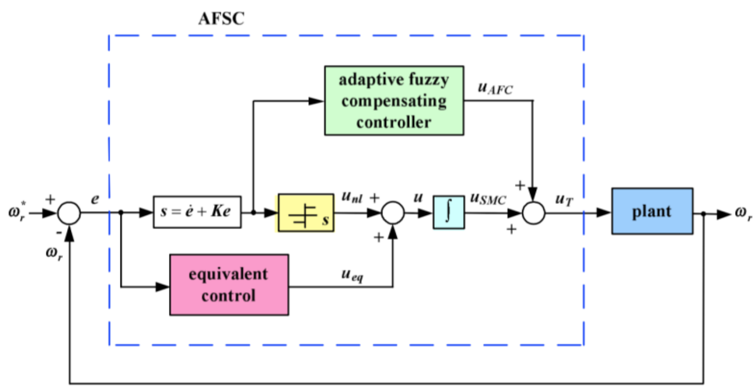

(a)

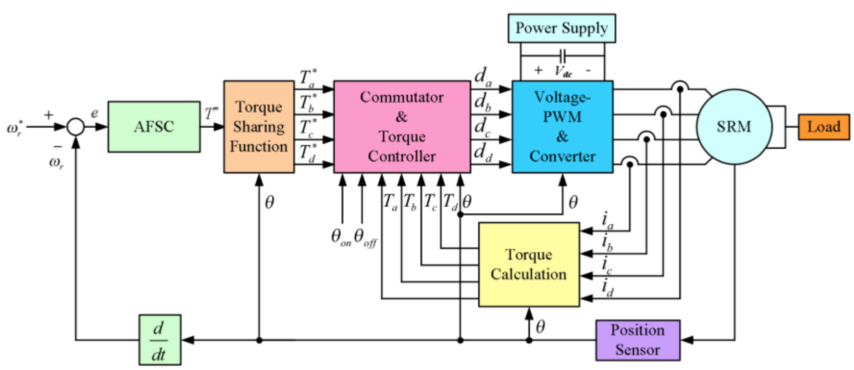

(b)

Figure 2.19 AFC-based (a) architecture and (b) SRM drive system [2.29].

the incoming phase is higher than the outgoing phase and ARCFL of outgoing phase becomes much higher than the incoming phase in mode II (at the end of phase commutation). Thus, the outgoing phase determines the maximum ARCFL and maximum TRFS (torque ripple free speed).

Therefore, a modified online TSF method is introduced that minimizes the maximum ARCFL and maximizes the TRFS region by using a PI compensator to minimize error between reference torque and estimated torque, with the output of the PI compensator added to the phase that has a lower ARCFL (because it is therefore more controllable), which is the outgoing phase in mode I and incoming phase in mode II. This permits better torque tracking and therefore the ability to minimize torque ripple. The online control method, shown in Figure 2.20, uses current lookup tables $i(\theta,\tau)$ for a given reference torque, and torque lookup tables $\tau(\theta,i)$ are used for torque estimation based on current measurement. The online method is shown to reduce the ARCFL considerably and increases the average torque and reduces the torque ripple from 40% to 20% in the most improved case. However, torque ripple still increases with speed due to saturation of the current controller, and torque tracking at high speeds is slightly less than conventional TSF methods. This is improved by defining a fitness function which sums the normalized ARCFL and square of current (to which copper loss is proportional), both of which have weighting factors, and GA based optimization is used to find the angle of phase activation (θ_{on}) and the overlapping angle between phases (θ_{ov}) that minimizes the fitness function.

The two components of the fitness function are defined as functions of the reference torque, θ_{on}, and θ_{ov}. Optimization using various type of TSFs was compared, with torque ripple reaching 41.91% for the unoptimized TSF, and 22.74%, 12.53% and 12.25% for the optimized offline TSF, optimized online TSF, and optimized online TSF with modified hysteresis current control, respectively. No detail was given regarding what the modification is; it is perhaps just soft switching. A comparison is provided across speed with the same torque reference, and the optimized online TSF achieves higher torque at elevated speeds and considerably lower torque ripple. The approach does not include mutual coupling, though its incorporation seems possible. While variation of control parameters across torque-speed range is mentioned, the control block diagram does not show higher level control or how this is handled. As authors note, the method

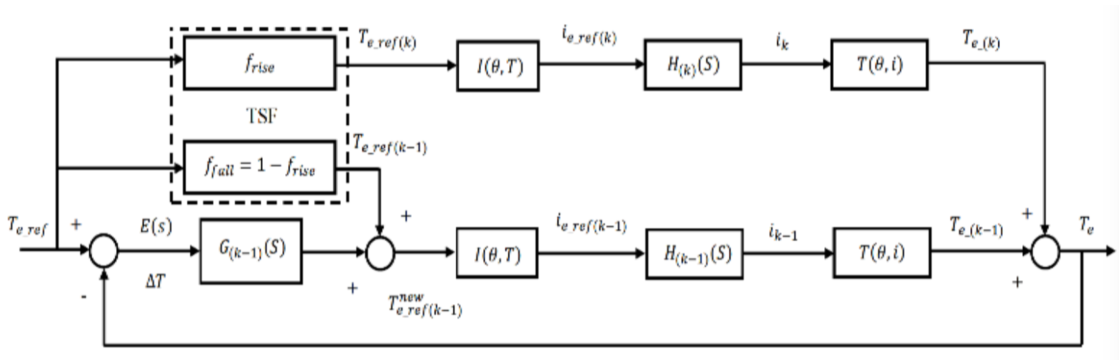

(a)

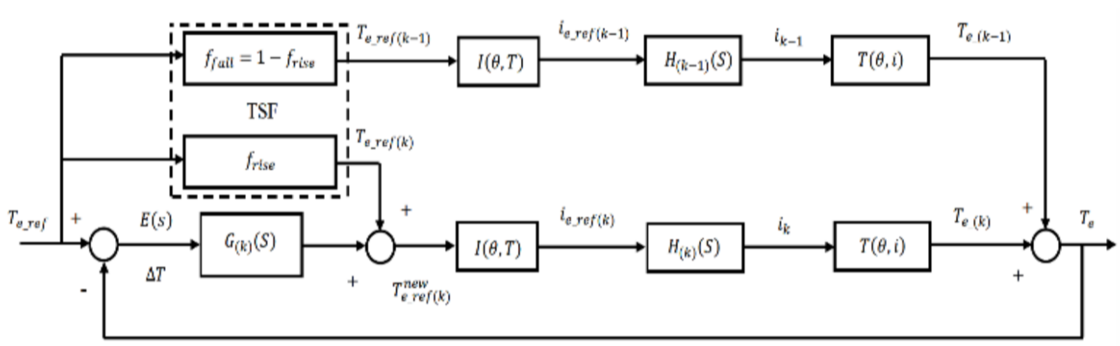

(b)

Figure 2.20 Online TSF control system applied in (a) mode I and (b) mode II [2.30].

may be better suited for advanced current control schemes such as PWM current control and model predictive current control. Of all reviewed control-based literature, this may be the one that most readily addresses limitations of dc link voltage/speed, and current control loop time delay.

Authors in [2.31] note the challenge and need for an expert user during the design and implementation of fuzzy logic and proposes a PI based control scheme for speed control and torque ripple minimization using a hybrid many optimizing liaison gravitational search algorithm (MOLGSA) with an outer speed loop and inner current control loop with intelligent selection of turn on and turn off angle. The approach resulted in a reduction of torque ripple, integral square of speed error, and current by 12.8%, 58%, and 16.7% compared to GSA. It is mentioned that PSO resembles a genetic algorithm (GA) in that it involves initialization of a population of random solutions and then to find optimal solutions by updating generations; however, PSO has no evolution operators such as cross-over and mutation. A simplified PSO called "social only" has been previously proposed and named "many optimizing liaisons (MOL)" and is reported to have improved performance and is easier to tune. The MOLGSA combines the exploitation ability of MOL/PSO with the exploration ability of GSA. This paper uses a hybrid MOL and GSA (MOLGSA) to determine 6 optimal parameters: turn-on and turn-off angles, current PI gains, and speed PI gains with a fitness function defined as the sum of the integral squared error (ISE) of speed and torque ripple. A block diagram of the proposed controller is shown in Figure 2.21, where the output of the MOLGSA supplies the appropriate controller gains. The best values of Ki_{speed}, Kp_{speed}, $Ki_{current}$, $Kp_{current}$, θ_{on}, and θ_{off} for minimal torque ripple with MOLGSA are 0.1, 9.9, 0.1, 29.8, 48.3°, and 81.0°. The best average torque ripple achieved with MOLGSA was 45.9% versus 46.2% with MOL and 74.8% with GSA. This appears to be determined at one speed, and how these vary vs. torque and speed is not addressed. Furthermore, while it is a good exercise to determine PI gains in simulation, PI gains often need to be adjusted as a result of noise and discontinuities arising from position and current measurement.

A fuzzy-logic control strategy is used in [2.32] for an integrated starter generator, and control is based on generated power error and its derivative. As shown in Figure 2.22, a table is used to determine the θ_{off} switching angle, and fuzzy logic generates the turn on angle. The error in power and the change in error are subjected to membership functions with 9 classification levels from

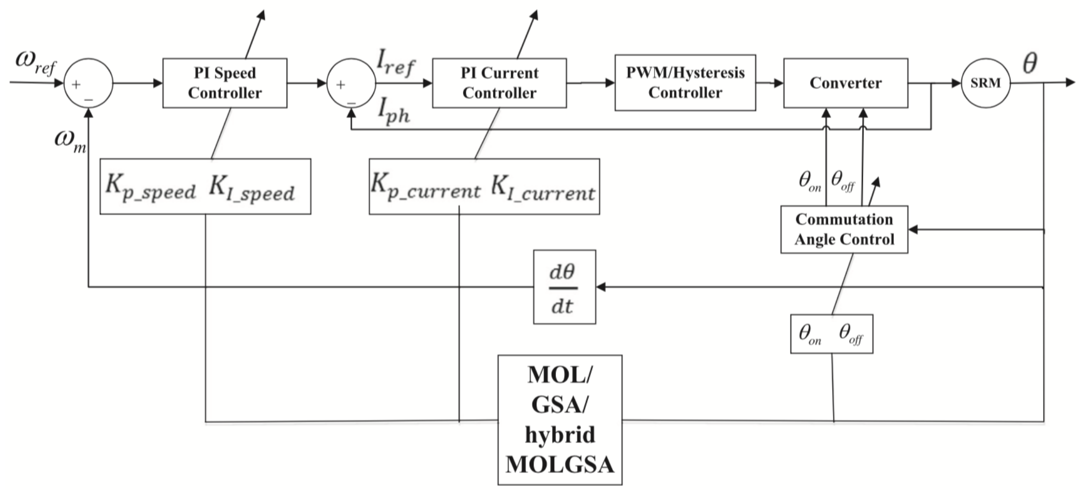

Figure 2.21 Block diagram of MOLGSA speed control method [2.31].

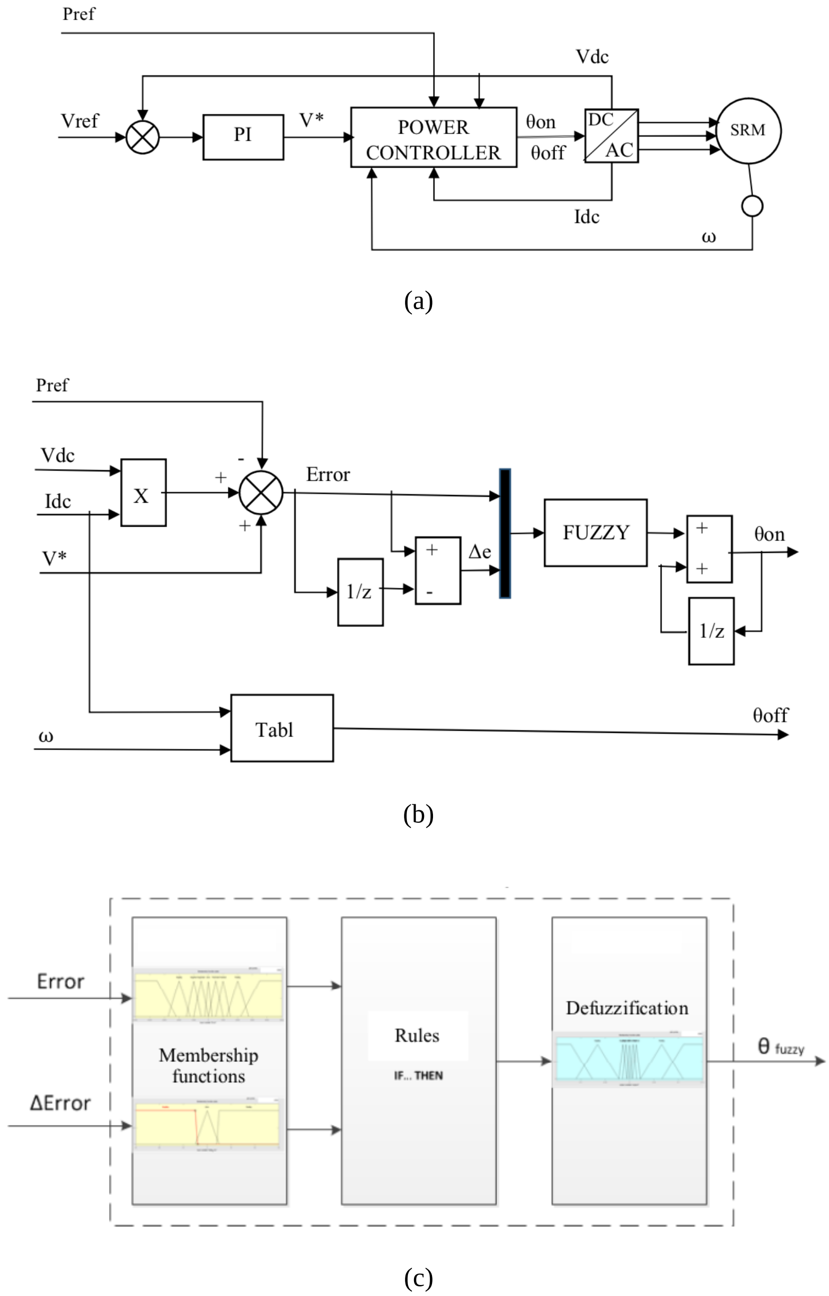

Figure 2.22 Block diagram of the (a) general controller, (b) power controller, and (c) fuzzy controller scheme [2.32].

negative large error to positive large error. Detailed discussion of results is not provided, but the implementation of the fuzzy logic control method was described in informative detail.

A method to represent flux linkage and torque by the sum of sine and cosine components (coefficients) of the waveform harmonics is proposed in [2.33]. Close matching with FEA is achieved by reconstruction of flux with harmonic orders 0, 1, 2, and 3 and harmonic orders 1, 2, and 5 for torque. The bar plots of flux linkage and torque harmonics for various current excitations shown in Figure 2.23 provides insight into harmonic content and impacts from nonlinear magnetic behavior.

SRM Design and Control Optimization

Overall, very few references were identified that involved optimization of both machine design and controls. A mutually coupled (MC) SRM design is presented in [2.34] that
permits bi-polar trapezoidal and sinusoidal excitation from a conventional VSI. As shown in Figure 2.24, similar performance and efficiency is demonstrated in comparison with conventional SRM and to the 2010 Prius PM motor, yet the SRMs have stack lengths of 85 and 87 mm, respectively, vs 50 mm for the PM motor. Efficiencies range from 89.4% to 93.9% at peak loading from base speed to maximum speed. Torque ripple reduction is not a significant focus of the paper, and significant torque ripple is incurred at base speed (160 to 260Nm for 205 Nm avg). Compared to conventional SRM, torque ripple is shown to decrease by 7% and 10% for bi-polar trapezoidal and sinusoidal excitation, respectively. However, it is not mentioned that sinusoidal drive imposes some limit to torque ripple reduction method, compared with conventional SRM drive with independent phase control. The results are encouraging for cases where torque ripple is of minimal concern.

An approach involving axially skewed rotor poles and instantaneous torque control with sinusoidal TSF is presented in [2.35]. This design requires 3D FEA due to skewing of the rotor poles, and therefore significant computation is required for each design point. The skew angle was swept from 0 to 27 degrees, and the nominal pole arc was 27.1 degrees. The smallest torque ripple was found with a skew angle of 17.5 degrees, and based on magneto-static results (where it is presumed ideal current commutation was assumed), a reduction from 32 to 26% from the conventional un-

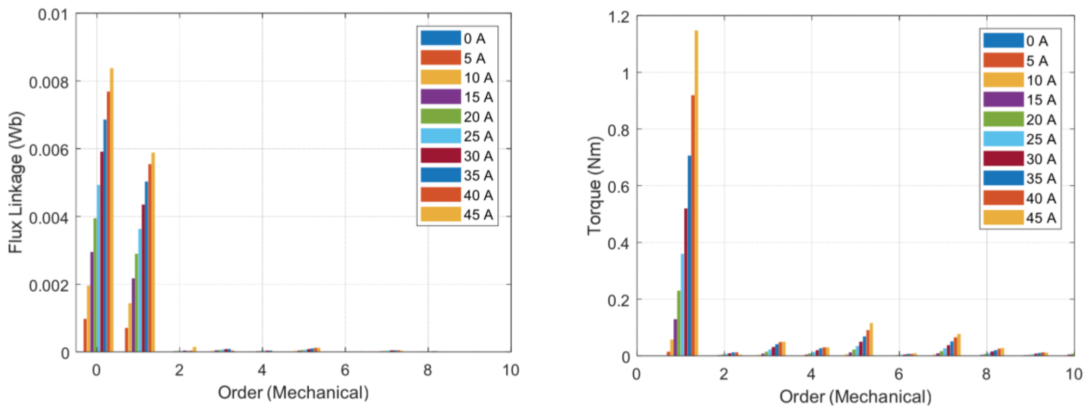

(a) (b)

Figure 2.23 Harmonic decomposition of (a) flux linkage and (b) torque [2.33].

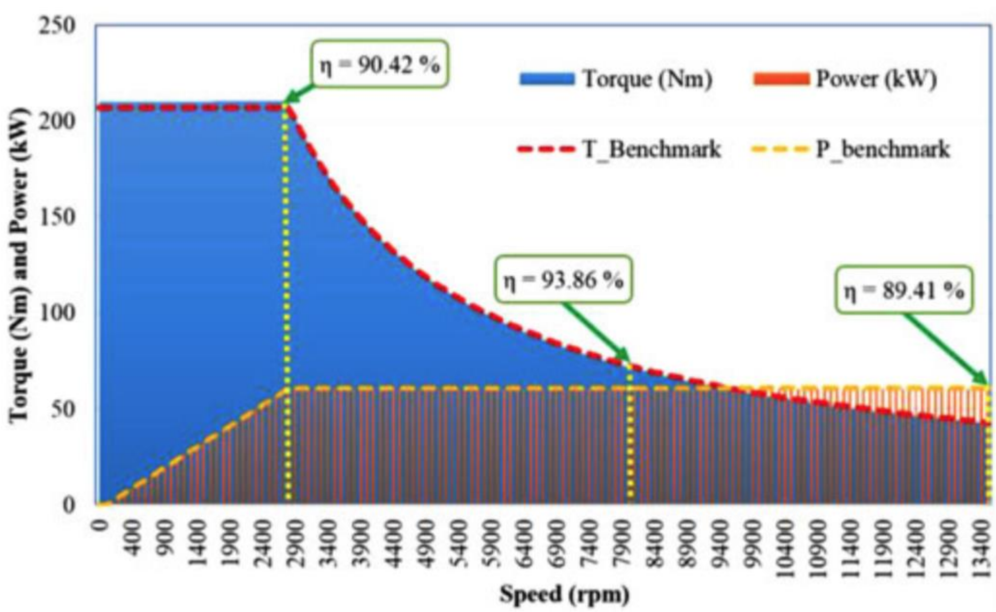

Figure 2.24 Power and torque versus speed for the designed MCSRM [2.34].

skewed rotor to the skewed rotor. The machine design optimization appears to be only magnetostatic, where impacts of voltage limitations are not addressed. Operation was simulated using instantaneous torque control with an outer speed PI loop and a torque sharing function that provides individual phase torque reference, and a corresponding current reference is determined by a look-up table $i(\theta,\tau)$. The importance of anti-windup in the speed controller is noted, and time-based simulation results show unskewed vs. skewed torque ripple is 29.7% versus 20.2%, with average torque being 7.9 Nm versus 6.2 Nm at a given speed. These metrics indicate the trade-off of average torque versus torque ripple, but it is not discussed, and this is a key item to address since skewing will reduce the ratio of aligned and unaligned inductances – the key drive of torque in the SRM. Authors note future work on more sophisticated optimized machines through 3D FEA and better torque control. Overall, very limited analysis is performed through simulation as only one speed and operation point is discussed in moderate detail, and other corresponding operational details such as efficiency and controller performance are not addressed.

Analytical expressions are developed for acoustic noise in [2.36], and dynamic motor models of the SRM are proposed that involve magnetic pressure lookup tables for conventional and mutually coupled SRMs. The magnetic pressure is the calculated air-gap radial magnetic force per unit area from FEA. This is a function of rotor position and is ultimately transformed into spatial orders and temporal harmonics by using two-dimension fast Fourier transformations. Expressions describing the vibration modes of the stator core with windings and frame effect, and furthermore, expressions for displacement amplitude, modal sound power, and modal radiation efficiency are developed to estimate sound power. Dynamic motor models, shown in Figure 2.25, rely on lookup tables to calculate the current, torque, and magnetic pressure as a result of applied voltage. Studies indicate that the MC SRM emits less noise than the conventional SRM, especially at low speeds. It is noted that the conventional SRM configuration is able to produce more torque at high speeds, which may be partially due to the geometry being optimized for conventional excitation. Experimental results indicate relatively close agreement between predicted and measured acoustic noise. While the paper does not address control mitigation methods in detail, it is included in this section since the approach involves time-domain modeling for acoustic noise based on detailed machine FEA.

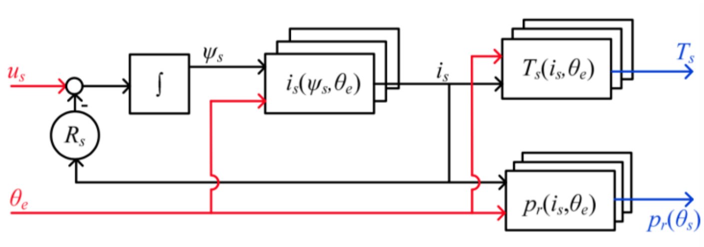

(a)

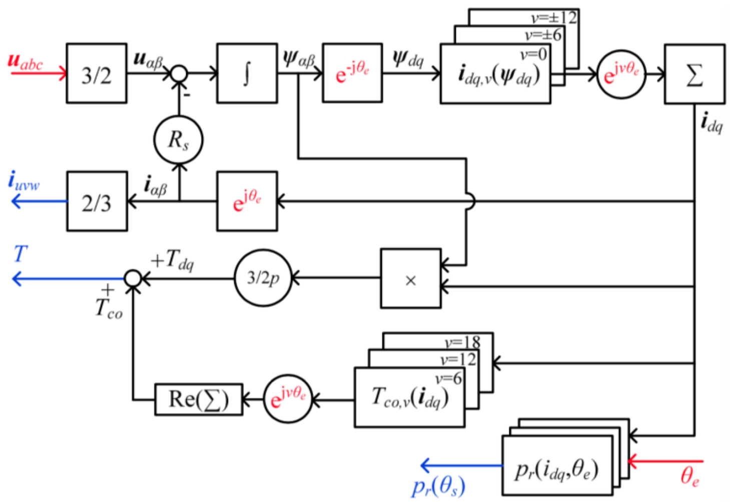

(b)

Figure 2.25 Dynamic motor models of the SRM with magnetic pressure look-up tables for the (a) conventional SRM and (b) MCSRM [2.36].

Three popular multi-objective optimization algorithms (GA), DE, and PSO are systematically evaluated in [2.37] on the design of a 6/4 SRM with seven independent variables and an objective to obtain a strong nonlinear multi-objective Pareto front. To quantify the quality of the Pareto fronts, five quality indicators are used to compare the effectiveness of the algorithms. The three performed similarly for both small and large amounts of candidate designs; however, DE tended to perform better with respect to convergence speed and Pareto front quality with moderate numbers of candidates. Five machine design parameters (stator bore diameter, stack length, rotor and stator angular pole width, and current density) are evaluated using a linear analytical model, then control variables θ_{on} and θ_{off}, and then the saturated inductance profile is adjusted according to the current profile, and ultimately the pareto front is observed with respect to torque density and efficiency, as shown in Figure 2.26. The approach was sufficient for comparison of the three optimization algorithms and for the selection of high-level geometric parameters; however, this approach lacks the fidelity of true machine design optimization due to linear assumptions. Further, details of control and time-based transient performance predictions are not discussed.

Summary

Machine design optimization efforts identified in the literature primarily focus on the reduction of torque ripple and/or acoustic noise. Other design targets include efficiency, torque density, or specific torque (torque per active mass). The most common optimization variables selected to reduce torque ripple through hardware design are the rotor and stator pole angular widths. Some researchers include stator and rotor back-iron thickness in their optimization studies, and a few references investigated pole tip shaping, while others researched impacts of axially skewing the rotor laminations. While some references discussed details associated with the trade-off between torque ripple and average torque, many did not address this important consideration. In general, design changes that reduce torque ripple often reduce the magnetic saliency, and therefore reduce the average torque rating. Further, most design optimization efforts did not consider the dynamic impacts of changes in geometric variables, which is particularly important for determining the peak torque envelope – one of the key design considerations for many applications, particularly vehicle propulsion. It is more straightforward to perform magnetostatic optimization and consider dynamic operation separately for various types of electric machines that are sinusoidally excited

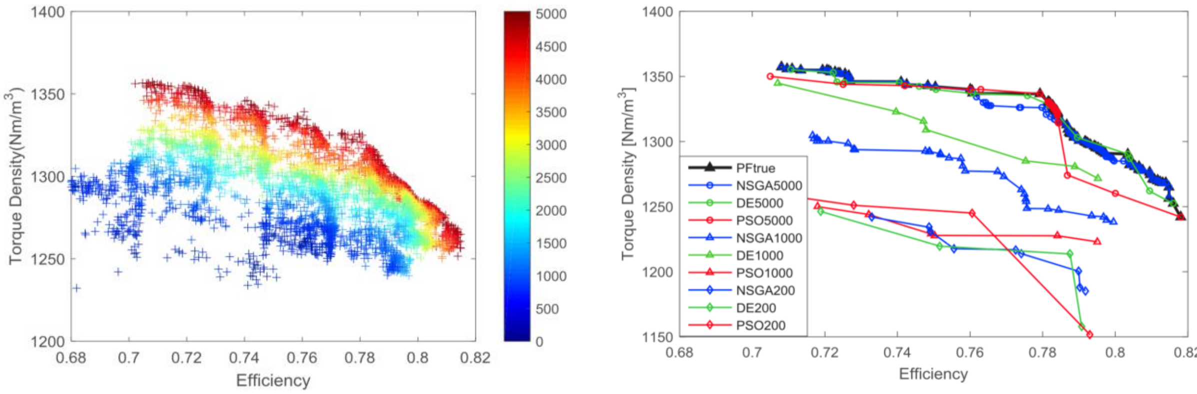

(a) (b)

Figure 2.26 (a) Search results with NGSA-II, (b) comparison of Pareto fronts determined by NGSA-II, DE, and PSO for different numbers of iterations [2.37].

and more continuous in nature versus the discontinuous and nonlinear behavior of the SRM with both current and position. Mutually coupled SRMs use the same geometry but different winding scheme to facilitate the use of conventional three-phase voltage source inverters and sinusoidal excitation. However, moving to this excitation scheme increases end-turn length and more importantly, limits the ability to control phase current individually, and therefore limits the implementation of advanced current profiling for torque ripple reduction. Nonetheless, the configuration may be preferred in some applications where the ability to use a conventional drive outweighs these concerns.

Methods to decrease computational demands of machine design include the use of magnetic equivalent circuits and other closed-form analytic equations to represent machine behavior. While these methods may be good for down-selecting from a broad set of machine considerations, they likely do not have the fidelity needed to perform detailed optimization. Further, their accuracy may deteriorate considerably if advanced or novel features are incorporated into the SRM geometry. Promising methods include FEA-based parameter sensitivity studies and other order reduction methods to reduce the number of optimization variables and the solution space prior to commencing comprehensive FEA-based optimization.

Torque ripple minimization through controls optimization has been researched considerably more than that of SRM hardware design optimization. A vast range of methods have been proposed, including feedback linearization, sliding mode controllers, torque sharing functions, self-training techniques, fuzzy logic controls, advanced neural networks, and many more. Current profiling can yield significant improvements in torque ripple and acoustic noise reductions for much of the operation range. Current profiling is simple in principle, as the current waveform can be shaped to generate near zero torque ripple. However, in application, determination and regulation of the ideal current waveform can be difficult due to the highly nonlinear behavior of torque as a function of current and position. Additionally, for high loads at elevated speeds, voltage limits are encountered, and this mitigation technique becomes limited. A few references include the most interesting approach that considers the absolute rate change of flux linkage as a part of the control system, and therefore voltage limitations and associated controllability are indirectly addressed. Additionally, a few other references present predictive control methods accounting for control loop delays and other discontinuous considerations, which is particularly important at high speeds where voltage limits are approached and the operational frequency becomes closer to the sampling or switching frequency, which may be a limitation due to microcontroller/FPGA or power electronics, respectively.

Similar optimization algorithms have been implemented in both machine design and controller optimization. In general, PSO methods have been reported to be more successful than GA-based algorithms for machine design optimization, while other algorithms such as NGSAII and DE approaches display better performance than PSO for controls optimization.

The literature review has shown that hardware optimization is performed without full consideration of the dynamic operation of the SRM, particularly as it relates to voltage constraints and the impact of geometric parameter variations on the trade-off between torque ripple and the maximum torque versus speed profile. One key reason for this is the vast computational requirements associated with geometric parameter optimization, even if 2D FEA is used. Further, complex control schemes that span the entire operation region are often not feasible to implement for each geometric variation. Online control optimization methods attempt to achieve torque ripple minimization without lookup tables but are limited in the fidelity of the machine model due to memory and computational limitations of the microprocessor/FPGA. Offline control methods can be based on more accurate machine models, but are susceptible to deviations from assumptions in the machine model, such as variances in manufacturing, material properties, etc. Therefore, it is proposed that optimization of the machine is performed with respect to the full dynamic range of the SRM with consideration of voltage limits. Additionally, both offline and online control optimization is proposed to allow for detailed machine models to be leveraged in offline computations, while online learning techniques can update control reference tables based on observer-based computations in practice.

Furthermore, a modeling and optimization framework is proposed that facilitates the co-optimization of SRM design and controller current profiles, while providing the capability to carry out optimization with respect to system parameters and characteristics such as acoustic noise, machine efficiency, converter DC-link current ripple, etc. A list of proposed features and common deficiencies observed in the literature review for various research focus areas is provided in Table 2.1. Very few references use more than two of the proposed features in Table 2.1, and no references were found that include all of the proposed features.

Table 2.1 Deficiencies of State-of-the-Art Approaches.

Research Focus	**Proposed Approach**	**Deficiencies Identified in Literature**
Machine Model	Nonlinear	Linear models are not sufficient for the optimization of geometry or controller for reduced torque ripple and other system parameters.
Controls Optimization	Offline and online	Offline: pre-computed control parameters often lack compensation for gaps between simulation and application Online: computationally limited and effectiveness without offline optimization.
Optimization Area	Both controls and machine	Optimization of the machine or controls alone is greatly inferior to solutions from combined optimization.
Optimization Objective	Multiple Objective	Methods lacking a co-optimization approach often lack the ability to optimize system parameters such as machine efficiency, converter efficiency, etc.
Operation Range	Control strategies for low and high speeds.	Many proposed control approaches are only applicable to specific speed ranges (low or high) or otherwise have limited effectiveness.

References

[2.1] O. Ellabban and H. Abu-Rub, "Switched reluctance motor converter topologies: A review," *2014 IEEE International Conference on Industrial Technology (ICIT)*, 2014, pp. 840-846, doi: 10.1109/ICIT.2014.6895009.

[2.2] M. N. Anwar, I. Husain and A. V. Radun, "A comprehensive design methodology for switched reluctance machines," in *IEEE Transactions on Industry Applications*, vol. 37, no. 6, pp. 1684-1692, Nov.-Dec. 2001, doi: 10.1109/28.968179.

[2.3] T. J. E. Miller, "Optimal design of switched reluctance motors," in *IEEE Transactions on Industrial Electronics*, vol. 49, no. 1, pp. 15-27, Feb. 2002, doi: 10.1109/41.982244.

[2.4] M. Balaji and V. Kamaraj, "Design optimization of Switched Reluctance Machine using Particle Swarm Optimization," *2011 1st International Conference on Electrical Energy Systems*, 2011, pp. 164-169, doi: 10.1109/ICEES.2011.5725322.

[2.5] M. Balaji and V. Kamaraj, "Evolutionary computation based multi-objective pole shape optimization of switched reluctance machine," *International Journal of Electrical Power & Energy Systems*, 2012, vol. 43, pp. 63-69, May 2012, doi: 10.1016/j.ijepes.

[2.6] C. Ma and L. Qu, "Multiobjective Optimization of Switched Reluctance Motors Based on Design of Experiments and Particle Swarm Optimization," *in IEEE Transactions on Energy Conversion*, vol. 30, no. 3, pp. 1144-1153, Sept. 2015, doi: 10.1109/TEC.2015.2411677.

[2.7] W. Peng and J. Gyselinck, "Combined Magnetic-Equivalent-Circuit and Finite-Element modelling of Switched Reluctance Machines," *2016 IEEE International Energy Conference (ENERGYCON)*, 2016, pp. 1-6, doi: 10.1109/ENERGYCON.2016.7513966.

[2.8] J. Zhang, H. Wang, S. Zhu, and T. Lu, "Multi-Physics Multi-Objective Optimal Design of Bearingless Switched Reluctance Motor Based on Finite-Element Method", June 2019, *Energies*, doi: 10.3390/en12122374.

[2.9] P. Azer, B. Bilgin and A. Emadi, "Mutually Coupled Switched Reluctance Motor: Fundamentals, Control, Modeling, State of the Art Review and Future Trends," *in IEEE Access*, vol. 7, pp. 100099-100112, 2019, doi: 10.1109/ACCESS.2019.2930895.

[2.10] M. Ilik-Spong, R. Marino, S. M. Peresada, and D. G. Taylor, "Feedback linearizing control of switched reluctance motors," *in IEEE Transactions on Automatic Control*, vol. AC-32, no. 5.

[2.11] D. G. Taylor, "An experimental study on composite control of switched reluctance motors," *in IEEE Control Systems Magazine*, vol. 11, no. 2, pp. 31-36, Feb. 1991, doi: 10.1109/37.67673.

[2.12] R. C. Kavanagh, J. M. D. Murphy and M. G. Egan, "Torque ripple minimization in switched reluctance drives using self-learning techniques," *Proceedings IECON '91: 1991*

International Conference on Industrial Electronics, Control and Instrumentation, 1991, pp. 289-294 vol.1, doi: 10.1109/IECON.1991.239292.

[2.13] D. E. Cameron, J. H. Lang and S. D. Umans, "The origin and reduction of acoustic noise in doubly salient variable-reluctance motors," *in IEEE Transactions on Industry Applications*, vol. 28, no. 6, pp. 1250-1255, Nov.-Dec. 1992, doi: 10.1109/28.175275.

[2.14] D. S. Schramm, B. W. Williams and T. C. Green, "Torque ripple reduction of switched reluctance motors by phase current optimal profiling," *PESC '92 Record. 23rd Annual IEEE Power Electronics Specialists Conference*, 1992, pp. 857-860 vol.2, doi: 10.1109/PESC.1992.254793.

[2.15] J. C. Moreira, "Torque ripple minimization in switched reluctance motors via bi-cubic spline interpolation," *PESC '92 Record. 23rd Annual IEEE Power Electronics Specialists Conference*, 1992, pp. 851-856 vol.2, doi: 10.1109/PESC.1992.254794.

[2.16] R. S. Wallace and D. G. Taylor, "A balanced commutator for switched reluctance motors to reduce torque ripple," *in IEEE Transactions on Power Electronics*, vol. 7, no. 4, pp. 617-626, Oct. 1992, doi: 10.1109/63.163641.

[2.17] J. Chiasson and L. Tolbert, "High performance motion control of a switched reluctance motor," *IEEE International Electric Machines and Drives Conference* (Cat. No.01EX485), 2001, pp. 425-429, doi: 10.1109/IEMDC.2001.939338.

[2.18] I. Husain and M. Ehsani, "Torque ripple minimization in switched reluctance motor drives by PWM current control," in *IEEE Transactions on Power Electronics*, vol. 11, no. 1, pp. 83-88, Jan. 1996, doi: 10.1109/63.484420.

[2.19] A. M. Omekanda, "A new technique for multidimensional performance optimization of switched reluctance motors for vehicle propulsion," in *IEEE Transactions on Industry Applications*, vol. 39, no. 3, pp. 672-676, May-June 2003, doi: 10.1109/TIA.2003.810632.

[2.20] C. E. Carstensen, N. H. Fuengwarodsakul and R. W. de Doncker, "Flux Linkage Determination for Correct Modeling of Switched Reluctance Machines - Dynamic Measurement versus Static Computation," *2007 IEEE International Electric Machines & Drives Conference*, 2007, pp. 1317-1323, doi: 10.1109/IEMDC.2007.383620.

[2.21] M. Alrifai, M. Zribi, R. Krishnan, and M. Rayan, “Nonlinear Speed Control of Switched Reluctance Motor Drives Taking into Account Mutual Inductance”, *in Journal of Control Science and Engineering*, 2008, doi: 10.1155/2008/491625.

[2.22] M. Alrifai, M. Zribi, M. Rayan, and R. Krishnan, “Speed control of switched reluctance motors taking into account mutual inductances and magnetic saturation effects”, *in Energy Conversion and Management*, 2010, vol. 51, pp. 1287-1297, doi: 10.1016/j.enconman.2010.01.004.

[2.23] R. Mikail, I. Husain, Y. Sozer, M. S. Islam and T. Sebastian, "A Fixed Switching Frequency Predictive Current Control Method for Switched Reluctance Machines," in *IEEE*

Transactions on Industry Applications, vol. 50, no. 6, pp. 3717-3726, Nov.-Dec. 2014, doi: 10.1109/TIA.2014.2322144.

[2.24] H. Makino, T. Kosaka and N. Matsui, "Control performance comparisons among three types of instantaneous current profiling technique for sr motor," *7th IET International Conference on Power Electronics, Machines and Drives (PEMD 2014)*, 2014, pp. 1-6, doi: 10.1049/cp.2014.0393.

[2.25] M. M. Namazi, M. M. Borujeni, A. Rashidi, S. M. S. Nejad and J. Ahn, "Torque ripple reduction of switched reluctance motor drive with adaptive sliding mode control and Particle Swarm Optimization," *2015 IEEE International Conference on Advanced Intelligent Mechatronics (AIM)*, 2015, pp. 371-376, doi: 10.1109/AIM.2015.7222560.

[2.26] J. Ye, P. Malysz and A. Emadi, "A Fixed-Switching-Frequency Integral Sliding Mode Current Controller for Switched Reluctance Motor Drives," in *IEEE Journal of Emerging and Selected Topics in Power Electronics*, vol. 3, no. 2, pp. 381-394, June 2015, doi: 10.1109/JESTPE.2014.2357717.

[2.27] Y. Wei, M. Qishuang, Z. Poming and G. Yangyang, "Torque ripple reduction in switched reluctance motor using a novel torque sharing function," *2016 IEEE International Conference on Aircraft Utility Systems (AUS)*, 2016, pp. 177-182, doi: 10.1109/AUS.2016.7748043.

[2.28] C. Ma, L. Qu, R. Mitra, P. Pramod and R. Islam, "Vibration and torque ripple reduction of switched reluctance motors through current profile optimization," *2016 IEEE Applied Power Electronics Conference and Exposition (APEC)*, 2016, pp. 3279-3285, doi: 10.1109/APEC.2016.7468336.

[2.29] S. Wang, F. Liu and J. Chou, "Design on Sliding Mode Controller with Adaptive Fuzzy Compensation for Switched Reluctance Motor Drive Systems," *2016 International Symposium on Computer, Consumer and Control (IS3C)*, 2016, pp. 239-242, doi: 10.1109/IS3C.2016.71.

[2.30] Harikrishnan R. and F. M. Fernandez, "Improved online torque-sharing-function based low ripple torque control of Switched Reluctance Motor Drives," *2016 IEEE International Conference on Power Electronics, Drives and Energy Systems (PEDES)*, 2016, pp. 1-6, doi: 10.1109/PEDES.2016.7914374.

[2.31] N. Saha, A. Panda, and S. Panda, “Speed control with torque ripple reduction of switched reluctance motor by many optimizing liaison technique”, in *Journal of Electrical Systems and Information Technology*, vol. 5, doi: 10.1016/j.jesit.2016.12.013.

[2.32] J. A. Domínguez-Navarro, J. S. Artal-Sevil, H. A. Pascual and J. L. Bernal-Agustín, "Fuzzy-logic strategy control for switched reluctance machine," *2018 Thirteenth International Conference on Ecological Vehicles and Renewable Energies (EVER)*, 2018, pp. 1-5, doi: 10.1109/EVER.2018.8362403.

[2.33] P. Pramod, P. Nuli, R. Mitra and S. Mehta, "Modeling and Simulation of Switched Reluctance Machines for Control and Estimation Tasks," *2019 IEEE International Electric*

Machines & Drives Conference (IEMDC), 2019, pp. 565-570, doi: 10.1109/IEMDC.2019.8785081.

[2.34] M. A. Kabir and I. Husain, "Design of Mutually Coupled Switched Reluctance Motors (MCSRMs) for Extended Speed Applications Using 3-Phase Standard Inverters," in *IEEE Transactions on Energy Conversion*, vol. 31, no. 2, pp. 436-445, June 2016, doi: 10.1109/TEC.2015.2499086.

[2.35] D. Marcsa, and M. Kuczmann, "Design and control for torque ripple reduction of a 3-phase switched reluctance motor", *in Computers & Mathematics with Applications*, vol. 74, doi: 10.1016/j.camwa.2017.01.001.

[2.36] J. Dong et al., "Hybrid Acoustic Noise Analysis Approach of Conventional and Mutually Coupled Switched Reluctance Motors," in *IEEE Transactions on Energy Conversion*, vol. 32, no. 3, pp. 1042-1051, Sept. 2017, doi: 10.1109/TEC.2017.2672741.

[2.37] S. Zhang, S. Li, R. G. Harley and T. G. Habetler, "Performance evaluation and comparison of multi-objective optimization algorithms for the analytical design of switched reluctance machines," in *CES Transactions on Electrical Machines and Systems*, vol. 1, no. 1, pp. 58-65, March 2017, doi: 10.23919/TEMS.2017.7911109.

CHAPTER THREE: A FRAMEWORK FOR MULTIPLE OBJECTIVE CO-OPTIMIZATION OF SWITCHED RELUCTANCE MACHINE DESIGN AND CONTROL

Portions of this chapter were originally published by Timothy Burress and Dr. Leon Tolbert:

T. Burress and L. M. Tolbert, "A Framework for Multiple Objective Co-Optimization of Switched Reluctance Machine Design and Control," *2021 IEEE Transportation Electrification Conference & Expo (ITEC)*, 2021, pp. 1-6, doi: 10.1109/ITEC51675.2021.9490155.

Abstract

A new modeling and optimization approach is proposed for co-optimization of both switched reluctance machine (SRM) design and control across the entire torque-speed operation range. A unique method uses static finite element analysis (FEA) results to determine optimal control conditions for discrete speeds, torques, and torque ripple levels, and the associated voltage profiles are computed using steady state equations without time-domain simulations. Particle swarm optimization is implemented to determine optimal current profiles with the consideration of voltage limits, torque ripple, and other system parameters. For moderate to high speeds where the SRM is near voltage limit conditions, a method was developed to determine optimal control conditions based on a performance function with weighted scalars for torque ripple and efficiency. Further, a machine design optimization method is proposed that leverages outputs from control optimization determines quality metrics for each design based on efficiency and torque ripple across the operation region of the SRM. A key benefit of the overall proposed approach is that a wide range of machine design parameters and control conditions can be swept and based on the needs of an application, the designer can select the appropriate geometry, winding, and control approach based on various performance functions that consider torque ripple, efficiency, and other metrics.

Overview

The limited accuracy associated with applying closed form solutions for performing SRM design optimization have been demonstrated in the literature. Advanced optimization of SRM hardware requires FEA-based modeling to account for operational intricacies of SRMs such as non-linear magnetics and irregular excitation. Since determination of optimal SRM control parameters across the operation region is a complex process, common SRM design methods implemented in literature involve optimization of operational metrics such as torque and torque ripple targets under static conditions. This is largely due to the significant computational requirements associated with transient FEA simulations. A framework is proposed in this chapter that consists of co-optimization of both SRM design and control using static FEA-based machine models with steady state modeling for optimization with respect to voltage and other system parameters throughout the torque-speed operation region.

Proposed Modeling and Optimization Framework

The proposed modeling and optimization framework, shown in Figure 3.1, includes FEA-based machine modeling while addressing computational constraints of transient FEA. This framework includes many simulation tools that can be used in various ways to achieve design and control optimization and a proposed process is discussed later. These tools make use of magnetostatic FEA to map flux linkage and torque as a function of current and rotor position. According to (2.1), partial derivatives of the flux linkage can be used in the voltage equation to represent dynamic operation of the SRM. Code-based voltage fed and steady state current fed machine models were developed to perform dynamic simulations using outputs from magnetostatic FEA. Machine design optimization is based on results from the current and voltage fed models where the maximum torque envelope, optimal current profiles, control conditions, and other operational characteristics are determined across the entire torque-speed operation region with consideration of voltage and torque ripple constraints. Operational constraints related to low and high-speed control parameters are directly addressed by this framework, allowing for machine design optimization to be carried out with consideration of dynamic operation without timely FEA transient simulations. Simulink models were developed to emulate on-line control methods and to provide the capability to include other system components such as source and converter models. The Simulink model can call the voltage fed machine model or directly link with Ansys to perform transient FEA co-simulation. This co-simulation link is used to validate the code-based voltage fed model and to aid in parameter correlation between post processed magnetostatic results and direct transient FEA, such as with core loss or radial force estimation for qualitative acoustic noise assessments.

As management of torque ripple is particularly important for rotor positions where multiple phases produce torque, the multi-phase voltage equation (3.1) with consideration of mutual coupling was

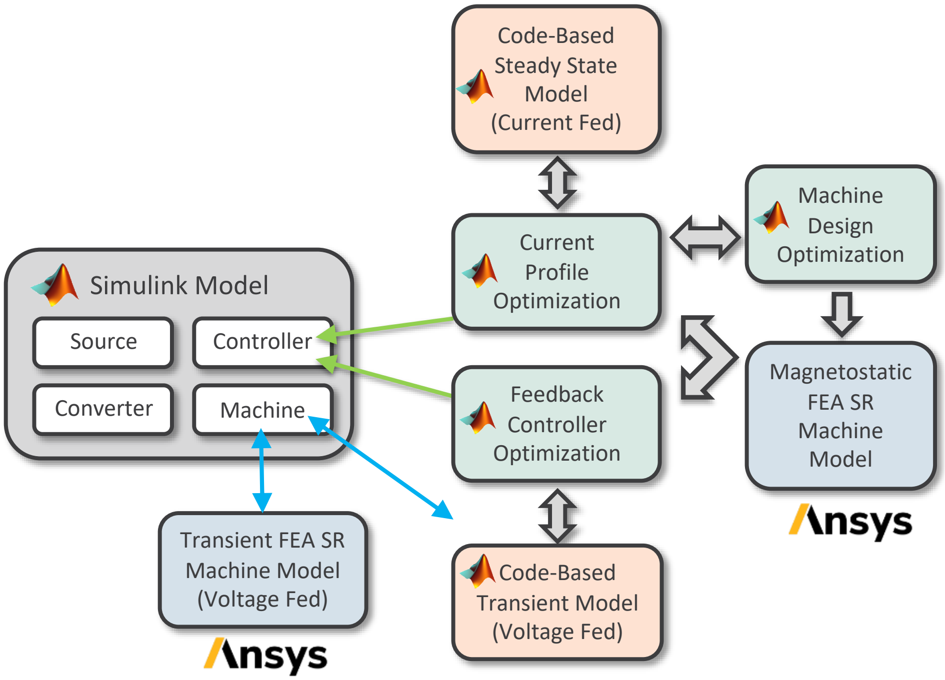

Figure 3.1 Proposed modeling and optimization framework that includes existing and novel modeling tools, optimization code, and their interconnections used for development and validation of unique multiple objective optimization of SRM design and control.

implemented in a code-based current fed model. Diagonal elements of the matrix with flux linkage partial derivatives in the second term correlate with the incremental inductance, and the off-diagonal elements correlate with the incremental mutual inductance between phases. Flux linkage data output from magnetostatic FEA are combined into a four-dimensional matrix (3.2), as they are defined across variations of all three phase currents and rotor position.

A code-based voltage fed transient model, implemented using (3.3), computes the incremental current over time as a result of an applied voltage. Implementation of (3.3) is not as straightforward or efficient as (3.1) since the inverse of the impedance matrix must be computed, and in some cases, singularities may result from certain flux or current conditions. Countermeasures were implemented by applying approximations to avoid taking the inverse of sparse matrices that result in errors during the inverse calculation without considerable impact on the overall computation. Furthermore, the voltage fed equation (3.3) must be solved discretely in the time domain and in the case of voltage pulse excitation, initial conditions are difficult to predict, requiring multiple cycles to be carried out until a condition of steady state is determined. This process was automated with code, and the voltage fed simulator was used for determination of optimal control conditions for moderate to high speeds where the SRM is near voltage limits, while the current fed simulator was used to determine optimal current profiles for low to moderate speeds.

$$\begin{bmatrix} v_a \\ v_b \\ v_c \end{bmatrix} = R \begin{bmatrix} i_a \\ i_b \\ i_c \end{bmatrix} + \begin{bmatrix} \frac{\partial \psi_a}{\partial i_a} & \frac{\partial \psi_a}{\partial i_b} & \frac{\partial \psi_a}{\partial i_c} \\ \frac{\partial \psi_b}{\partial i_a} & \frac{\partial \psi_b}{\partial i_b} & \frac{\partial \psi_b}{\partial i_c} \\ \frac{\partial \psi_c}{\partial i_a} & \frac{\partial \psi_c}{\partial i_b} & \frac{\partial \psi_c}{\partial i_c} \end{bmatrix} \frac{d}{dt} \begin{bmatrix} i_a \\ i_b \\ i_c \end{bmatrix} + \begin{bmatrix} \frac{\partial \psi_a}{\partial \theta} \\ \frac{\partial \psi_b}{\partial \theta} \\ \frac{\partial \psi_c}{\partial \theta} \end{bmatrix} \omega \tag{3.1}$$

$$\begin{bmatrix} \psi_a \\ \psi_b \\ \psi_c \end{bmatrix} = \begin{bmatrix} \psi_a(i_a, i_b, i_c, \theta) \\ \psi_b(i_a, i_b, i_c, \theta) \\ \psi_c(i_a, i_b, i_c, \theta) \end{bmatrix} \tag{3.2}$$

$$\frac{d}{dt}\begin{bmatrix} i_a \\ i_b \\ i_c \end{bmatrix} = \begin{bmatrix} \frac{\partial \psi_a}{\partial i_a} & \frac{\partial \psi_a}{\partial i_b} & \frac{\partial \psi_a}{\partial i_c} \\ \frac{\partial \psi_b}{\partial i_a} & \frac{\partial \psi_b}{\partial i_b} & \frac{\partial \psi_b}{\partial i_c} \\ \frac{\partial \psi_c}{\partial i_a} & \frac{\partial \psi_c}{\partial i_b} & \frac{\partial \psi_c}{\partial i_c} \end{bmatrix}^{-1} \left\{ \begin{bmatrix} v_a \\ v_b \\ v_c \end{bmatrix} - R \begin{bmatrix} i_a \\ i_b \\ i_c \end{bmatrix} - \begin{bmatrix} \frac{\partial \psi_a}{\partial \theta} \\ \frac{\partial \psi_b}{\partial \theta} \\ \frac{\partial \psi_c}{\partial \theta} \end{bmatrix} \omega \right\} \tag{3.3}$$

Magnetostatic FEA Model

With broad parametric optimization in mind, many efforts were made to facilitate efficient FEA calculations for each design. It can be assumed that a maximum of two phases operate simultaneously based on flux linkage and torque profiles shown in Figures 2.2 and 2.3 respectively. Furthermore, only 120 degrees of the electrical cycle needs to be mapped since the characteristics of three-phase SRM repeat on this interval. Even so, a coarse mapping with 10 current levels for each of the two phases and 12 positions (10-degree steps over 120 degrees) yields 1200 cases. This correlates with a computational time of several hours to several days for typical high performance desktop computers depending on mesh density, computational power, and the ability to solve cases in parallel. An SRM with 12 stator teeth and 8 rotor teeth was selected as the base design as it is a three-phase machine which simplifies implementation of the SRM drive compared to machines with a greater number of phases. Further, the selection of the number of rotor teeth is a trade-off among several considerations including higher operational frequencies and thus higher core losses associated with a greater number of rotor teeth versus higher torque ripple with fewer rotor teeth. An example of the geometry and mesh density is provided in Figure 3.2. A quarter model was setup with symmetrical boundary conditions to decrease computational time. Two dimensional magnetostatic FEA simulations were carried out in Ansys, and while there are built-in tools for calculating winding flux linkage in transient FEA packages, they are not available in most magnetostatic FEA environments. Therefore, to avoid transient FEA, a method was developed to calculate flux linkage for each case. The relationship between the magnetic field, *H*, and the vector potential of the magnetic field, *A*, can be described by

$$\mu_0 H = \nabla \times A \tag{3.4}$$

The flux passing through a surface is expressed by the surface integral

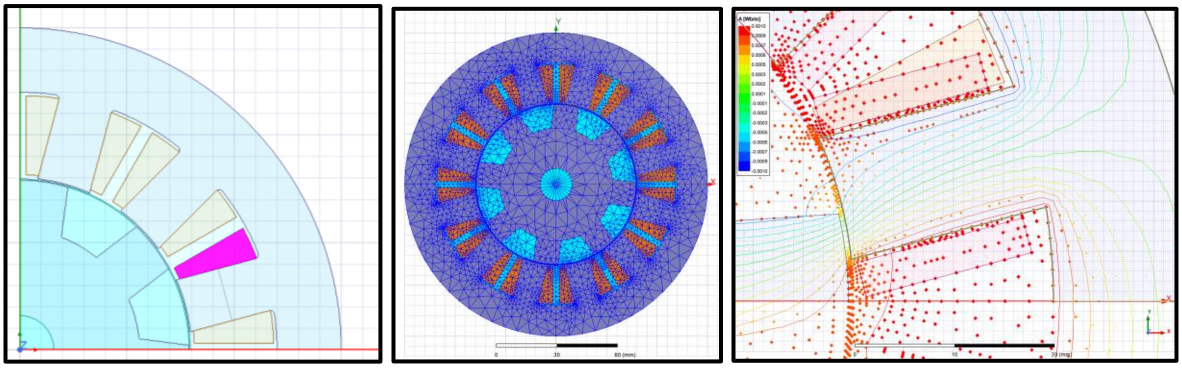

(a) (b) (c)

Figure 3.2 Example 12-8 SRM (a) stator, rotor, and winding geometry, (b) FEA mesh for solving Maxwell's equations, and (c) magnetic vector potential used for determining flux linkage.

$$\lambda = \int_S \nabla \times A \, da \tag{3.5}$$

Stokes theorem can be applied and flux can be expressed as an integral of the contour enclosing the surface:

$$\lambda = \oint_C A \, dS \tag{3.6}$$

Assuming directions of the flux vectors are only in a two-dimensional plane (which is already assumed in 2D FEA), in the x-y plane of the Cartesian coordinate system, for example, and considering a rectangular-shaped contour orthogonal to that plane, flux linkage between the two sides oriented in the z-direction can be defined as

$$\lambda = l(A_{z2} - A_{z1}) \tag{3.7}$$

where l is the length of the contours in the z direction and A_{z2} and A_{z1} are the vector potentials of the magnetic field at points along the z-oriented sides of the contour. For 2D FEA, A_z is computed as a part of the solving process and is already provided as an output.

In the case of a concentrated winding on an SRM stator tooth, (3.7) can be extended to calculate flux linkage in the coil by computing the surface integral of the z-component of the vector potential across each cross-section of a coil:

$$\psi = N_t \lambda = N_t l \left(\frac{1}{A_{coil2}} \int_{S2} A_z dS - \frac{1}{A_{coil1}} \int_{S1} A_z dS \right) \tag{3.8}$$

where N_t is the number of turns, A_{coil2} and A_{coil1} is the cross-sectional area of each half of the coil, and l is equal to the stator stack length. This method was implemented and verified by calculating torque using the co-energy method described by (2.6) and comparing with the calculated torque result from FEA.

In addition to outputting torque and flux linkage, other parameters can be output for post processing of various dynamic behavior and parameter related operation constraints. For example, radial forces in specific locations were mapped for post processing and qualitative analysis of vibration and acoustic noise. The FEA model is parametrically defined such that the cross-sectional area of the coil changes appropriately with parameterized features such as stator tooth width. Coil cross-sectional area is output for each design since current capacity (and therefore maximum torque capability) is dependent on the cross-sectional area of the coil and the allowable current density. These limits are applied in post processing and considered as a part of the machine design optimization process.

Calculation of Winding Parameters for Transient Simulations

A formula was derived to calculate the appropriate number of turns, N_{turns}, and strands, $N_{strands}$, based on an assumed slot fill factor, FF, a given wire cross-sectional area, A_{wire}, coil cross-sectional area, A_{coil}, number of parallel branches in a phase, N_{par}, targeted nominal current density, J_0, and phase current rating, I_{ph}:

$$N_{strands} = nearest\left(\frac{I_{ph}\, FF}{A_{wire}\, J_0\, N_{par}}\right) \tag{3.9}$$

$$N_{turns} = nearest\left(\frac{J_0\, A_{coil} N_{par}}{I_{ph}}\right) \tag{3.10}$$

Values for $N_{strands}$ and N_{turns} are the nearest integer of the ratio defined in parentheses. Conventional stators wound with stranded wire typically have a fill factor in the range of 0.25 to 0.5. Wire cross-sectional area, A_{wire}, is determined by the gauge of wire and coil cross-sectional area, A_{coil}, is determined by area available in the slot for a coil. The 12-8 SRM analyzed in this work has a total of four coils per phase, therefore N_{par} can be 1, 2, or 4. The targeted nominal current density correlates with the anticipated losses and selected cooling approach, and phase current rating may be selected based on thermal limitations of the SRM or the current rating of the devices in the motor drive.

Calculation of Phase Resistance and Resistance Losses

The resistance of the phase windings can be approximated based on geometric parameters and winding specifications. First, the temperature-dependent resistivity of copper is defined by:

$$\rho(T) = \rho_{20^\circ\mathrm{C}}(1 + \alpha(T - 20\ ^\circ\mathrm{C})) \tag{3.11}$$

where T is the average operational temperature of the windings, α is the temperature coefficient of copper per °C, and the resistivity of copper at 20 °C, $\rho_{20°C}$, is 1.724x10^{-8} Ω-m. The DC resistance of a copper wire per unit length can be defined by:

$$R_L = \frac{\rho}{A_{wire}} \tag{3.12}$$

and the DC resistance of a coil can be defined as:

$$R_{coil} = \frac{N_{turns}}{N_{strands}} 2R_L(l_{stack} + 2l_{ext} + l_{arc}) \tag{3.13}$$

where l_{stack} is the axial length of the stator, l_{ext} is the average distance the end-turns extend beyond the stator prior to bending, and l_{arc} is the arclength of the end-turn. The total DC resistance of a phase given by:

$$R_{phase} = \frac{R_{coil}N_{ser}}{N_{par}} \tag{3.14}$$

where N_{ser} is the number of coils in series per phase.

A New SRM Core Loss Calculation Method Based on Mapped Flux Linkage

A method was developed to approximate core losses in the proposed current fed and voltage fed transient models using flux linkages mapped in magnetostatic FEA. Using the stator sections defined in Figure 3.3, the flux density for each tooth can be approximated by using the mapped flux linkage versus position and current, and then dividing by the cross-sectional area of the tooth. For example, the average flux density in tooth 1 of phase A can be defined by:

$$B_{A1} = \frac{\psi_{A1}(i_a, i_b, i_c, \theta_e)}{N_t w_{Stooth} l_{stack}} \tag{3.15}$$

where w_{Stooth} is the average stator tooth width and l_{stack} is the stack length. Flux linkage in the back-iron segments can be correlated to tooth flux linkages by implementing a method similar to Kirchoff's current law. For example, the flux linkage in back-iron segment 'CB1' can be expressed by two different equations:

$$\psi_{CB1} = \psi_{C1} - \psi_{AC1} \tag{3.16}$$

and

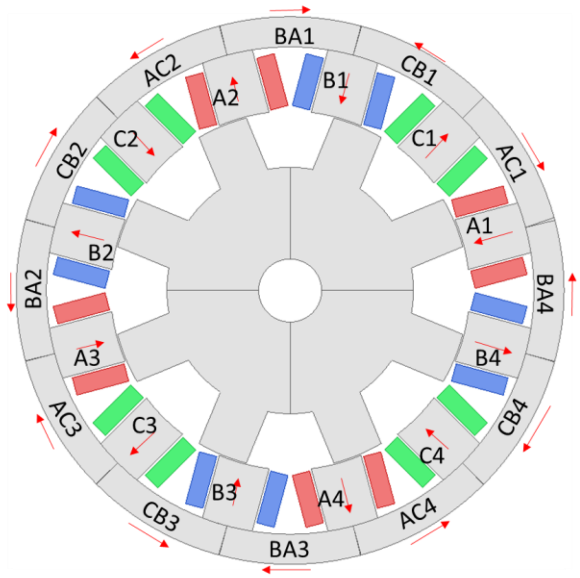

Figure 3.3 Stator and rotor sections identified to calculate transient core losses using flux linkages mapped during magnetostatic simulations.

$$\psi_{CB1} = \psi_{B1} - \psi_{BA1} \tag{3.17}$$

After expressions for the back-iron segment flux linkage are derived, they can be equated and combined with other back-iron segment flux linkage definitions to redefine each of them with respect to only stator tooth flux linkages. Then, the flux density is obtained by dividing by the cross-section area perpendicular to the direction of the average flux density vector, and expressions for the first three segments are:

$$B_{AC1} = \frac{\psi_{A1} - \psi_{B1} + \psi_{C1}}{2N_t w_{yoke} l_{stack}} \tag{3.18}$$

$$B_{BA1} = \frac{\psi_{A1} + \psi_{B1} - \psi_{C1}}{2N_t w_{yoke} l_{stack}} \tag{3.19}$$

$$B_{CB1} = \frac{-\psi_{A1} + \psi_{B1} + \psi_{C1}}{2N_t w_{yoke} l_{stack}} \tag{3.20}$$

Therefore, mapped coil flux linkages are used to directly approximate flux density in various sections of the stator core without direct dependence on position. Expressions for average flux density in the rotor core are position dependent and average flux density in the rotor teeth can be expressed by:

$$B_{RT1} = \frac{\psi_\alpha - \psi_\beta + \psi_\gamma}{2N_t w_{Rtooth} l_{stack}} \tag{3.21}$$

$$B_{RT2} = \frac{-\psi_\alpha + \psi_\beta - \psi_\gamma}{2N_t w_{Rtooth} l_{stack}} \tag{3.22}$$

where w_{Rtooth} is the average width of the rotor tooth, and ψ_α, ψ_β, and ψ_γ are flux linkages defined with respect to a rotating reference frame:

$$\psi_\alpha = \begin{cases} \psi_a & (0 \leq \theta_e < 120°) \\ \psi_b & (120 \leq \theta_e < 240°) \\ \psi_c & (240 \leq \theta_e < 360°) \end{cases} \tag{3.23}$$

$$\psi_\beta = \begin{cases} \psi_b & (0 \leq \theta_e < 120°) \\ \psi_c & (120 \leq \theta_e < 240°) \\ \psi_a & (240 \leq \theta_e < 360°) \end{cases} \tag{3.24}$$

and

$$\psi_\gamma = \begin{cases} \psi_c & (0 \le \theta_e < 120°) \\ \psi_a & (120 \le \theta_e < 240°) \\ \psi_b & (240 \le \theta_e < 360°) \end{cases} \tag{3.25}$$

Similarly, the average flux density in the rotor back-iron segments can be defined as:

$$B_{RH1} = B_{RT2} - B_{RT1} \tag{3.26}$$

$$B_{RH2} = B_{RT1} - B_{RT2} \tag{3.27}$$

With flux densities in rotor and stator defined as a function of stator coil flux linkages, core losses can be computed with the time-domain equations implemented in Ansys Maxwell [3.1], where hysteresis loss is defined as

$$p_h(t) = \left\{ \left| H_x \frac{dB_x}{dt} \right|^{\frac{2}{\beta}} + \left| H_y \frac{dB_y}{dt} \right|^{\frac{2}{\beta}} + \left| H_z \frac{dB_z}{dt} \right|^{\frac{2}{\beta}} \right\}^{\frac{\beta}{2}} \tag{3.28}$$

where the suggested value for β is 2 in [3.1], and magnitudes for the magnetic fields H_x, H_y, and H_z are determined by

$$H_m = \frac{1}{\pi} k_h B_m \tag{3.29}$$

Eddy current loss is defined as

$$p_c(t) = \frac{1}{2\pi^2} k_c \left\{ \left(\frac{dB_x}{dt}\right)^2 + \left(\frac{dB_y}{dt}\right)^2 + \left(\frac{dB_z}{dt}\right)^2 \right\} \tag{3.30}$$

and excess loss is expressed as

$$p_e(t) = \frac{1}{C_e} k_e \left\{ \left(\frac{dB_x}{dt}\right)^2 + \left(\frac{dB_y}{dt}\right)^2 + \left(\frac{dB_z}{dt}\right)^2 \right\}^{0.75} \tag{3.31}$$

The loss equations were modified to be of a singular dimension based on the assumed radial direction of flux vectors in the rotor and stator teeth and assumed circumferential direction of flux vectors in the rotor and stator back-iron. A comparison study was conducted to analyze the accuracy of the proposed loss approximation method by simulating the same geometry, operating conditions, and control technique in transient electromagnetic FEA and the proposed code-based transient simulation environment. Time-domain core loss waveforms from simulations discussed in more detail in Chapter 4 are shown for back-iron segment 'AC1' shown in Figure 3.4(a) show very close agreement between FEA and the proposed method. However, comparison of core losses in tooth 'A1' shown in Figure 3.4(b) show greater error. This error is likely due to localized transients in the magnetic field near the airgap that cannot be accounted for using coil flux linkage mapping which captures only average flux density. Future work can be done to improve this approach by using correlation factors based on rotor rotation, or a more accurate approach using spatial mapping of the flux density for areas near the airgap where the error of the flux linkage-based approximation method is higher. Nonetheless, the time-average of the approximated total core loss is close to FEA and combined with the considerable computational advantages of the proposed transient environment, loss estimation can be performed as a wide range of hardware and control parameters are swept and optimized.

Machine Design Optimization Process

The proposed multi-stage machine design optimization process is shown in Figure 3.5. Two down-selection stages are implemented to reduce the solution space prior to implementation of the more computationally intensive off-line control optimization that uses a current-fed steady state model to determine optimal current-profiles throughout the operation region. Stages in the flowchart are color-coded according to the areas identified in the torque-speed operation map included with the flowchart. Following the determination of fixed and variable design parameters, two primary stages are implemented to yield a down-selection of viable designs. In the first stage, static FEA is performed for at least two current values to determine torque and current density associated with single phase operation at coarse position increments over the 180-degree positive torque production stroke. Simulations are carried out at the zero-speed condition with one current value corresponding to near maximum torque and the other current value corresponding to a moderate torque to help determine an initial solution space (geometric variables for a set of designs), adjust nominal parameters if necessary, iterate on the initial design set, and establish a fundamental understanding of the sensitivity of geometric parameters in relation to operational quantities such as average torque, torque ripple, and current density. The latter is particularly important to provide insight in the formation of the optimization fitness function that is implemented in various stage of the design process.

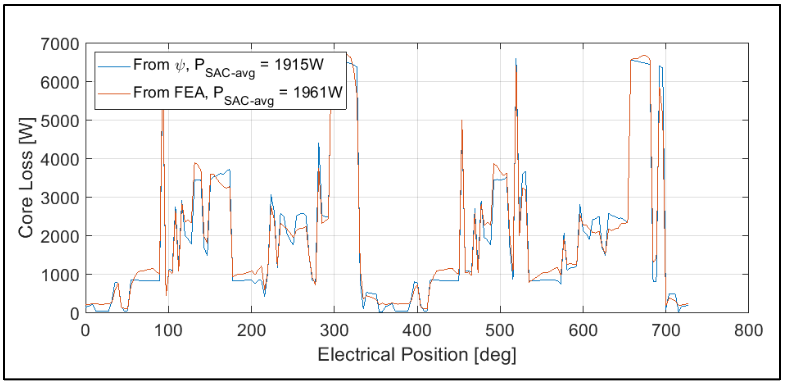

(a)

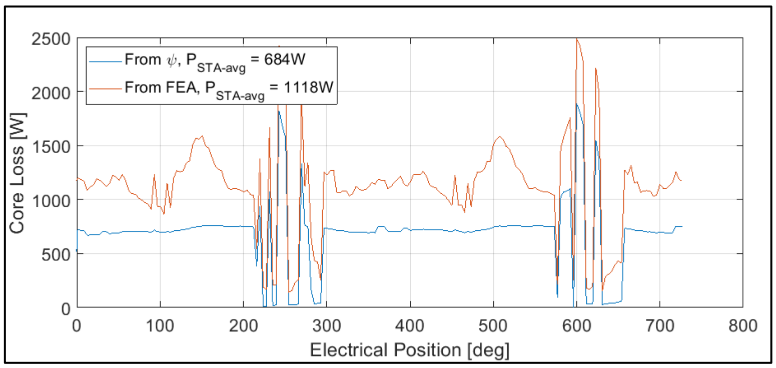

(b)

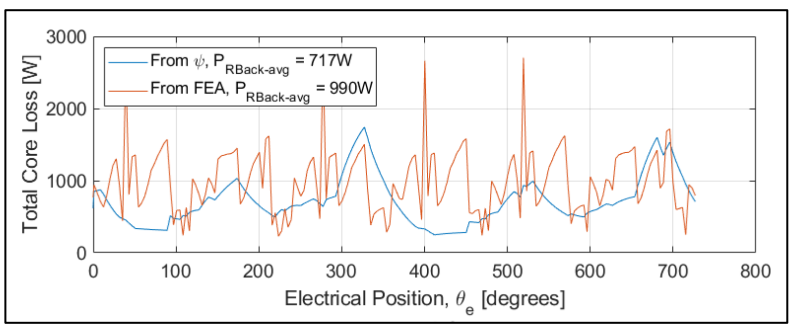

(c)

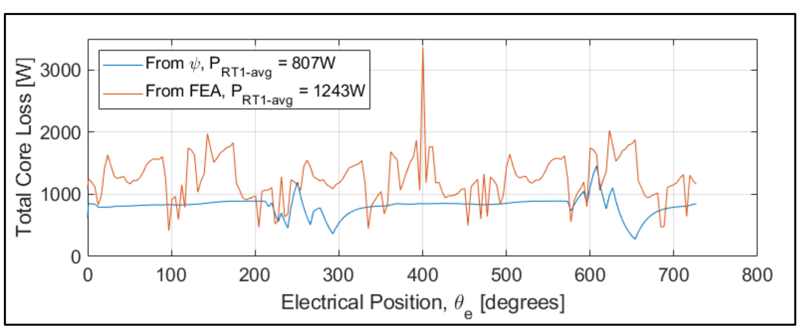

(d)

Figure 3.4 Comparisons of approximated and transient FEA core loss for the stator back-iron segment (a), stator tooth (b), rotor back-iron (c), and rotor tooth (d).

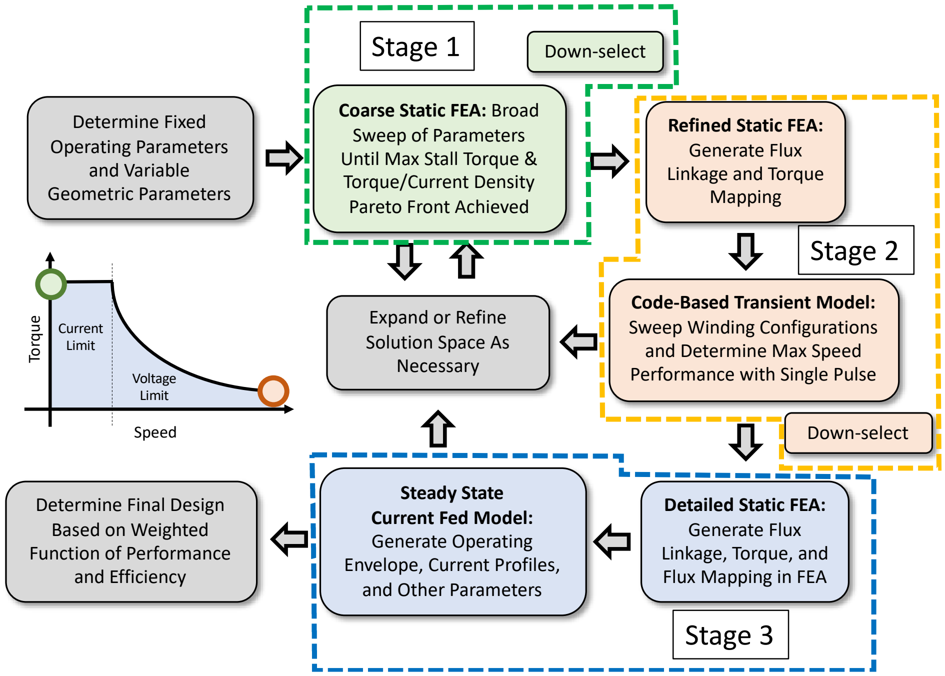

Figure 3.5 Proposed stages within overall SRM design and control optimization approach include two geometry down-selection stages at maximum performance for zero and maximum speed prior to the more computationally intensive off-line control optimization performed in Stage 3.

In the second stage, maximum speed performance of the reduced design set is analyzed using flux linkage and torque mapping from more refined static FEA simulations. This step facilitates selection of various winding configurations, refinement of geometric parameters, more exploration of the solution space as necessary, and further reduction of the design set prior to multi-objective co-optimization of design and control parameters for the remaining operation region using the proposed framework.

After design exploration and down-selection in Stages 1 and 2, more detailed flux and torque maps are generated with static FEA which are used by a function in Stage 3 that generates optimal current profiles with respect to torque ripple and voltage constraints. Other steps in Stage 3, as shown in Figure 3.6, includes the generation of operation envelopes for each design variation and determining the value of each design based on a performance function, then potentially further design exploration depending on design goals and the current status of the design set. After control optimization is completed in Stage 3, the value of each machine design is determined by a performance function evaluating operational metrics such as efficiency and torque ripple at various points throughout the torque-speed range. The solution space is expanded as necessary in Stages 2 and 3 based on machine performance values, and new points in the solution space may be identified by using an evolutionary algorithm such as particle swarm optimization if the number of design parameters is high or if machine performance function is complex.

Novel Method to Generate Current Profiles for Torque Ripple Mitigation

A new method for determining optimal current profiles for torque ripple mitigation was developed and can be implemented during Stage 3 control optimization efforts. Optimal current profiles for torque ripple minimization are generated using four-dimensional interpolation of the torque matrix. For zero torque ripple, current combinations are computed directly from the 4D torque matrix at each position. An example of current, voltage, flux-linkage, and torque waveforms associated with minimal current (k=1) with zero torque ripple is shown in Figure 3.7. In contrast to methods reviewed in the literature, multiple current profiles are selected that match the targeted torque and torque ripple allowance, and then are sorted with respect to maximum torque per ampere (MTPA). This can be described by an array of current profiles:

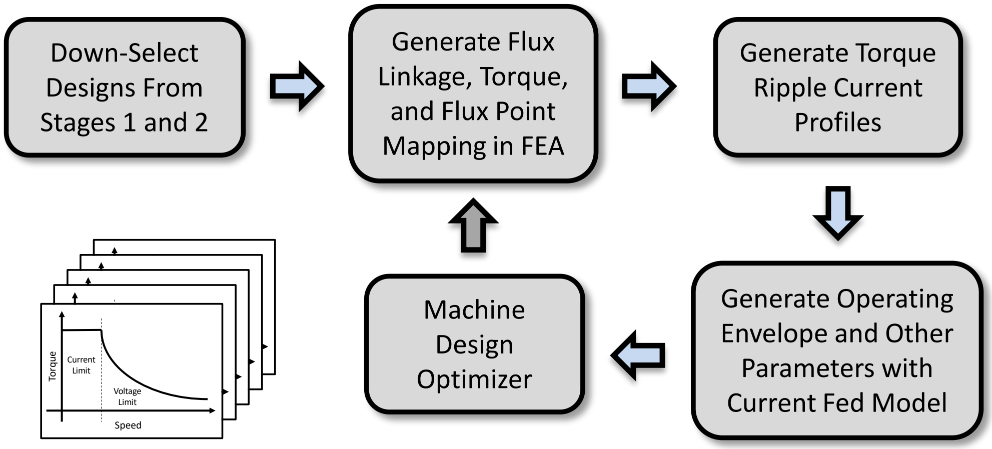

Figure 3.6 Current profile optimization can be implemented in Stage 3 as arrays of voltage-constrained current profiles are generated for each torque and speed condition and this stage also includes machine design optimization that uses key points from the operating envelopes to gauge the value of each design and generate new design variations using particle swarm optimization.

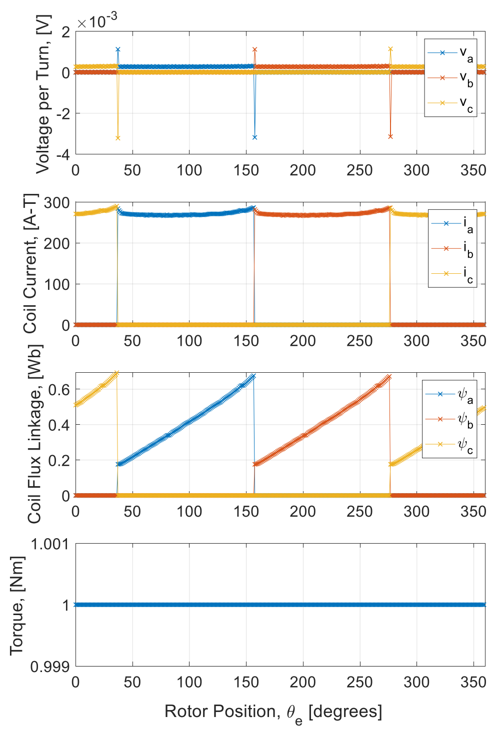

Figure 3.7 Exemplar current profiles generated by the proposed control optimizer demonstrate that zero percent torque ripple can be achieved under some conditions, and associated voltage, flux, and torque waveforms demonstrate that the control optimizer incorporates transient modeling capability based on static flux mapping.

$$i_{profile} = i(\tau_{avg}, \tau_r, k, \theta) \tag{3.32}$$

where τ_{avg} is an array of targeted average torques over an electrical cycle, τ_r is an array of allowable torque ripple values, θ is an array of positions at which the profile is defined, and k is the sorted index based on MTPA, with the highest MPTA current profile at $k = 1$. An example of the first 30 current profiles without voltage constraints is shown in Figure 3.8.

For non-zero torque ripple, particle swarm optimization (PSO) is used to generate a range of current profiles that meet a targeted torque and torque ripple value. Particles (current values) are defined at each position, and a weighting vector is applied with non-uniform velocity limits during particle velocity calculations according to the TPA at each position such that particles in areas of high TPA have increased mobility in the positive direction and particles in areas of low TPA have increased mobility in the negative direction. The fitness function minimizes the sum of the phase currents. One key advantage of this method is that an arbitrary torque waveform does not need to be assumed, such as in TSF approaches, as the PSO algorithm determines the optimal waveform based on machine characteristics.

These profiles are used by a function that sweeps winding configurations and uses the current fed model to determine the required voltage associated with each winding configuration (shown in Figure 3.9), current profile, and various speeds. Similar to the current-based torque ripple optimization method, PSO is used to minimize voltage peaks and the sum of the three phase currents. An example of swarm progression during voltage-constrained current profile optimization for various PSO iterations is shown in Figure 3.10. Particles in the swarm trend toward lower performance metrics of minimizing normalized maximum absolute voltage and normalized total current.

This function outputs a new list of current profiles that satisfy voltage constraints and are defined for various torque-speed combinations. This can be described as an array of voltage constrained current profiles for each winding configuration:

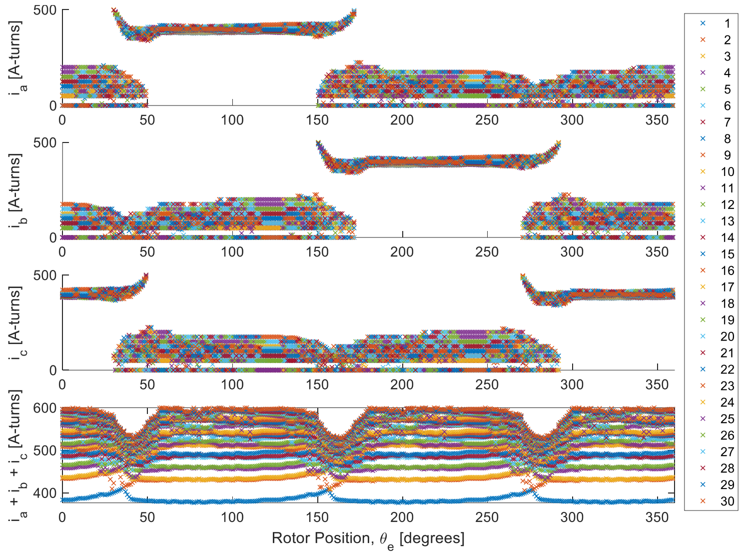

Figure 3.8 Exemplar current profiles generated by the optimizer without voltage constraints that generate a targeted torque and torque ripple. The first index represents the optimal profile without voltage constraints and other indices (2-30) are used as initial solutions as voltage constraints are implemented.

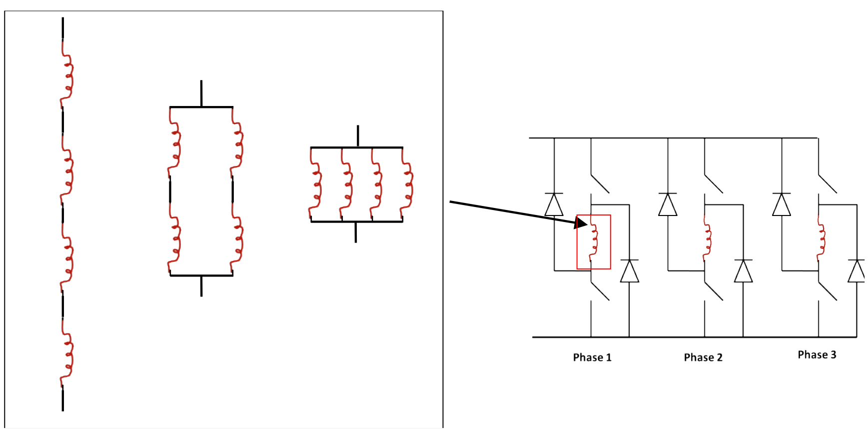

Figure 3.9 Winding configurations considered during optimization.

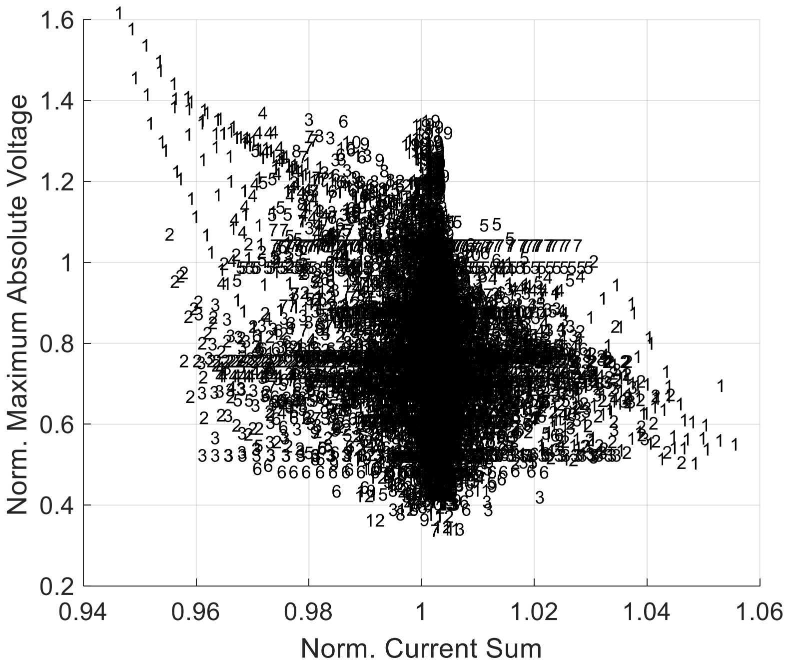

Figure 3.10 Exemplar swarm progression for various PSO iterations during voltage-constrained current profile optimization.

$$i\_v_{profile} = i(\tau_{avg}, \tau_r, \omega, k, \theta, N_t, N_{str}, N_{par}) \quad (3.33)$$

where additional dimensions are included for ω, the rotational speed of the rotor, N_t, the number of turns in each coil, N_{str}, the number of strands in each turn, and N_{par}, the number of parallel branches, which in this case is either 1, 2, or 4. An example of the voltage (per turn), flux linkage, and torque associated with a voltage-constrained current profile is shown in Figure 3.11.

In addition to generating voltage constrained current profiles across the torque-speed range for winding parameters, a maximum torque versus speed envelope is defined for each torque ripple value based on voltage and current constraints. Similar to the current profile arrays, an array of maximum torque envelopes can be described as

$$\tau_{env} = \tau(\tau_r, \omega, N_t, N_{str}, N_{par}) \quad (3.34)$$

The maximum torque envelope calculation is implemented during the generation of voltage constrained current profiles, in which the current profile with the highest MTPA is selected until voltage constraints are reached. Then, the current profile with the highest MTPA value that also meets voltage constraints is selected. If these conditions are not met for a given torque and allowable torque ripple target, there is no additional entry in the $i\_v_{profile}$ array in the τ_{avg} dimension, and the previous successful increment of τ_{avg} is stored in a torque envelope array, and the optimizer proceeds to the next speed. Torque envelopes and other operational data for each machine design variation are fed to the machine design optimizer.

Conclusions

A framework and method to perform systematic co-optimization of SRM design and control been proposed and demonstrated. Transient models rely on torque and flux-linkage lookup tables from 2D FEA to yield a decrease in computation time by a factor of at least 100 times in comparison with 2D transient FEA. This reduction in computational time greatly facilitates broad sweeps of both machine design and control parameters, and the implementation of this framework is detailed in Chapter 4.

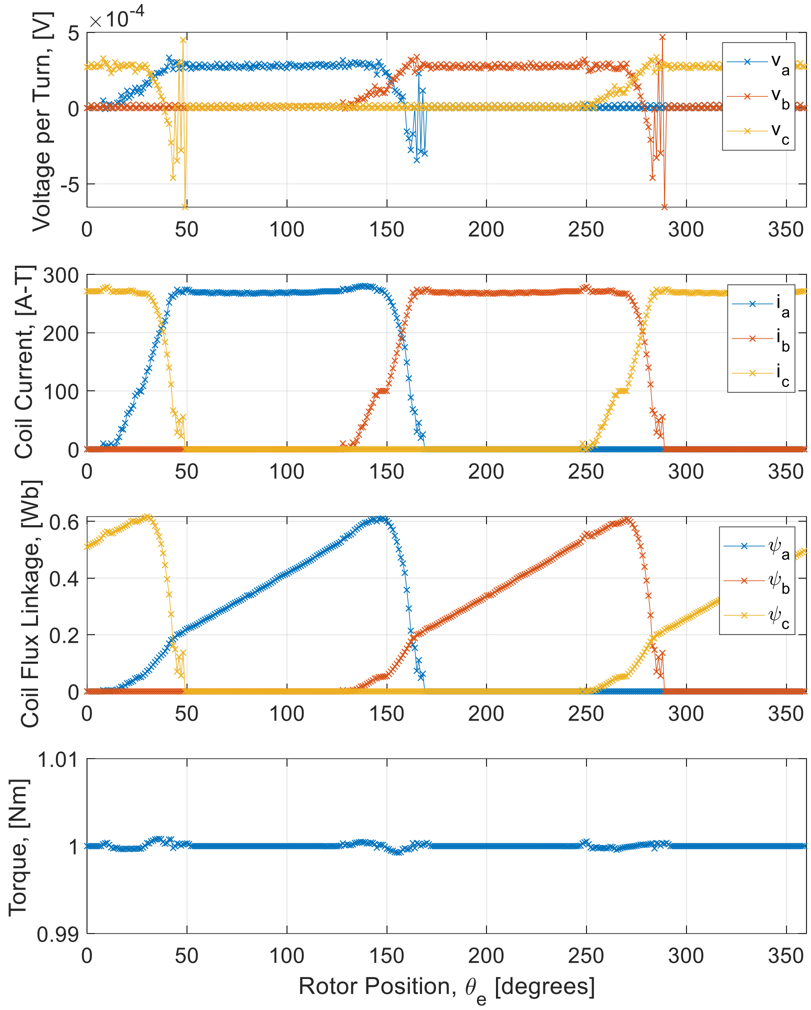

Figure 3.11 Example of voltage-constrained current profile shows that the optimizer generates smoother reference waveforms to remain within voltage limits.

References

[3.1] D. Lin, P. Zhou, W. N. Fu, Z. Badics and Z. J. Cendes, "A dynamic core loss model for soft ferromagnetic and power ferrite materials in transient finite element analysis," *in IEEE Transactions on Magnetics*, vol. 40, no. 2, pp. 1318-1321, March 2004, doi: 10.1109/TMAG.2004.825025.

CHAPTER FOUR: SWITCHED RELUCTANCE MACHINE DESIGN AND CONTROL OPTIMIZATION

Portions of this chapter were originally published by Timothy Burress and Dr. Leon Tolbert:

T. Burress, L. M. Tolbert, "Multiple Objective Co-Optimization and Experimental Evaluation of Switched Reluctance Machine Design and Controls," *IEEE International Electric Machine and Drives Conference*, San Francisco, California, May 15-18, 2023.

Abstract

A new modeling framework and optimization process for co-optimization of both switched reluctance machine (SRM) design and control across the entire torque-speed operation range was presented in Chapter 3. In this chapter, a baseline electric machine is selected to aid with the establishment of performance targets and nominal design specifications, optimization is implemented under zero and maximum speed conditions to perform design down-selection, and the proposed optimization framework is implemented to demonstrate multiple objective optimization of SRM design and control with consideration of several machine characteristics throughout the entire operation region. Portions of this chapter will be published in [4.3].

Overview

The optimization framework presented in Chapter 3 is implemented as SRM geometry, and control is optimized with multiple objectives. The Nissan LEAF primary traction drive electric machine is used as a baseline reference since detailed design, performance, and operational metrics are publicly available [4.1]. While the goal of this work is not to surpass the performance and efficiency of the baseline design, it serves as a good reference for application requirements such as maximum torque versus speed and continuous power capability. Further, other design metrics such as the stator outer diameter (OD), stator length, operation voltage, and current density are adopted for the nominal SRM design. The effectiveness of the proposed optimization framework is demonstrated as a wide range of design variables are considered, and impacts of various design constraints such as torque ripple are realized as performance across the entire torque-speed operation range is assessed.

Baseline Electric Machine

The 2012 Nissan LEAF primary traction drive electric machine was selected as a baseline reference since detailed design, performance, and operational metrics are publicly available [4.1]. It was also chosen because it is the sole source for propulsion power for an electric vehicle (EV) and therefore has a continuous operation capability that is more broadly applicable to other vehicle types and other applications. In contrast, electric machines in hybrid electric vehicles (HEV) share the burden of propulsion with combustion engines and as a result often have nonintuitive peak and continuous power capabilities that may not be as broadly applicable to other vehicle architectures and applications.

Key performance, geometric dimensions, and winding design metrics of the 2012 Nissan LEAF are shown in Table 4.1. The published rated torque and power of the LEAF electric machine is 280 Nm and 80 kW, respectively, with a maximum operation speed of 10,390 rpm. The phase current rating is 442 Arms, and with 4 parallel coils, the current rating for each coil is 110.5 Arms. Each slot has 8 turns of 15 strands of wire, yielding a total of 120 wires per slot. With a 20 AWG wire size, the total cross-sectional area of copper in the slot is 62.28 mm^2. Therefore, the current density using only copper cross-sectional area ("copper current density") is 14.2 Arms/mm^2, and current density using the entire slot area is about 9 Arms/mm^2. Typical current densities achieved in electric machines with various cooling methods are shown in Table 4.2 [4.2]. Current density is a key metric regarding the thermal loading of the machine, and typical values can be used as a reference for specifying a targeted current density without comprehensive consideration of the heat transfer characteristics of the system. The measured torque-speed efficiency map, shown in Figure 4.1, indicates a broad operation region above 90% efficiency. Empirical testing also indicates that the published rated power of 80 kW was achieved continuously at 7,000 rpm with the maximum stator temperature remaining below 150°C.

Fixed and Nominal SRM Design Parameters

Based on design and operational parameters of the LEAF electric machine, fixed parameters throughout the entire optimization process include a targeted rated power of 80 kW, rated torque of 280 Nm, maximum speed of 10,000 rpm, DC link voltage of 375 Vdc, an air gap of 0.5 mm, and a stator outer diameter of 200 mm. Nominal and potentially variable parameters include a rated phase current of 450 Arms, and a stack length of 151 mm. These fixed parameters and other nominal design parameters are summarized in Table 4.3. Similar to the LEAF, the cooling approach for the SRM was selected to be a liquid-cooled jacket with circumferential coolant paths for a water-ethylene glycol mixture that is typically used in EVs and HEVs. Therefore, a targeted

Table 4.1 2012 Nissan LEAF design and operational parameters.

Parameters	**Value**
Rated Power	80 kW
Rated Torque	280 Nm
Maximum Speed	10,390 rpm
Stator OD	200 mm
Stator Inner Diameter	131 mm
Rotor OD	130 mm
Stack Length	151 mm
Poles	8
Strands per coil	15
Turns per coil/slot	8
Wires per slot	120
Wire size	20 AWG
Wire Area in slot	62.28 mm^2
Current Rating	442 Arms
Current Rating Per Coil	110.5 Arms
Current Density (copper only)	14.2 $Arms/mm^2$
Current Density	~9 $Arms/mm^2$
Nominal DC link Voltage	375 Vdc

Table 4.2 Typical current densities in electric machines with various cooling methods.

Cooling Type	Current Density [A-RMS/mm^2]
Convection air cooling	2-4
Forced air cooling	4-8
Water stator jacket	6-14
In-slot direct cooling	10-25
Direct immersion and spray cooling	8-28

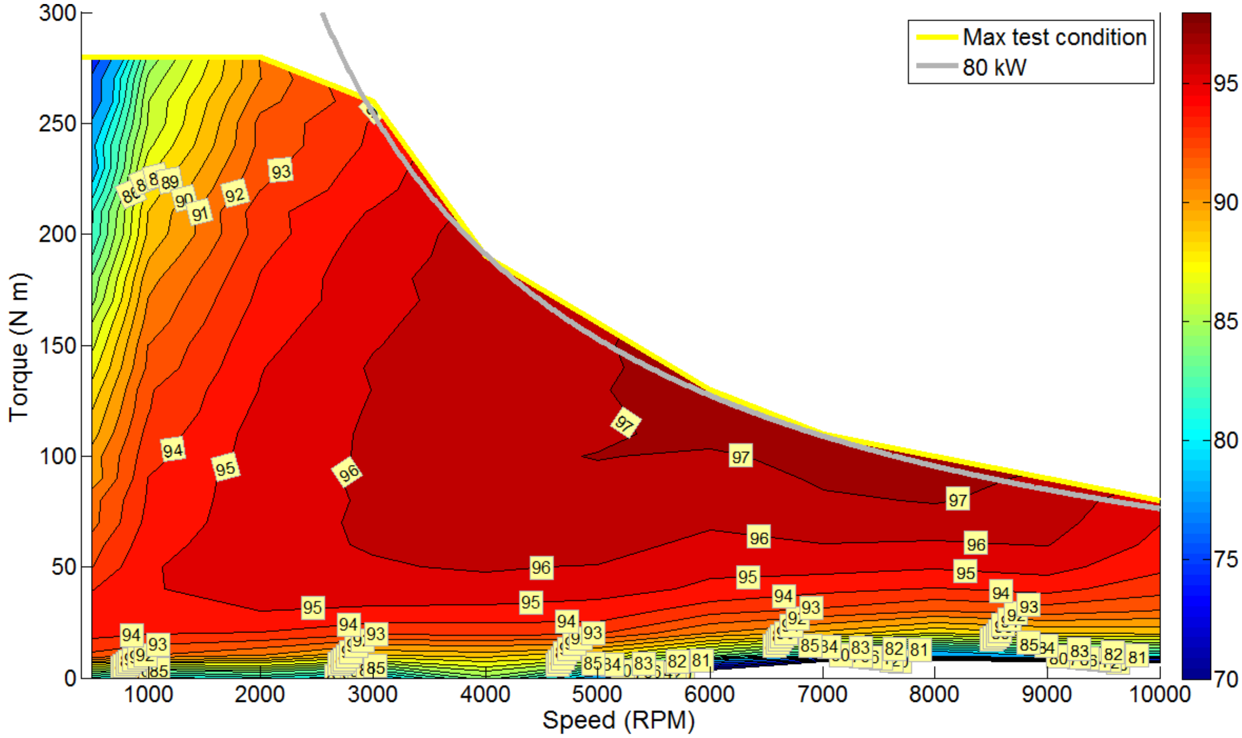

Figure 4.1 Measured Nissan LEAF electric machine performance curve and efficiency contour map.

Table 4.3 Nominal and fixed parameters for SRM optimization.

Parameter	**Value**
Rated Power (fixed)	80 kW
Rated Torque (fixed)	280 Nm
Maximum Speed (fixed)	10,000 rpm
Stator Outer Diameter (fixed)	200 mm
Air Gap (fixed)	0.5 mm
Number Stator Teeth (fixed)	12
Number or Rotor Teeth (fixed)	8
Stack Length (nominal)	151 mm
Phase Current Rating (nominal)	450 Arms
Copper Current Density (nominal)	15 Arms/mm^2
Current Density (nominal)	9 Arms/mm^2
DC link Voltage (fixed)	375 VDC

current density of 9 Arms per mm^2 was selected with the LEAF as a basis. This target is in the middle of the range of typical current density values (6-14 Arms per mm^2) found in water jacket-based cooling systems listed in Table 4.2.

Stage 1 SRM Design Studies and Zero-Speed Down-Selection with Static FEA

An SRM with 12 stator teeth and 8 rotor teeth, referred to as a 12/8 design, was selected since it is a 3-phase machine that can be driven by three switching devices and three diodes, similar but in a different arrangement to a conventional 3-phase drive. Further, the number of rotor teeth was selected as a compromise between the effective high torque ripple associated with smaller numbers of rotor teeth, and the high operational frequencies and losses associated with higher numbers of rotor teeth. The six geometric parameters identified for the first step of optimization are shown in Figure 4.2. The stator OD is fixed at 200 mm, while the stator ID varies based on the rotor OD and a fixed air gap of 0.5 mm. Stator yoke thickness and stator ID determines the depth of stator slots. Rotor tooth length determines the length of the rotor tooth between the OD of the rotor back-iron and rotor OD. Widths of stator and rotor teeth are determined by the stator and rotor tooth width factors according to:

$$w_{ST} = D_{SI} \frac{\pi}{N_S} \frac{1}{2} k_{STW} \tag{4.1}$$

$$w_{RT} = D_{RO} \frac{\pi}{N_S} \frac{1}{2} k_{RTW} \tag{4.2}$$

where w_{ST} is the stator tooth width, D_{SI} is the stator ID, N_S is the number of stator teeth, k_{STW} is the stator tooth width factor, w_{RT} is the rotor tooth width, D_{RO} is the rotor outer diameter, and k_{RTW} is the rotor tooth width factor.

The first down-selection is implemented by performing static FEA at zero-speed to determine torque and other performance metrics as parameterized geometries are varied. Since it is important to consider the impact of geometry changes on winding cross-sectional area and the corresponding current density, the FEA model is setup to calculate the cross-sectional area of the winding for each geometry and output it for post-processing. The values shown in Table 4.4 indicate the range of each parameter in the solution space prior to the first down-selection. As discussed in more

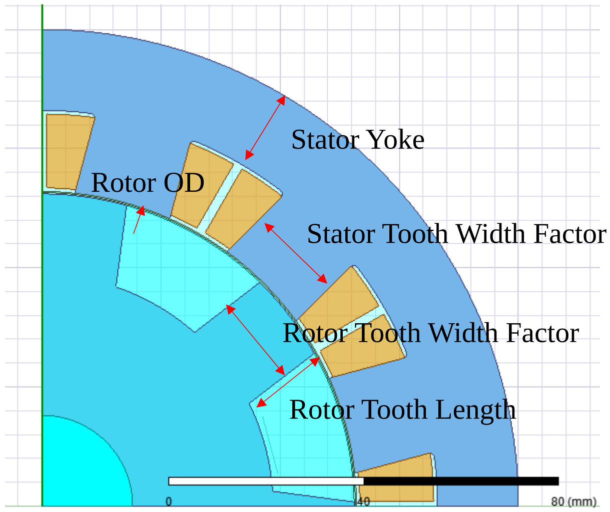

Figure 4.2 Geometric parameters selected for initial optimization.

Table 4.4 Range of geometric parameters in solution space prior to first down-selection.

Parameter	**Value**
Rotor OD	110-130 mm
Stator Yoke	7-19 mm
Stator Tooth Width Factor	0.9-1.2
Rotor Tooth Width Factor	0.8-1.2
Rotor Tooth Length	10-30 mm

detail later, these ranges are a result of iterations on a smaller initial solution space made to ensure maximum performance conditions were reached within the solution space prior to the first down-selection.

All simulations in the first stage involve the application of a constant single-phase current as the rotor is incremented between zero to 180 electrical degrees and the corresponding locked rotor torque is calculated. Exemplar results for current levels of 2,000 ampere-turns (A-T) and 5,000 A-T are shown in Figures 4.3 and 4.4, respectively. Single phase torque profiles are shown for all three phases and the summation of these curves yields the 3-phase torque calculated from a single-phase torque profile. This is in close agreement with actual 3-phase simulations for both excitation levels, indicating that the principle of superposition applies even for cases with high magnetic non-linearity. Therefore, a significant reduction in the number of simulation cases can be achieved by applying this principle to approximate three-phase torque.

While winding configuration details such as the number of turns and number of strands in parallel for each conductor have an impact on winding impedance and therefore transient operation, performance under zero-speed static conditions can be fully assessed without detailed winding information specified. For example, the 5,000 A-T condition equally represents multiple winding configurations such as 100 A with 50 turns or 50 A with 100 turns. This approach is implemented in various stages of the overall optimization framework, as it greatly reduces the amount of FEA cases required for design and control optimization since electromagnetic characteristics of the machine can be obtained in FEA without specifying detailed winding characteristics, and the winding can be optimized by post-processing static FEA results.

The graphs in Figure 4.5 show the average torque and ratio of average torque to current density ratio ("TCD ratio") evaluated at current levels of 2,000 A-T and 5,000A-T for the range of geometric parameters described in Table 4.4. Average torque represents the total three-phase torque computed using the superposition principle with single-phase FEA results. The TCD ratio is an effective way to gauge torque performance while also considering implications of heat generated in the winding. Geometries with higher torque tend to have lower TCD ratios, and

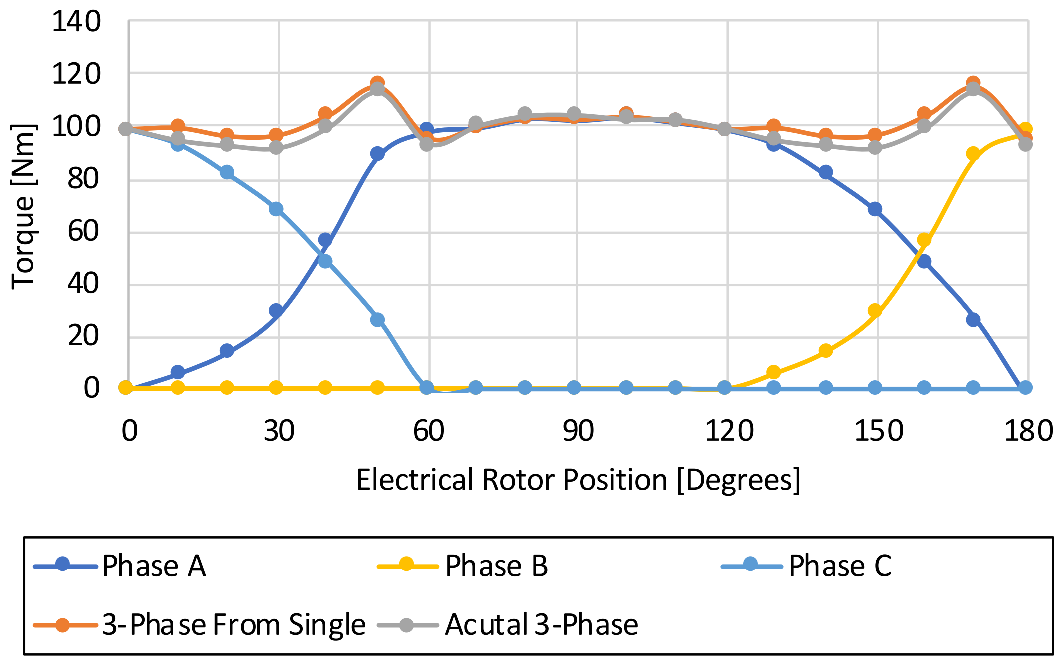

Figure 4.3 Single phase, calculated three-phase, and actual three-phase locked rotor torque profiles for 2,000 amp-turns indicate that the 3-phase torque profile can be calculated using only the single phase torque profile.

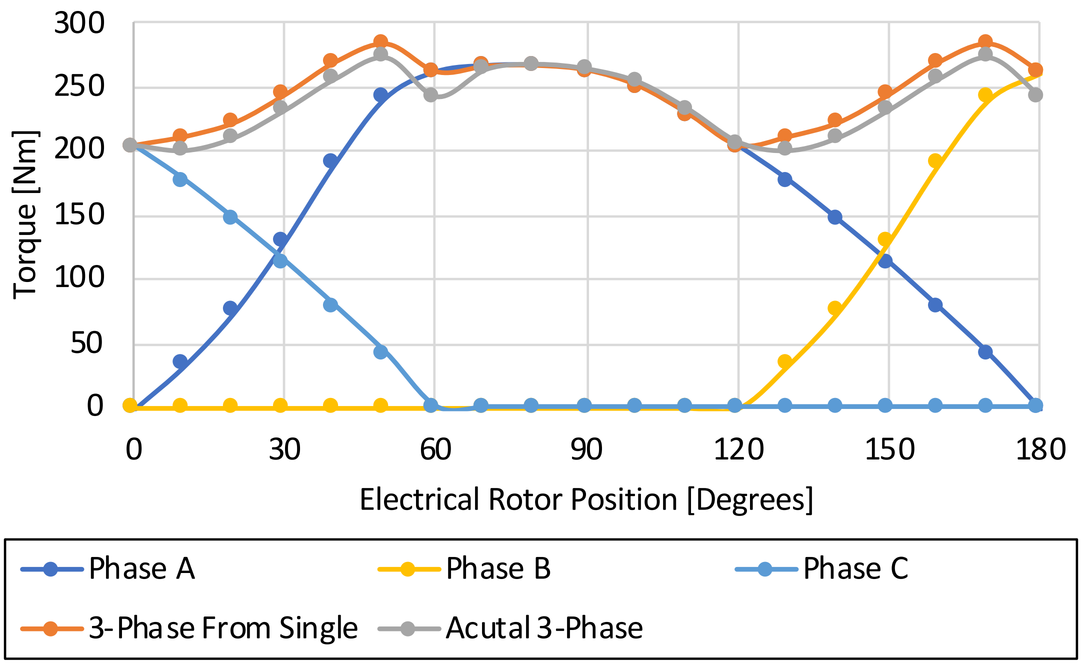

Figure 4.4 Single phase, calculated three-phase, and actual three-phase locked rotor torque profiles for 5,000 amp-turns indicate that the 3-phase torque profile can be calculated using only the single phase torque profile.

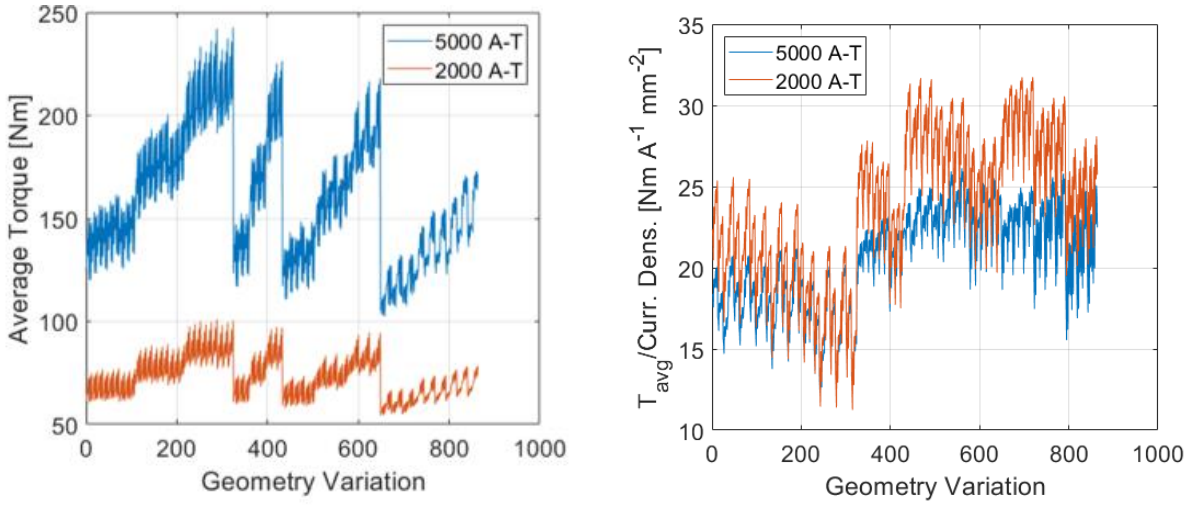

(a) (b)

Figure 4.5 (a) Average torque and (b) ratio of average torque to current density resulting from static FEA for 863 geometry variations.

geometries with high TCD ratios tend to have lower torque. Current density and coil cross-sectional area are plotted in a similar manner in Figure 4.6. Geometries with high torque correspond with small coil areas and therefore also correspond with higher current densities, while geometries with high TCD ratios tend to have large coil areas and lower current density.

Average torque is plotted versus rotor OD and stator yoke thickness for current levels of 2,000 A-T and 5,000 A-T in Figures 4.7 and 4.8, respectively. These scatter plots show the considerable impact of rotor OD and stator yoke thickness on average torque and include points for all combinations of geometries.

Similar plots are shown in Figures 4.9 and 4.10, but with TCD ratios plotted versus stator tooth width factor and stator yoke thickness. A comparison of the average torque and TCD ratio plots provides more insight into the tradeoffs between average torque and TCD ratio. These plots were generated for all geometric parameters after each manual iteration of the solution space to determine if and how the solution space should be expanded.

The sensitivity of torque and TCD ratio to variations in each geometric parameter across the ranges listed in Table 4.4 is shown in the bar plots in Figures 4.11 and 4.12, respectively. As shown by the exemplar green features in Figure 4.10(b), peak profiles for maximum torque and TCD ratio were determined by obtaining the maximum value across all discrete values of each geometric parameter, then sensitivity was determined by the difference between maximum and minimum values along this peak profile. Stator yoke thickness has the most significant impact on both torque and TCD ratio for both excitation levels of 2,000 A-T and 5,000 A-T. Rotor OD is the second most influential parameter on torque for both excitation levels and on TCD ratio at the 2,000 A-T excitation level, but the least influential parameter on TCD ratio at 5,000 A-T. Stator tooth width factor and rotor tooth width factor have similar influence on both performance metrics, and rotor tooth length generally has the least overall impact. The significant differences between sensitives at different excitation levels is a result of magnetic non-linearity and is discussed in more detail later.

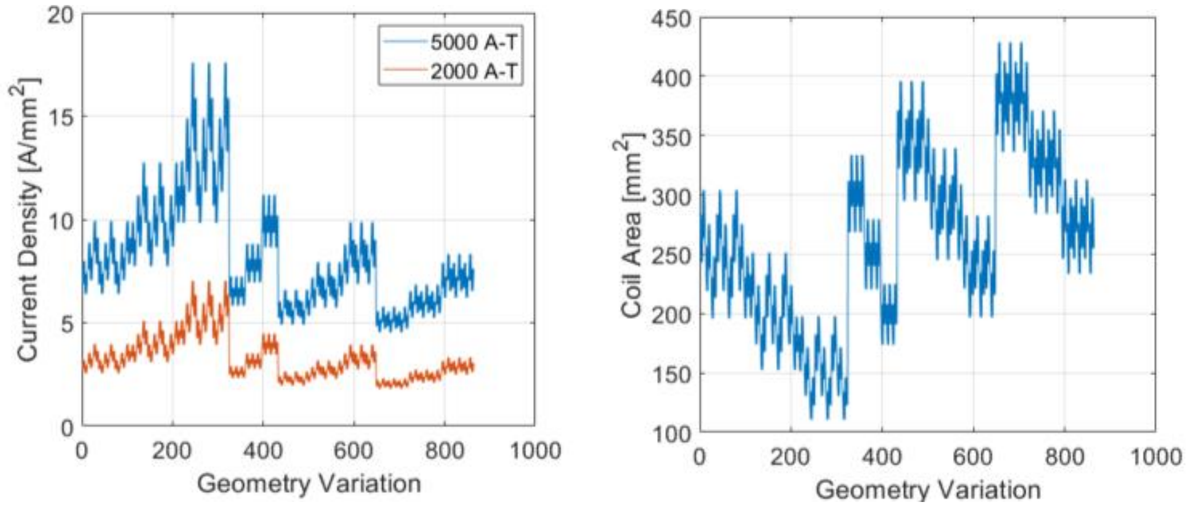

(a) (b)

Figure 4.6 (a) Current density and (b) cross-sectional coil area resulting from static FEA for 863 geometry variations shows the correlation between current density and coil area.

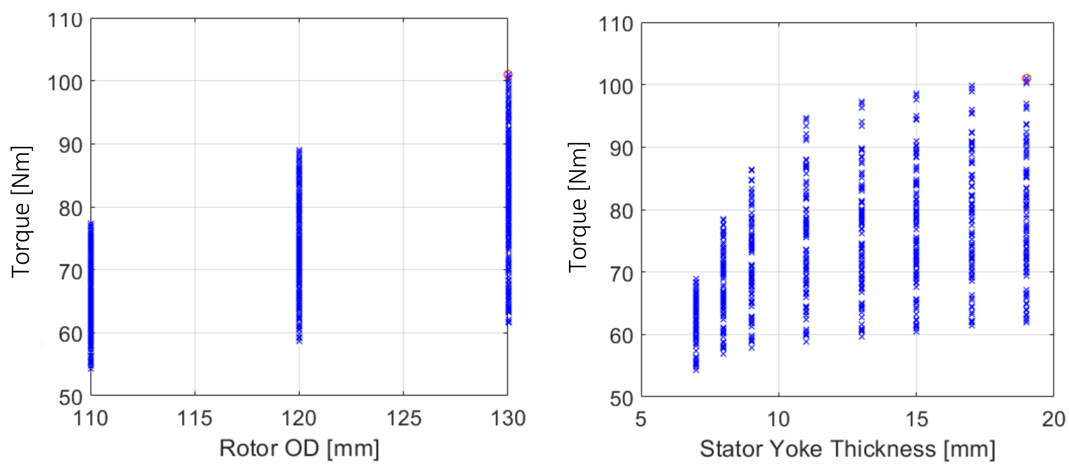

(a) (b)

Figure 4.7 (a) Average torque for 2,000 A-T versus rotor OD and (b) stator yoke thickness resulting from static FEA for 863 geometry variations.

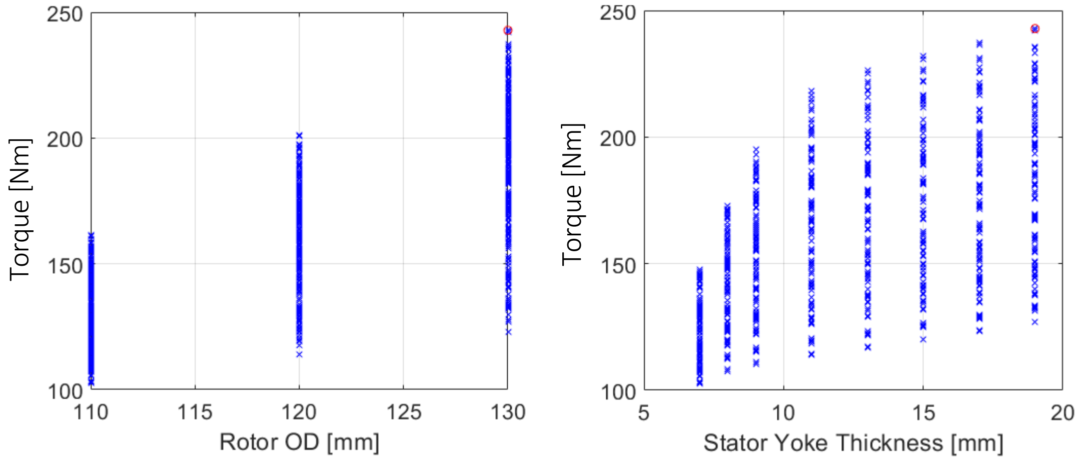

(a) (b)

Figure 4.8 Average torque for 5,000 A-T versus rotor OD (a) and stator yoke thickness (b) resulting from static FEA for 863 geometry variations.

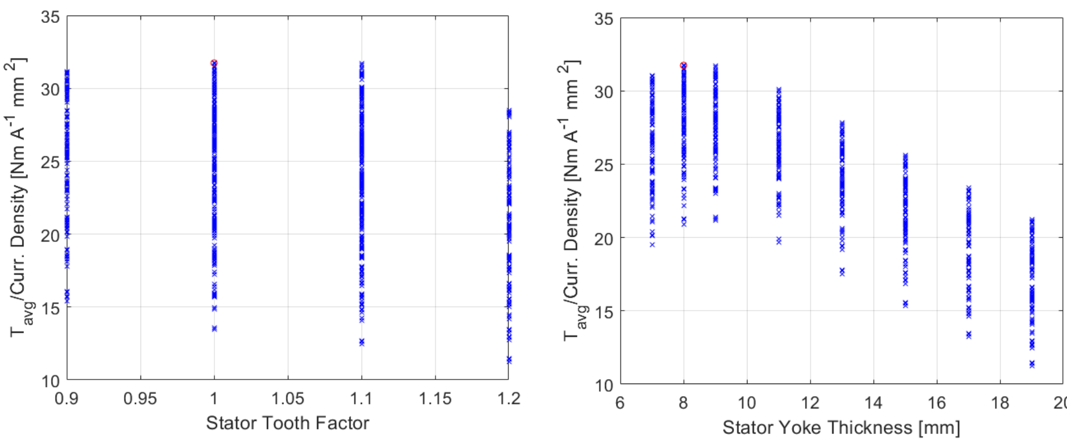

(a) (b)

Figure 4.9 (a) Ratio of average torque to current density for 2,000 A-T versus stator tooth width factor and (b) stator yoke thickness resulting from static FEA for 863 geometry variations.

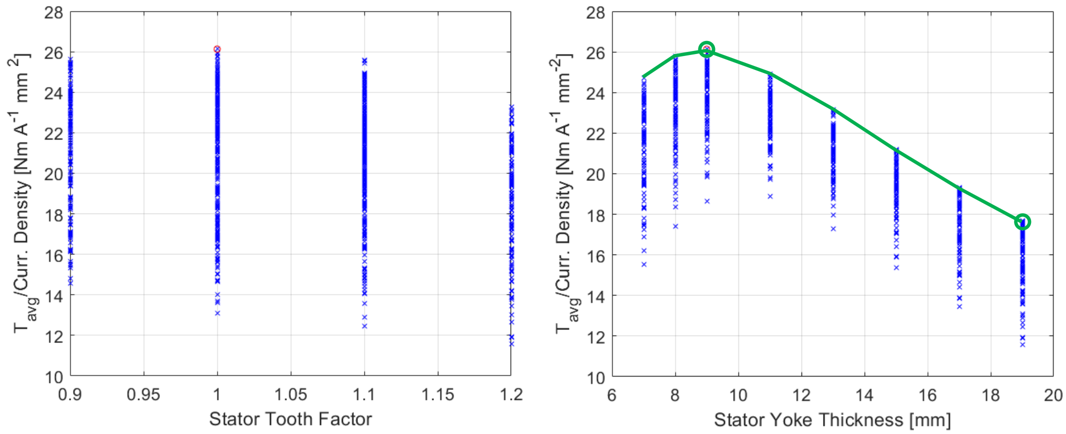

(a) (b)

Figure 4.10 (a) Ratio of average torque to current density for 5,000 A-T versus stator tooth width factor and (b) stator yoke thickness resulting from static FEA for 863 geometry variations.

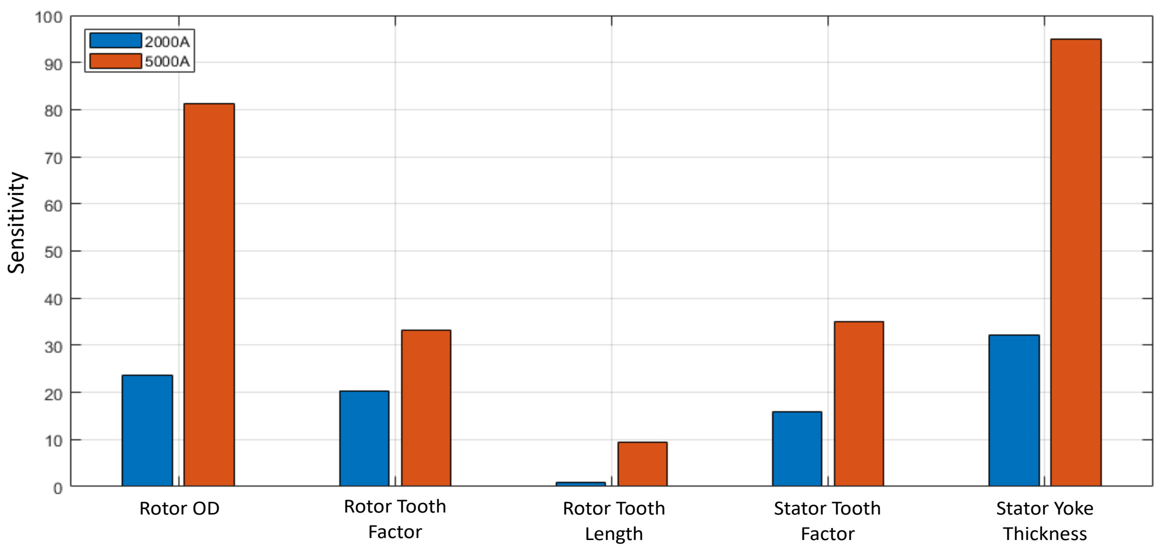

Figure 4.11 Bar chart showing sensitivity of torque to various geometric parameters.

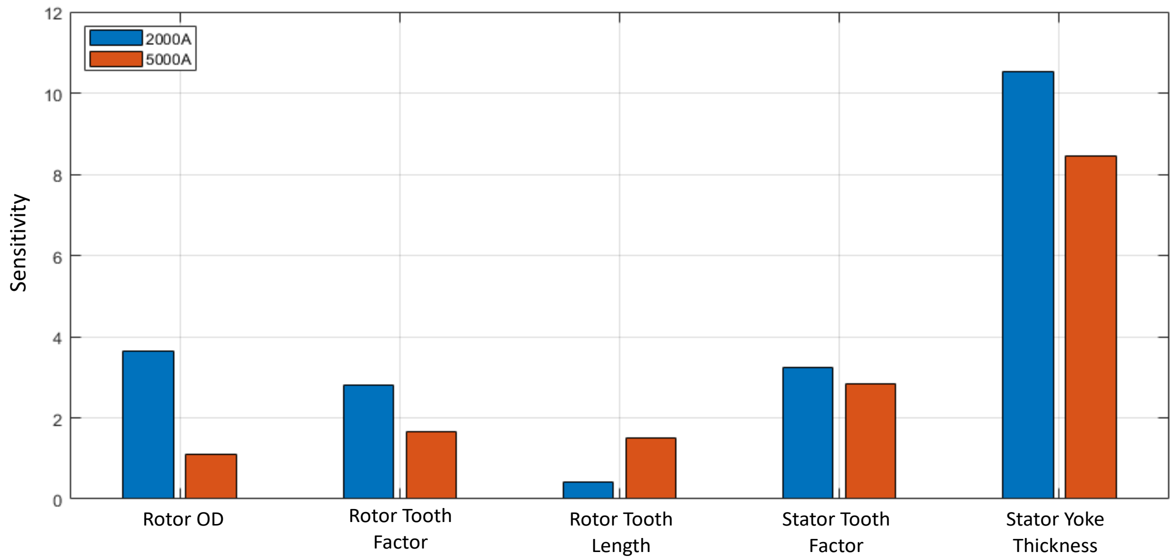

Figure 4.12 Bar chart showing sensitivity of TCD ratio to various geometric parameters.

Since average torque and TCD ratio are the two main performance metrics being observed during the zero-speed static analysis, scatter plots were generated with color mappings of geometric parameters and other design metrics. Scatter plots with color mappings of rotor OD and stator yoke thickness are shown for 2,000 A-T and 5,000 A-T in Figures 4.13 and 4.14, respectively. These plots offer a good visual indicator of the trade-off between torque and TCD ratio and how design variables and metrics correlate with them. They also indicate why having a single performance goal of maximum torque or maximum TCD ratio is not likely the best approach for design optimization. For example, the case with a maximum TCD ratio is associated with a much lower torque for a given current than the case with maximum torque. The case with maximum torque correlates with a low TCD ratio. A compromise between these two performance metrics is likely the best solution for most applications, and application requirements will likely determine which is most important. These performance trade-offs are largely associated with the cross-sectional area of the winding versus cross-sectional area of the stator and rotor magnetic circuit, where increased winding area reduces heat generated for a given current and increased stator and rotor sizes yield higher magnetic saliency and therefore higher torque for a given current.

The trade-off between winding area and stator thicknesses is indicated on the scatter plots of TCD ratio versus torque in Figures 4.15 and 4.16 for excitation levels of 2,000 A-T and 5,000 A-T, respectively. The average torque values and TCD ratios for all designs were normalized, and a performance function was used to determine the value of each design. The red trace indicates the threshold for down-selection and after iterative expansion of the solution space, down-selected geometries were identified and are indicated with red circles. Leading candidates for both excitation levels of 2,000 A-T and 5,000 A-T are numbered according to their index and corresponding geometric parameters and performance metrics are summarized in Tables 4.5 and 4.6, respectively. While detailed requirements of an application will drive design decisions, the approach used in this work is to identify designs with intermediate values of torque and TCD ratio such as geometry indices 647 and 648 for high excitation levels as indicated in Figure 4.16. Geometries associated with maximum TCD ratio are shown in Figure 4.17, and geometries producing maximum torque are shown in Figure 4.18. Steel in the stator and rotor is operating near saturation for high excitation levels, and therefore the relative torque-current ratio is lower,

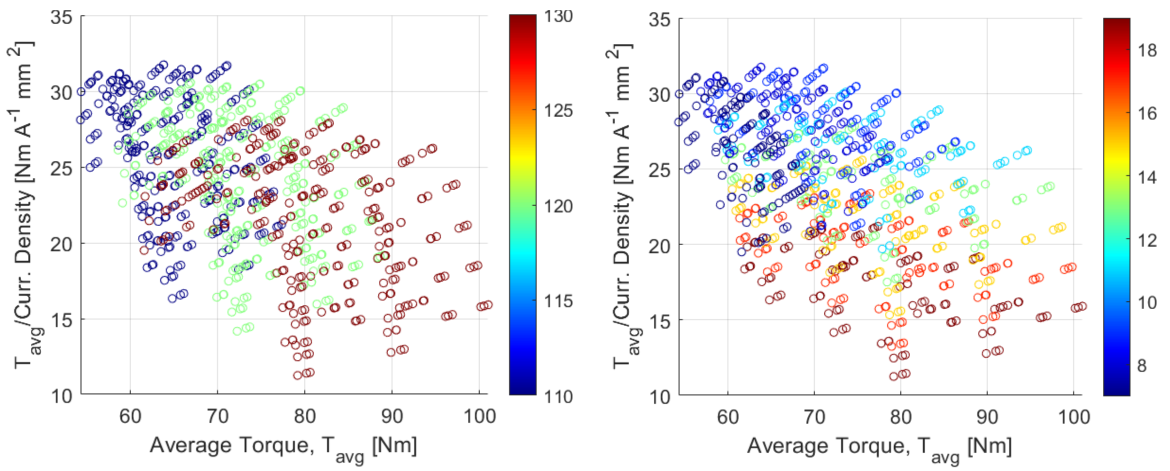

(a) (b)

Figure 4.13 (a) Scatter plot of torque-current density ratio versus average torque for 2,000 A-T with colormap of rotor OD [mm] and (b) stator yoke thickness [mm] resulting from static FEA for 863 geometry variations.

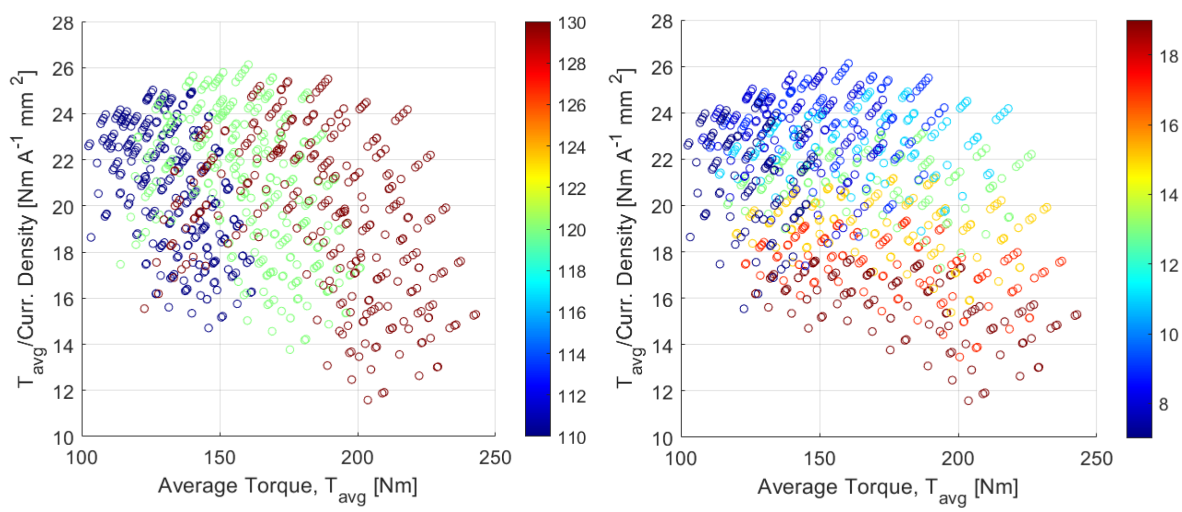

(a) (b)

Figure 4.14 (a) Scatter plot of torque-current density ratio versus average torque for 5,000 A-T with colormap of rotor OD and (b) stator yoke thickness resulting from static FEA for 863 geometry variations.

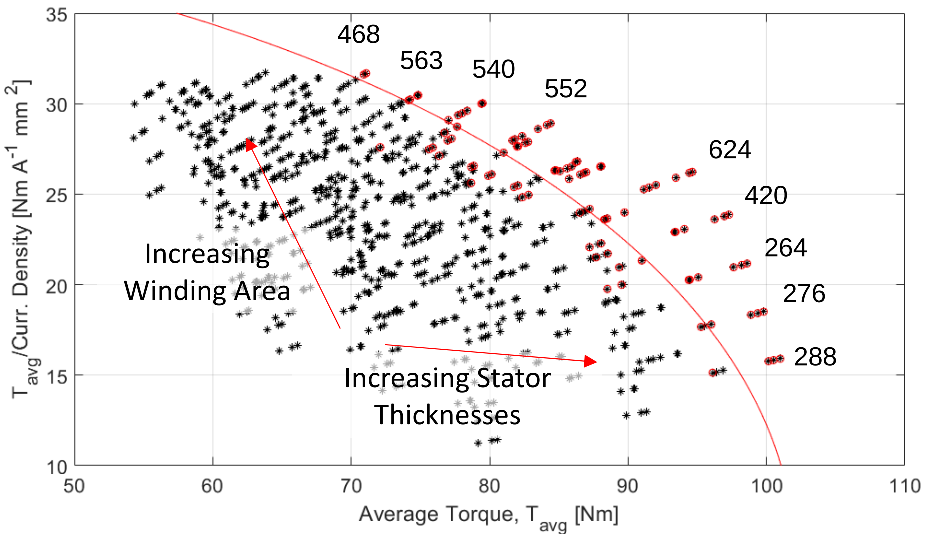

Figure 4.15 Scatter plot of torque-current density ratio versus average torque for 2,000 A-T with leading geometries numbered and down-selected geometries identified with red circles.

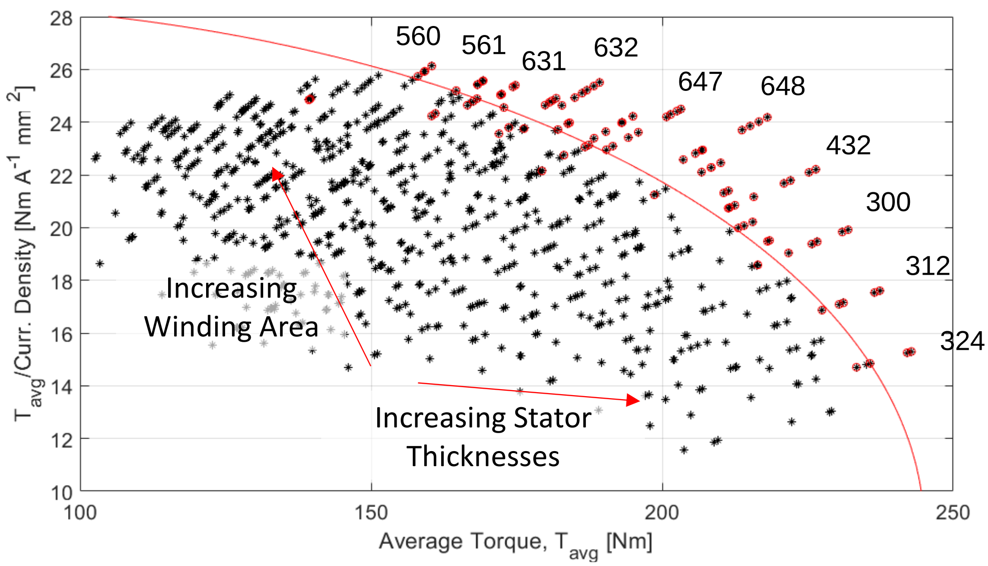

Figure 4.16 Scatter plot of torque-current density ratio versus average torque for 5,000 A-T with leading geometries numbered and down-selected geometries identified with red circles.

Table 4.5 Leading candidates and associated geometric parameters for 2,000 A-T.

Geom. Index, kG	Rotor Tooth Width Factor	Stator Tooth Width Factor	Rotor OD [mm]	Rotor Tooth Length [mm]	Stator Yoke Thick. [mm]	Average Torque, T_{avg} [Nm]	Average Torque-Current Density Ratio
468	1.1	1.1	110	15	9	71.1	31.7
563	1.1	1	120	20	9	74.8	30.5
540	1.1	1.1	120	15	9	79.5	30.0
552	1.1	1.1	120	15	11	84.4	28.9
624	1.1	1.1	130	15	11	94.6	26.2
420	1.1	1.1	130	15	13	97.3	23.9
264	1.1	1.1	130	15	15	98.6	21.2
276	1.1	1.1	130	15	17	99.8	18.5
288	1.1	1.1	130	15	19	101.0	15.9

Table 4.6 Leading candidates and associated geometric parameters for 5,000 A-T.

Geom. Index, kG	Rotor Tooth Width Factor	Stator Tooth Width Factor	Rotor OD [mm]	Rotor Tooth Length [mm]	Stator Yoke Thick. [mm]	Average Torque, T_{avg} [Nm]	Average Torque-Current Density Ratio
560	1	1	120	20	9	160.2	26.1
632	1	1	130	20	9	188.4	25.6
647	1.1	1	130	20	11	203.7	24.6
648	1.1	1.1	130	20	11	218.3	24.4
432	1.1	1.1	130	20	13	225.1	22.4
300	1.1	1.1	130	20	15	231.2	20.1
312	1.1	1.1	130	20	17	237.6	17.7
324	1.1	1.1	130	20	19	242.4	15.3

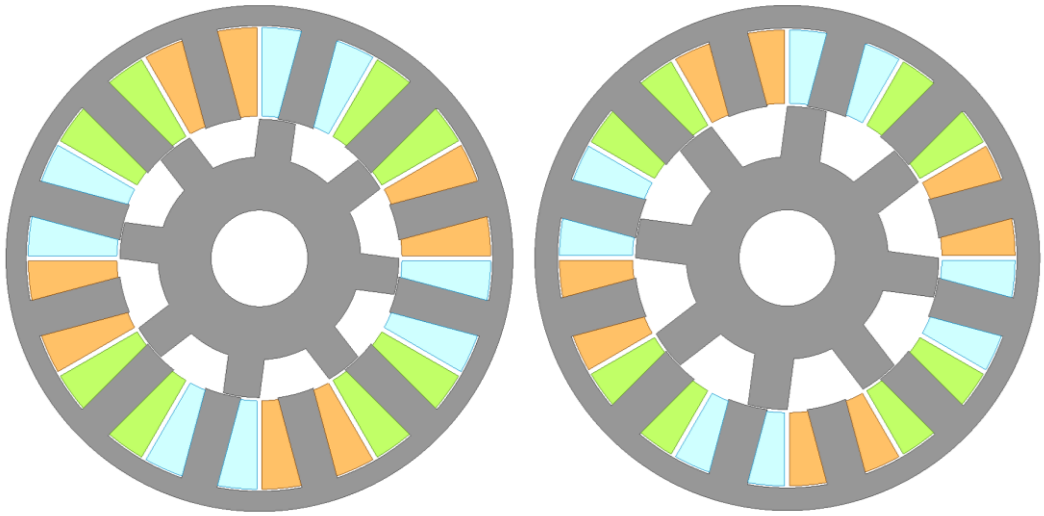

(a) (b)

Figure 4.17 Geometries associated with maximum torque-current density ratio for (a) 2,000 A-T and (b) 5,000 A-T.

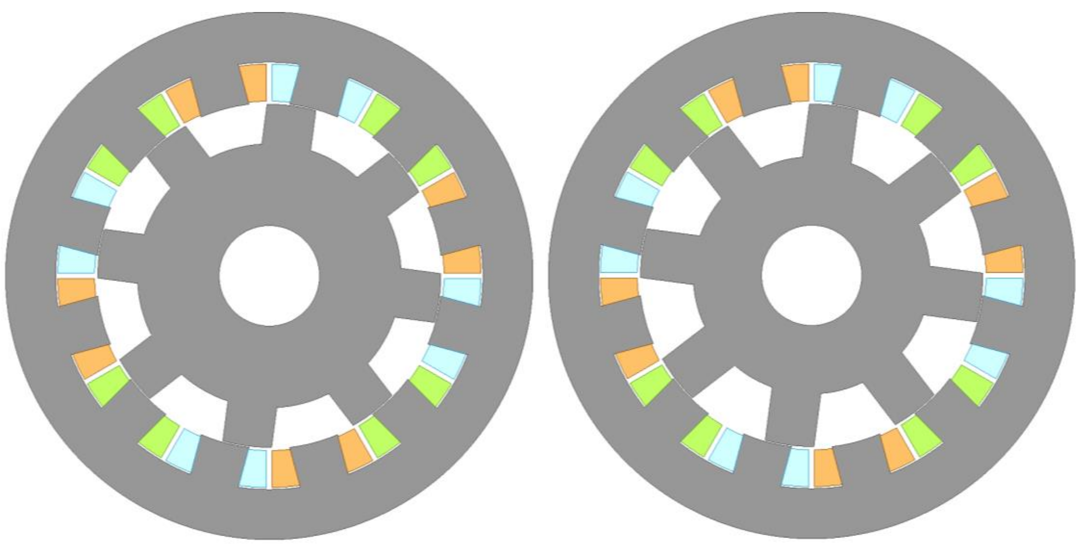

(a) (b)

Figure 4.18 Geometries associated with maximum torque for (a) 2,000 A-T and (b) 5,000 A-T.

particularly in geometries with reduced steel thickness. This generally results in lower TCD ratios for high excitation levels.

If a target is set of 9 Arms/mm^2 for the nominal current density for the intermediate torque of 200 Nm, the corresponding TCD ratio is ~22 Nm A^{-1} mm^2, and this is achieved with the nominal stack length. If the nominal current density of 9 Arms/mm^2 is targeted for the rated torque of 280 Nm, the associated TCD ratio should be about 31 Nm A^{-1} mm^2, and the scatter plot in Figure 4.19 shows that the previously identified leading candidates meet this condition if the stack length is scaled by 1.3 to 196.3 mm.

The down-selection resulted in 98 geometries that were studied for further insight into metrics that will help with design decisions and also to identify other parameters that might be useful in successive steps of the optimization process. This includes calculation of forces and mechanical stiffness for incorporation of acoustic noise modeling and a correlation study of flux density and core loss for core loss estimation during transient optimization.

Stage 1 Electromagnetic Force and Mechanical Deformation Correlation Studies with Down-Selected Geometries

Electromagnetic forces were calculated at both excitation levels for the down-selected geometries, and an example of edge force vectors on a stator tooth is provided in Figure 4.20. An example of the net radial and tangential forces on a stator tooth through one single-phase stroke is provided in Figure 4.21. The net radial force is a radial inward force on the stator tooth, and the net tangential force is directly associated with torque production. The maximum net radial and tangential force over the 180-degree torque production stroke is color mapped on a plot of TCD ratio versus average torque in Figure 4.22. It can be seen that the maximum radial forces are generally considerably higher than the tangential forces. These forces cause the tooth and stator back-iron to deform, and the amount of deformation depends on the stiffness of the stator, which varies with each geometry. Further, higher amounts of deflection correlate with higher levels of acoustic noise, which is one of the main negative characteristics of the switched reluctance motor.

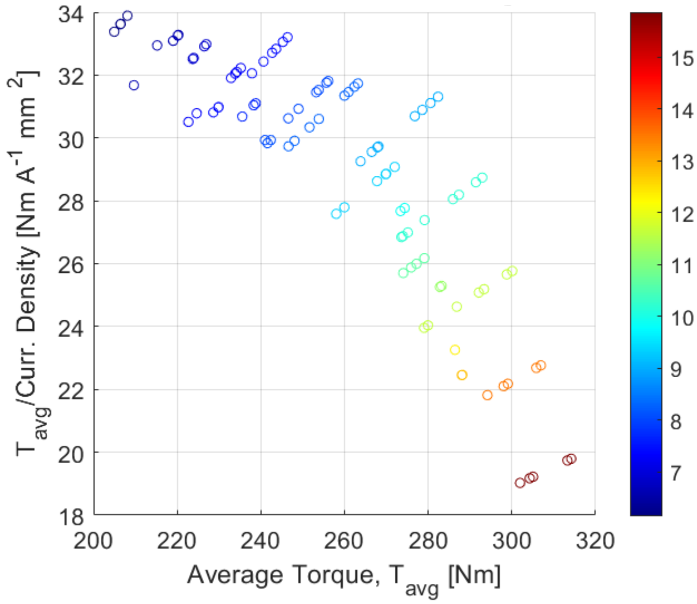

Figure 4.19 Scatter plot of torque-current density ratio versus average torque for 5,000 A-T with color map of current density after scaling stack length by a factor of 1.3.

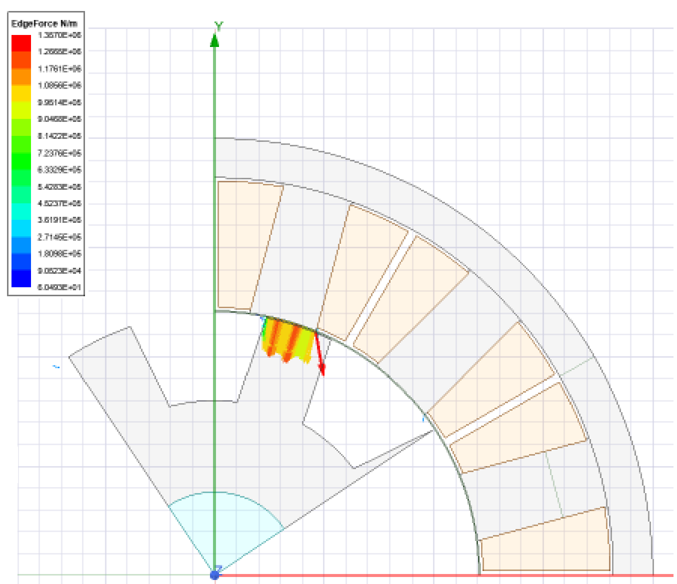

Figure 4.20 Example of edge force vectors resulting from FEA simulations.

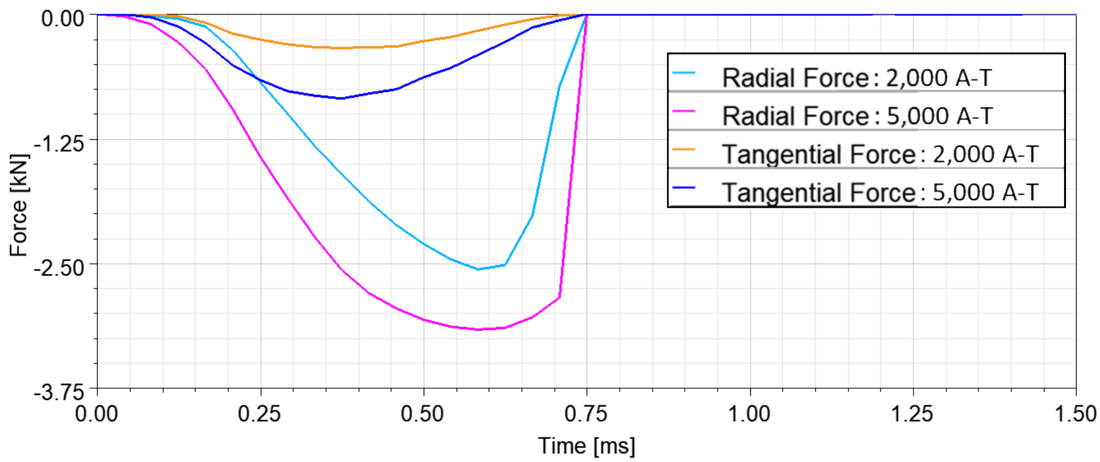

Figure 4.21 Example of average radial and tangential tooth forces for 2,000 and 5,000 A-T from transient FEA.

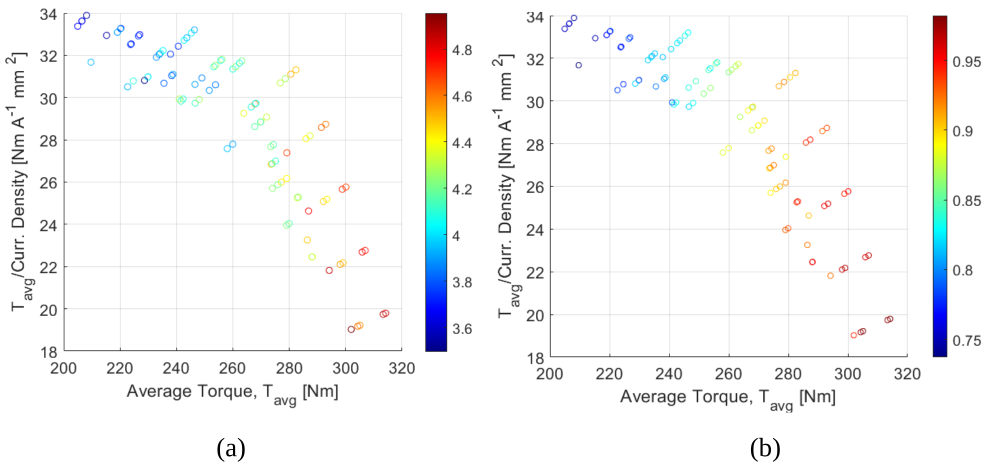

Figure 4.22 (a) Scatter plot of torque-current density ratio versus average torque for 5,000 A-T with color map of maximum radial force [kN] and (b) maximum tangential force [kN] over the 180-degree torque production region of a single phase.

The stress-strain curve of M270-35A electrical steel, a commonly used grade for SR motors, is shown in Figure 4.23. A parameterized mechanical model was developed to calculate structural deformation associated with radial and tangential loading, as shown in Figures 4.24 and 4.25, respectively. Exemplar radial and tangential deformation results for the thinnest stator geometry are shown in Figure 4.26, as the resulting deformation is plotted versus applied load. Even for the thinnest stator geometry, the maximum induced principal stress in the steel is below 35 MPa, which is well within the linear elastic region of the material, and therefore simulation of only one loading point is required for each geometry to determine the stiffness of the framework. This is particularly useful for simulations involving various loading conditions such as in the implementation of an acoustic noise model.

Radial and tangential stiffness values for each geometry are color mapped in the scatter plot of TCD ratio versus torque in Figure 4.27. This plot shows that geometries with high TCD ratios have considerably lower values of mechanical stiffness due to the thinner structural members of the stator. The color maps in Figure 4.28 show the radial and tangential deformation associated with an excitation level of 5,000 A-T. Interestingly, radial and tangential deformation is nearly the same for each case although radial loading values are much higher. This is a result of the radial stiffness generally being much higher than the tangential stiffness for all geometries.

Stage 2 and 3 Simulations and Down-Selections

Stage 2 simulations rely on the voltage fed model to determine operational metrics at maximum speed, and the waveforms shown in Figures 4.29 and 4.30 provide a comparison of transient FEA and the proposed code-based voltage fed model, respectively, at maximum speed near maximum power using the same control conditions. While winding resistance loss calculations are straightforward, core losses were approximated by developing expressions for stator back-iron, stator tooth, rotor back-iron, and rotor tooth flux density as a function of flux-linkage, and the time domain core loss equations described in Chapter 3 were implemented. Comparing results of FEA and the voltage fed model, the average torque is 158 Nm and 160 Nm, the torque ripple is 49.3% and 48.9%, and the efficiency is 76.0 and 74.2%, respectively.

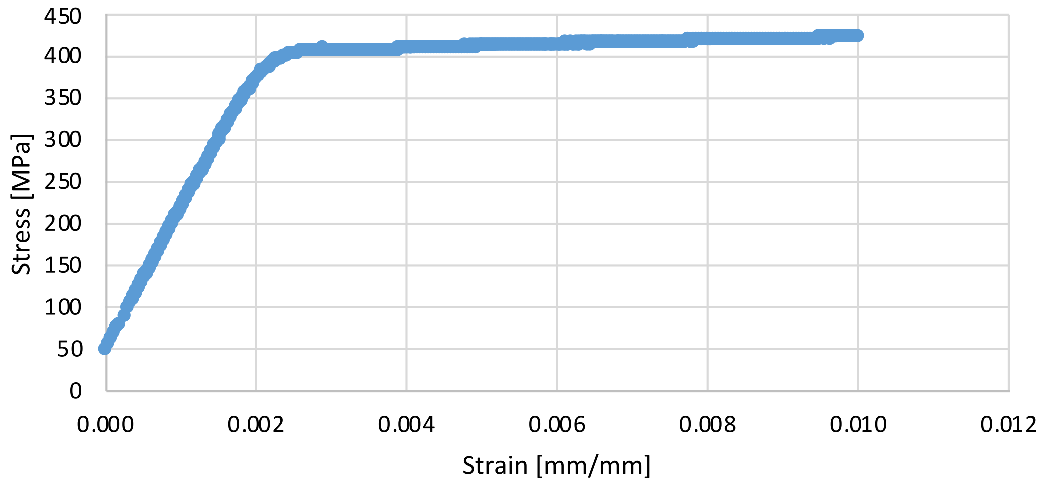

Figure 4.23 Stress-strain curve for M270-35A electrical steel.

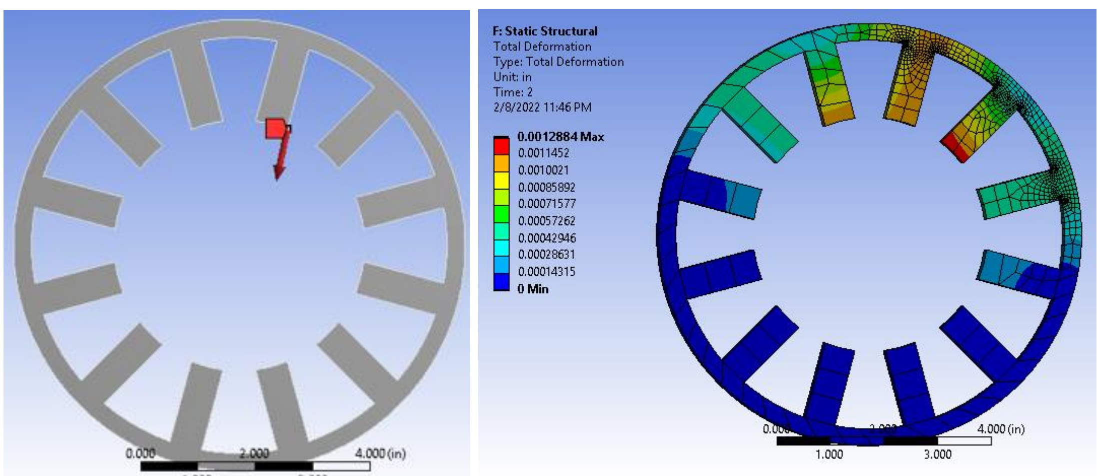

(a) (b)

Figure 4.24 Example of (a) radial loading vector and (b) corresponding deformation colormap calculated using static mechanical FEA.

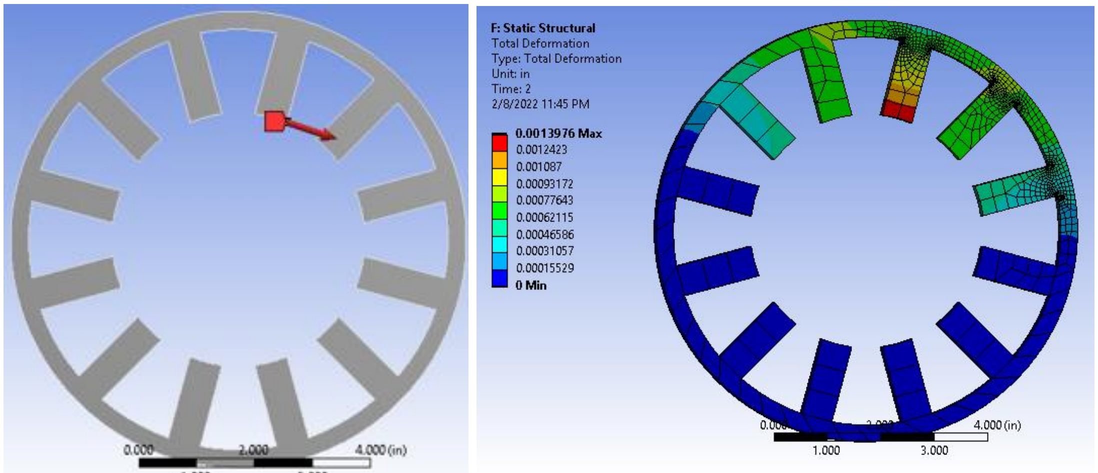

(a) (b)

Figure 4.25 Example of (a) tangential loading vector and (b) corresponding deformation colormap calculated using static mechanical FEA.

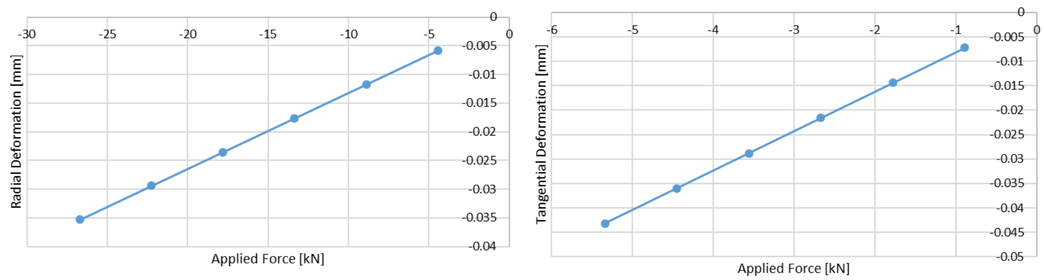

(a) (b)

Figure 4.26 Example of (a) radial deformation versus applied radial force and (b) tangential deformation versus applied tangential force calculated using static mechanical FEA.

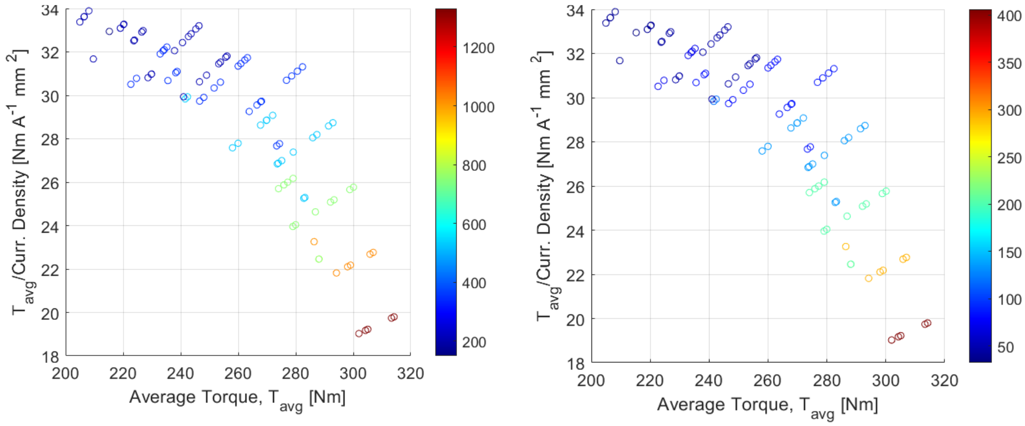

(a) (b)

Figure 4.27 (a) Scatter plot of torque-current density ratio versus average torque for 5,000 A-T with color map of radial stiffness [kN/mm] and (b) tangential stiffness [kN/mm] shows that the geometries with higher TCD ratios are associated with considerably lower levels of mechanical stiffness.

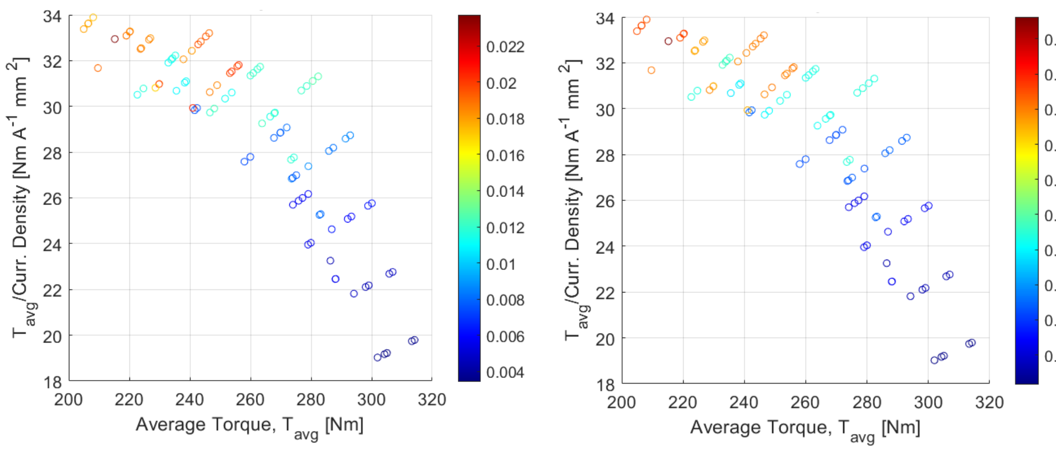

(a) (b)

Figure 4.28 (a) Scatter plot of torque-current density ratio versus average torque for 5,000 A-T with color map of radial deformation [mm] and (b) tangential deformation [mm] shows that the geometries with higher TCD ratios are associated with considerably higher deformations, which correlate with higher acoustic noise levels.

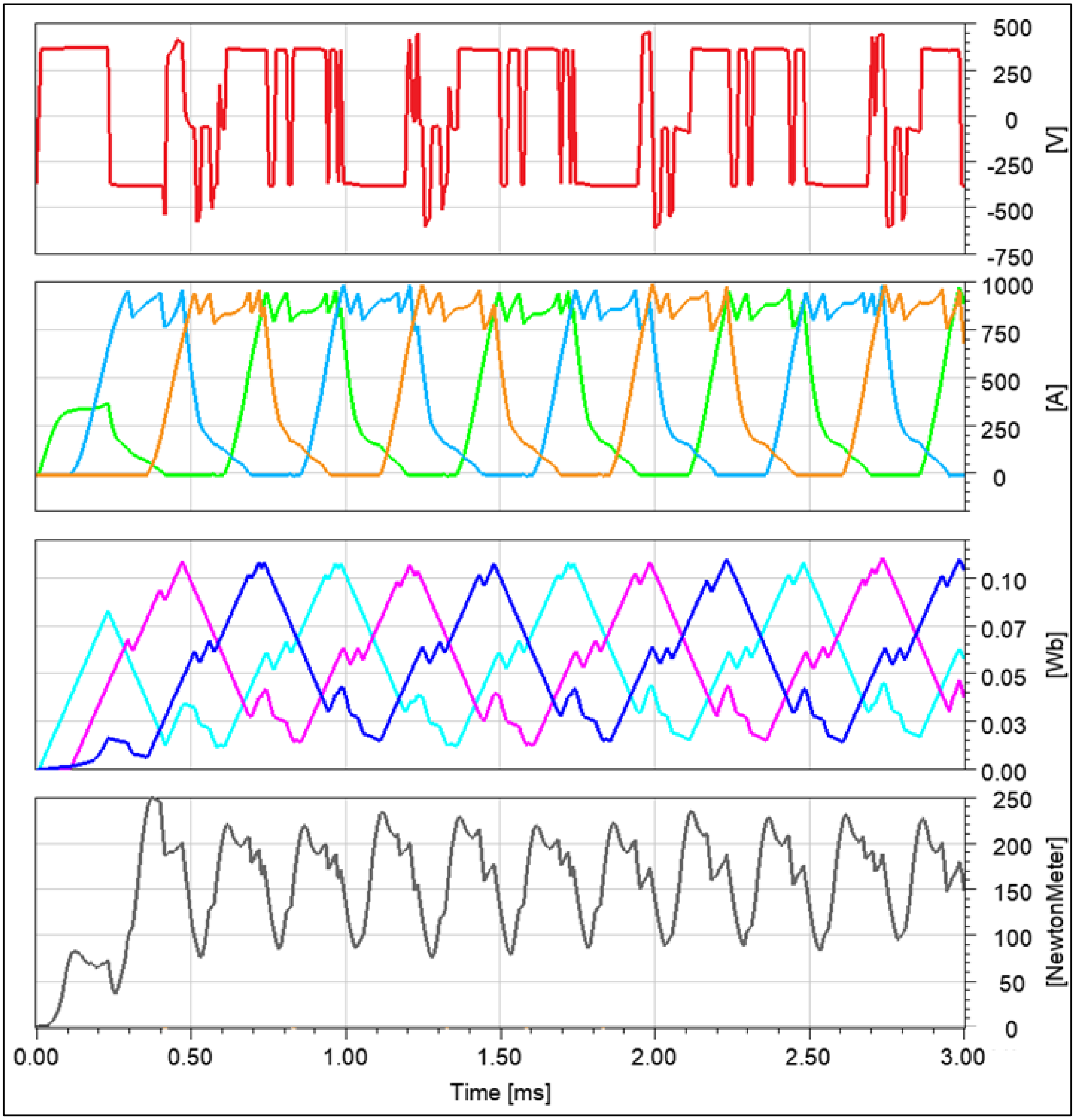

Figure 4.29 Phase ‘a’ voltage, three-phase currents, three-phase flux-linkages, and torque waveforms from FEA transient simulations at 10,000 rpm.

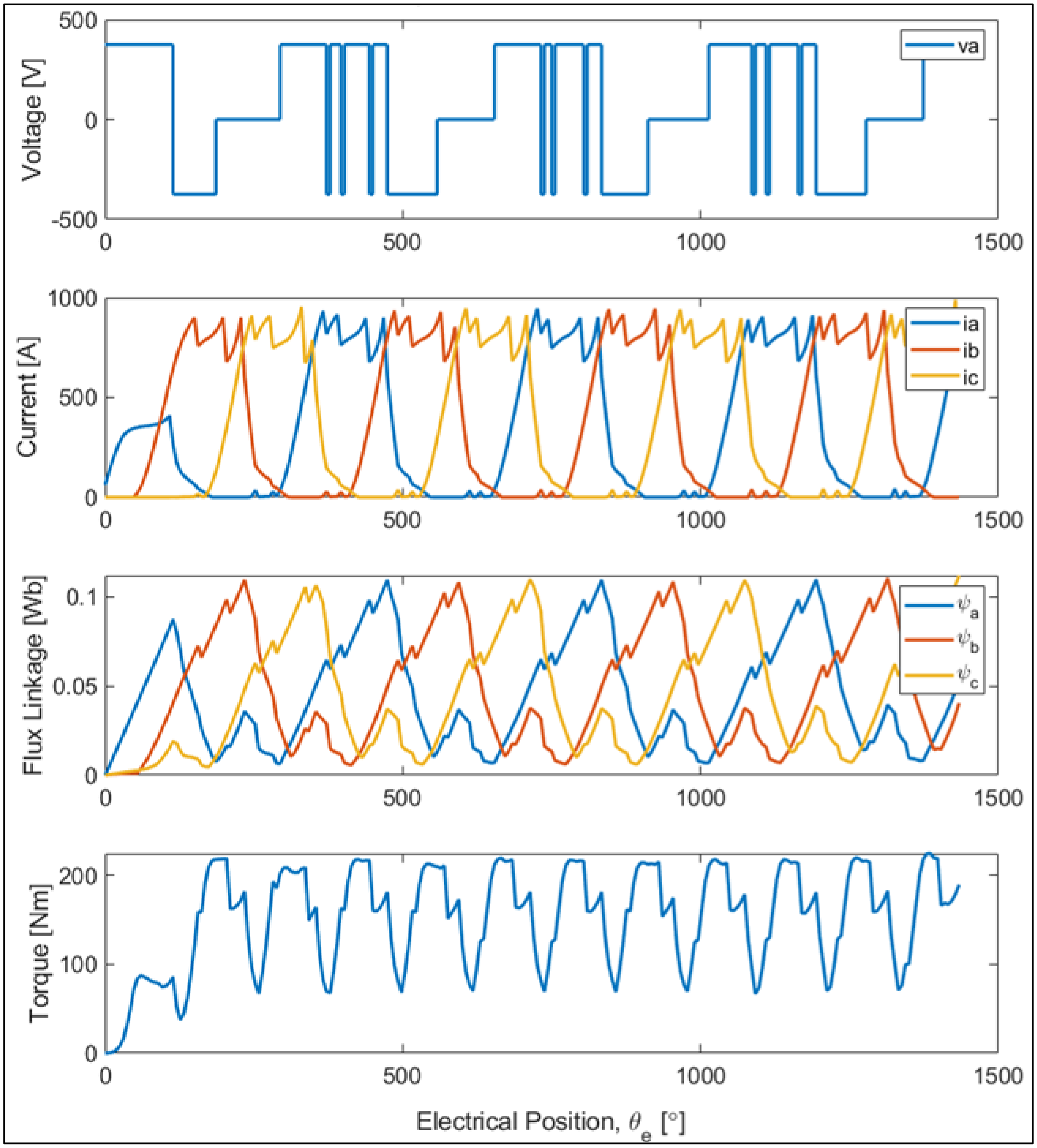

Figure 4.30 Phase 'a' voltage, three-phase currents, three-phase flux-linkages, and torque waveforms from code-based voltage-fed transient simulations at 10,000 rpm.

Close agreement with transient FEA was achieved across the entire torque-speed region. Using a mid-performance desktop PC, transient FEA solve times ranged from ~1-3 minutes per point with 16 cores while the voltage fed model solve time ranged from 0.5-3 seconds with a single core. Machine mapping with magnetostatic FEA consumed about 2 hours for Stage 2 and 6 hours for Stage 3. The short solve time greatly facilitates comprehensive optimization of control conditions throughout the torque-speed range.

For Stage 2 simulations at maximum speed, torque, efficiency, and torque ripple were determined as various types of single pulses were applied to the windings. Using conventional SRM control terminology, the advance angle, θ_a, is the amount of angular advance of the phase turn-on state (or the rising edge of the pulse in this case) with respect to the aligned condition of the stator and rotor teeth, and the dwell angle, θ_d, is the angular duration over which the phase is in the on-state.

Similar down-selection methods were used for Stages 2 and 3. Optimal control conditions were determined (in Stage 3 simulations with conventional control) by sweeping θ_a and θ_d at a given speed and reference current, then interpolating the resulting map for each targeted torque level. As an example, contours of average torque, torque ripple, and efficiency are shown for various combinations of θ_a and θ_d at 10,000 rpm and reference current of 400 A in Figures 4.31 (a), (b), and (c), respectively. A red contour for an average torque of 130 N-m is superimposed onto the torque ripple and efficiency contour plots in Figures 4.31 (b) and (c), respectively. For any control method, the impact of various control conditions can be visualized by plotting efficiency versus torque ripple, such as in Figure 4.32, where the plot includes results from various combinations of θ_a and θ_d that produce 130 N-m for each given reference current.

A performance function can be used to determine which control conditions to use at each operation point. For this example, a simple performance function to determine the value of various control parameters was defined as

$$P_{ctrl} = k_{eff-ctrl}\,\overline{\eta} + \left(1 - k_{eff-ctrl}\right)\left(1 - \overline{\tau_{ripple}}\right) \tag{4.3}$$

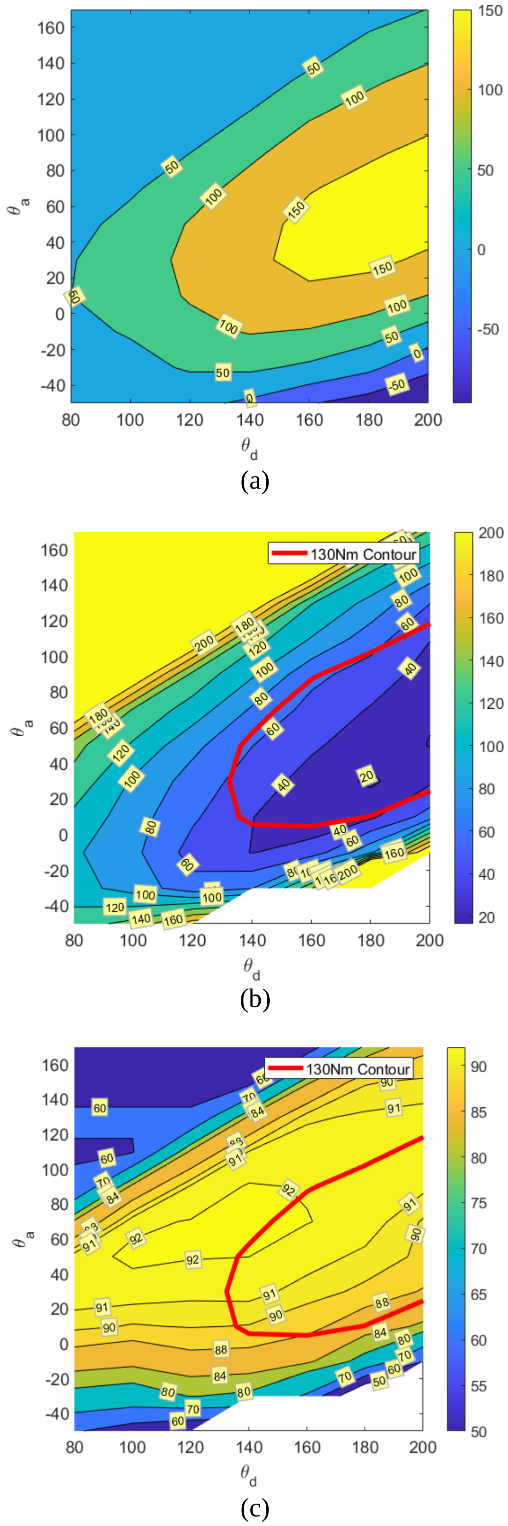

Figure 4.31 Average torque, torque ripple, and efficiency contour maps for advance and dwell control angle sweeps with code-based transient simulations at 10,000 rpm.

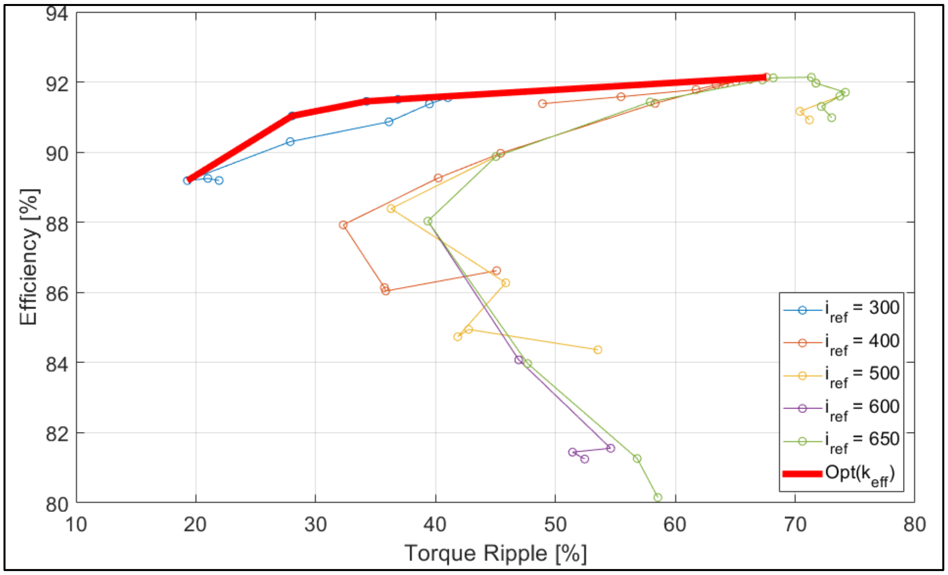

Figure 4.32 Efficiency versus torque ripple for various reference currents and a torque of 130 N-m.

where $\overline{\eta}$ and $\overline{\tau_{ripple}}$ are efficiency and torque ripple arrays normalized with respect to the control conditions at each torque-speed point, and $k_{eff-ctrl}$ is a weighting factor varying from 0 to 1, with 0 correlating with full prioritization of torque ripple minimization and 1 correlating with full prioritization of efficiency maximization. The red trace in Figure 4.32 indicates the optimal efficiency and torque ripple relationship determined by evaluating the performance function as $k_{eff-ctrl}$ ranges from 0 to 1. Therefore, control conditions can be selected based on the evaluation of the performance function at each operation point as $k_{eff-ctrl}$ is selected based on requirements of the application. The approach for Stage 2 is similar but has only one reference current (maximum current) and relies on more coarse torque and flux linkage maps from static FEA.

The control performance function was implemented at many points throughout the torque-speed operation region and contour plots of θ_a, θ_d, and i_{ref} with $k_{eff-ctrl}$ = 0 are shown in Figures 4.33(a), 4.33(b), and 4.33(c), respectively, for all torques and speeds. Similarly, contour plots of θ_a, θ_d, and i_{ref} with $k_{eff-ctrl}$ = 1 are shown in Figures 4.33(d), 4.33(e), and 4.33(f), respectively for all torques and speeds. In general, minimum torque ripple control conditions correlate with more overlap between phases with a lower peak current while maximum efficiency control conditions correlate with less overlap and higher current across positions with higher torque-per-ampere.

To determine the value of each geometry across multiple points in the torque-speed plane, a performance function such as the following can be defined:

$$\begin{aligned} P_{TS} = \; & k_{eff-TS_1}\,\overline{\eta_1} + \left(1 - k_{eff-TS_1}\right)\left(1 - \overline{\tau_{ripple_1}}\right) + \\ & k_{eff-TS_2}\,\overline{\eta_2} + \left(1 - k_{eff-TS_2}\right)\left(1 - \overline{\tau_{ripple_2}}\right) + \ldots \\ & k_{eff-TS_m}\,\overline{\eta_m} + \left(1 - k_{eff-TS_m}\right)\left(1 - \overline{\tau_{ripple_m}}\right) \end{aligned} \tag{4.4}$$

where $\overline{\eta_{\mathrm{p=1\to m}}}$ and $\overline{\tau_{ripple_{\mathrm{p=1\to m}}}}$ are efficiency and torque ripple arrays normalized with respect to all geometries at each torque-speed point, *p*, and $k_{eff-TS_{\mathrm{p=1\to m}}}$ are weighting factors ranging from 0 to 1, with k_{eff-TS_p} = 0 correlating with full prioritization of torque ripple minimization and k_{eff-TS_p} = 1 correlating with full prioritization of efficiency maximization. The weighting factor can be selected based on the importance of torque ripple or efficiency in different areas of

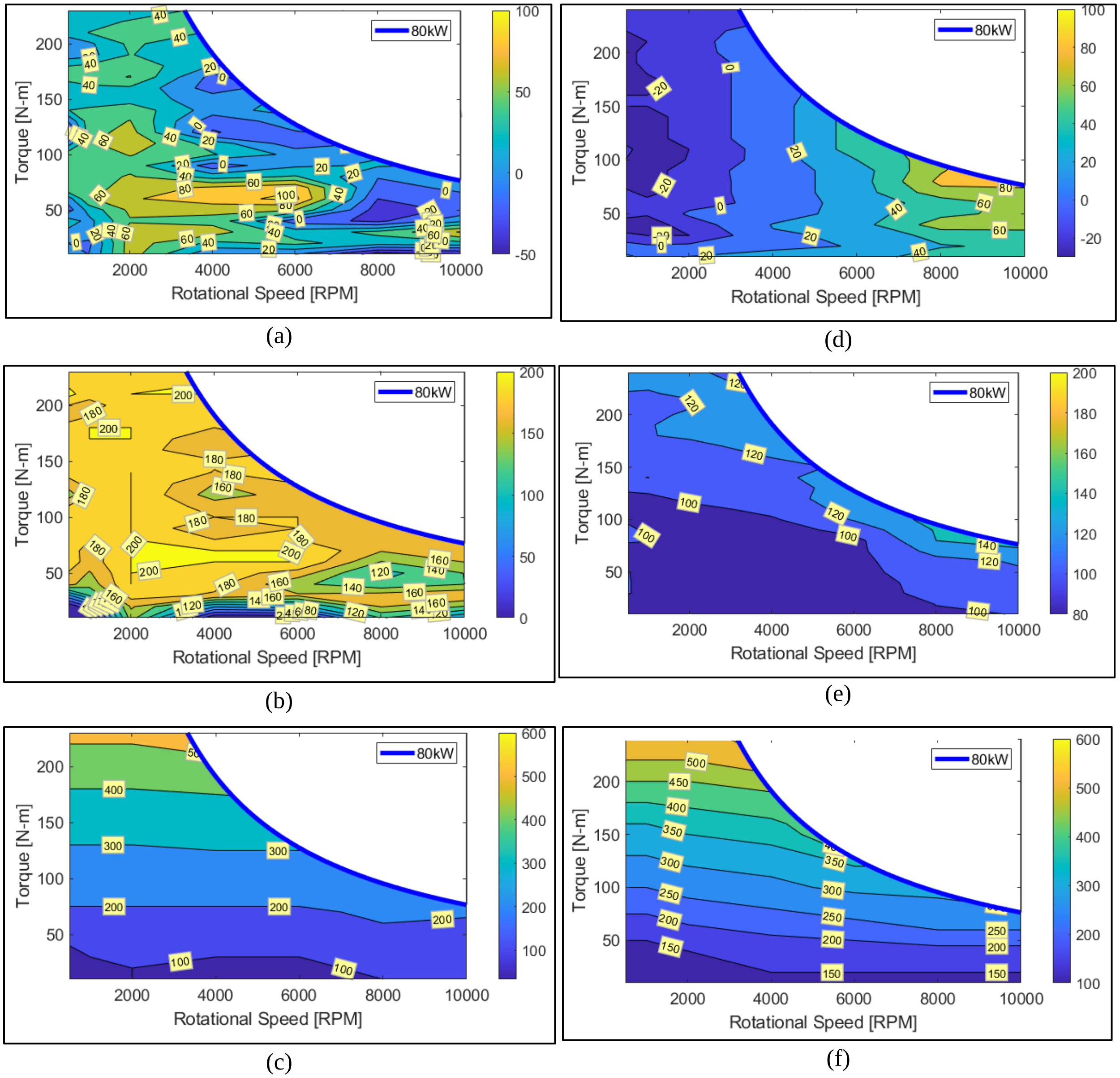

Figure 4.33 Contour plots of θ_a (a), θ_d (b), and i_{ref} (c) for all torques and speeds with $k_{eff-ctrl}$ = 0, respectively, and θ_a (d), θ_d (e), and i_{ref} (f) for all torques and speeds with $k_{eff-ctrl}$ = 1, respectively.

the torque-speed range. For example, torque ripple minimization is more important for low speeds as vibrations can be felt more easily by the passenger, whereas torque ripple minimization at higher speeds is less important due to natural inertia related damping and road vibration.

For demonstration purposes, down-selections in Stage 2 were performed using three combinations of $k_{eff-ctrl}$ = k_{eff-TS} = 0, 0.5, and 1. As a part of Stage 3, the resulting three geometry solutions were simulated with the voltage fed model with detailed torque and flux-linkage mapping from 2D FEA as control parameters were swept at each torque-speed point to generate a full mapping of efficiency and torque ripple. Efficiency contour plots for geometry 2 shown in Figures 4.34 and 4.35 correlate with $k_{eff-ctrl}$ = 0 and 1, respectively, as the performance equation (4.4) was maximized at each point throughout the entire torque-speed range. Similarly, torque ripple contour plots in Figures 4.36 and 4.37 correlate with $k_{eff-ctrl}$ = 0 and 1 throughout the entire torque-speed range, respectively.

Efficiency and torque ripple for all three geometries at the 500 rpm, 230 Nm operation point (indicated by one of the red circles in the contour plots) is shown in Figures 4.38(a) and 4.38(b), respectively, for $k_{eff-ctrl}$ = 0, 0.5, and 1. For almost all control conditions, efficiency is maximized and torque ripple is minimized with geometry 2. Analogous to what is indicated in Figures 4.15 and 4.16, geometry 1 is a machine with more winding area, geometry 3 is a machine with less winding area and thicker iron segments, while geometry 2 is a compromise between the two. The torque-speed performance equation (4.4) was implemented while including all three points indicated by red circles on the contour plot and the resulting performance of all three geometries is plotted versus k_{eff-TS} for $k_{eff-ctrl}$ = 0, 0.5, and 1, in Figures 4.39(a), 4.39(b), and 4.39(c), respectively. With the exception of a few conditions, it can be seen that the evaluated value of geometry 2 is greater than that of the other geometries. This demonstrates how the proposed framework can be used to achieve co-optimization of both machine and control conditions. The final optimal solution (geometry 2) correlates with D_{RO} = 130 mm, w_{Syoke} = 11 mm, k_{STW} = 1.1, k_{RTW} = 1.1, and l_{Rtooth} = 20 mm.

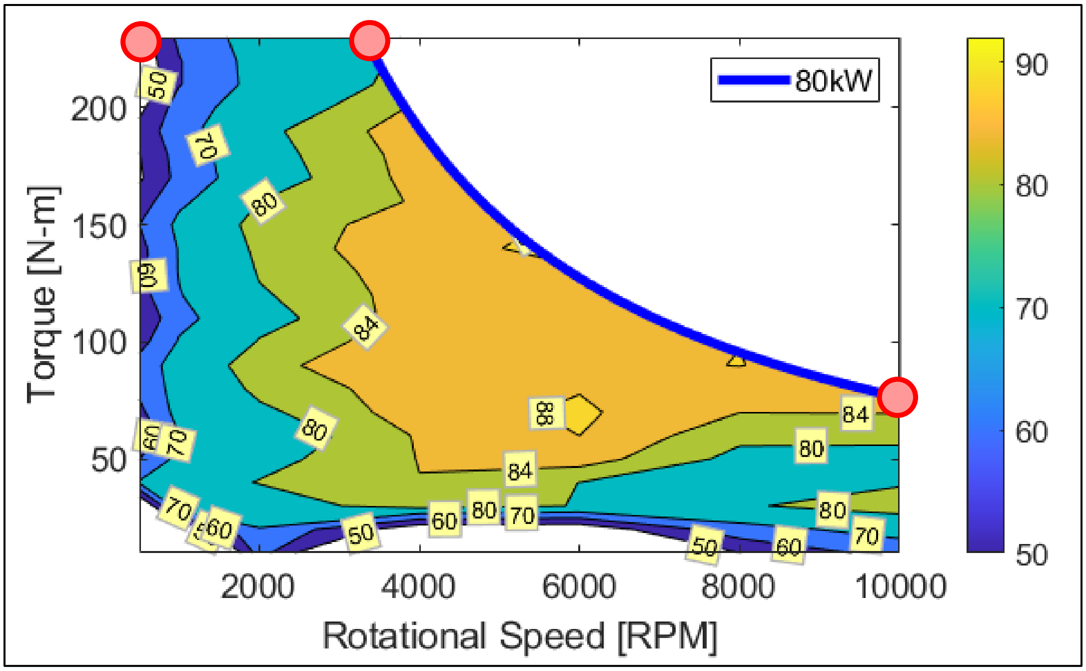

Figure 4.34 Contours of simulated efficiency [%] plotted for torque versus speed for geometry index 2 with $k_{eff-ctrl} = 0$.

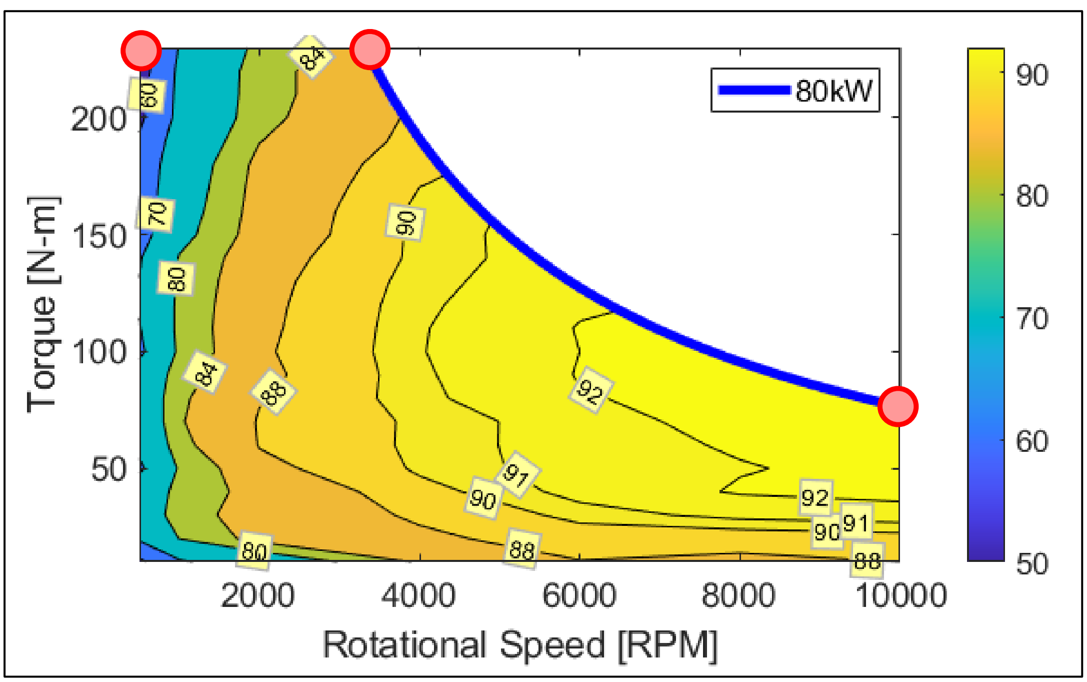

Figure 4.35 Contours of simulated efficiency [%] plotted for torque versus speed for geometry index 2 with $k_{eff-ctrl} = 1$.

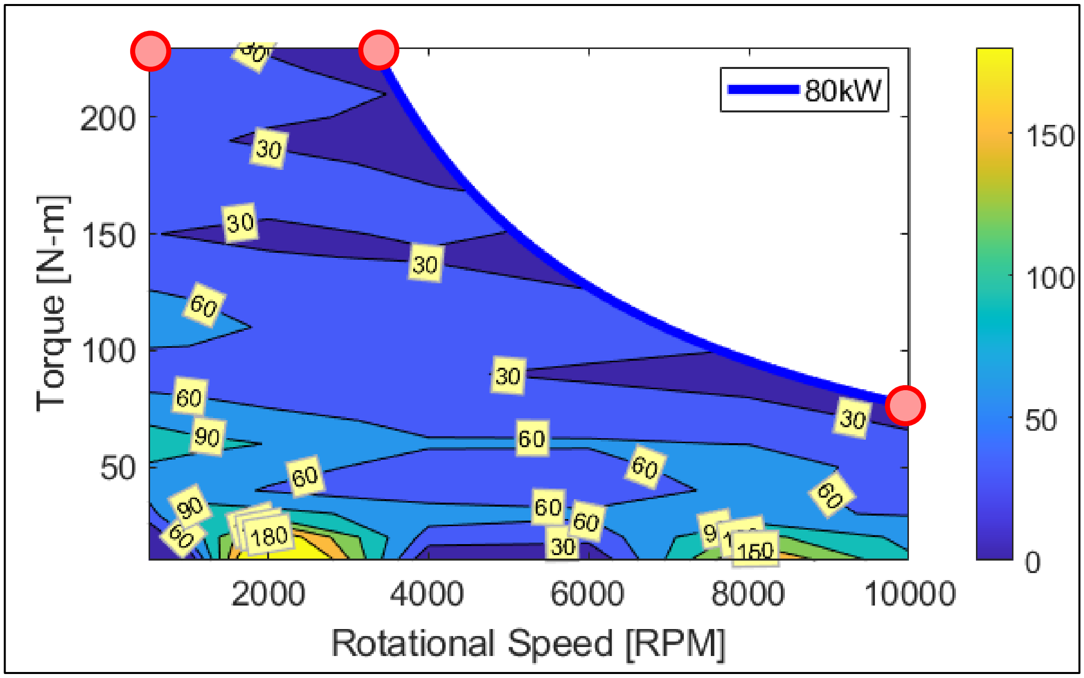

Figure 4.36. Contours of simulated torque ripple [%] plotted for torque versus for geometry index 2 speed with $k_{eff-ctrl}$ = 0.

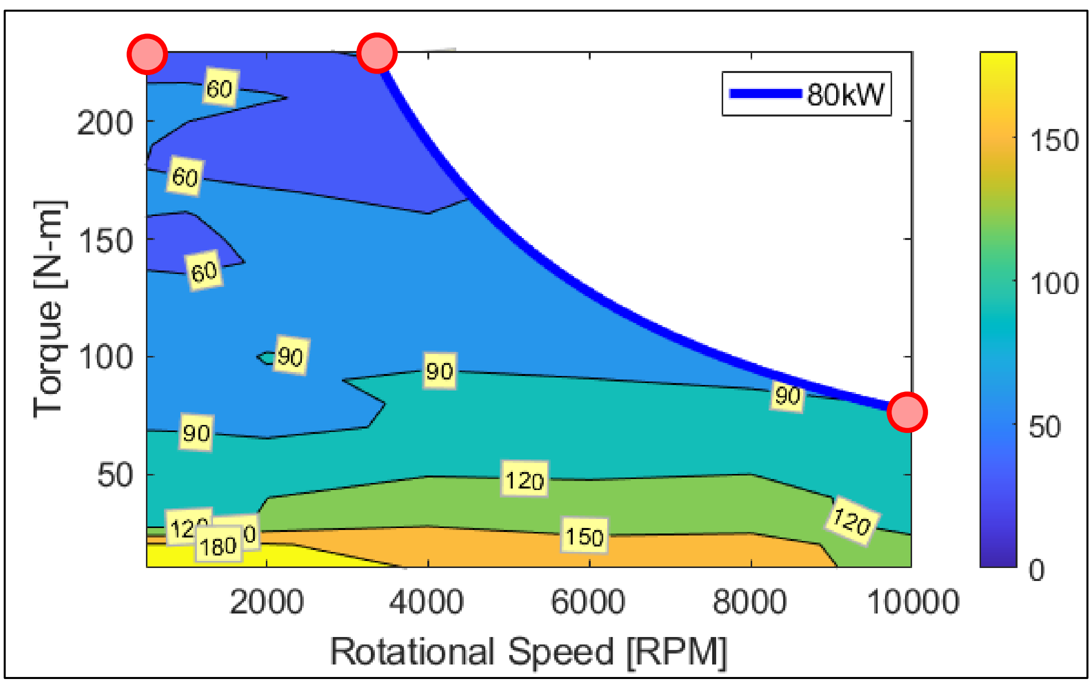

Figure 4.37 Contours of simulated torque ripple [%] plotted for torque versus for geometry index 2 speed with $k_{eff-ctrl}$ = 1.

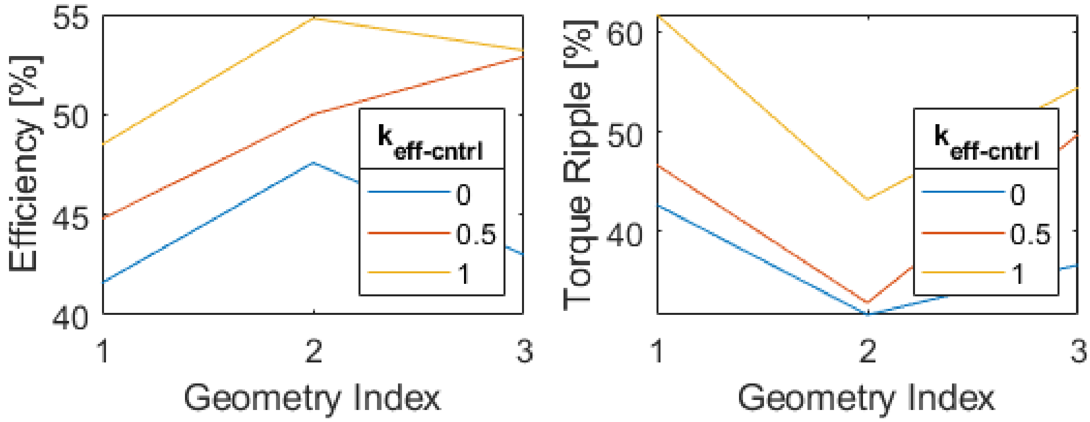

(a) (b)

Figure 4.38 Simulated efficiency (a) and torque ripple (b) of three geometries at 500 rpm and 230 N-m for various control weighting factors, $k_{eff-ctrl}$.

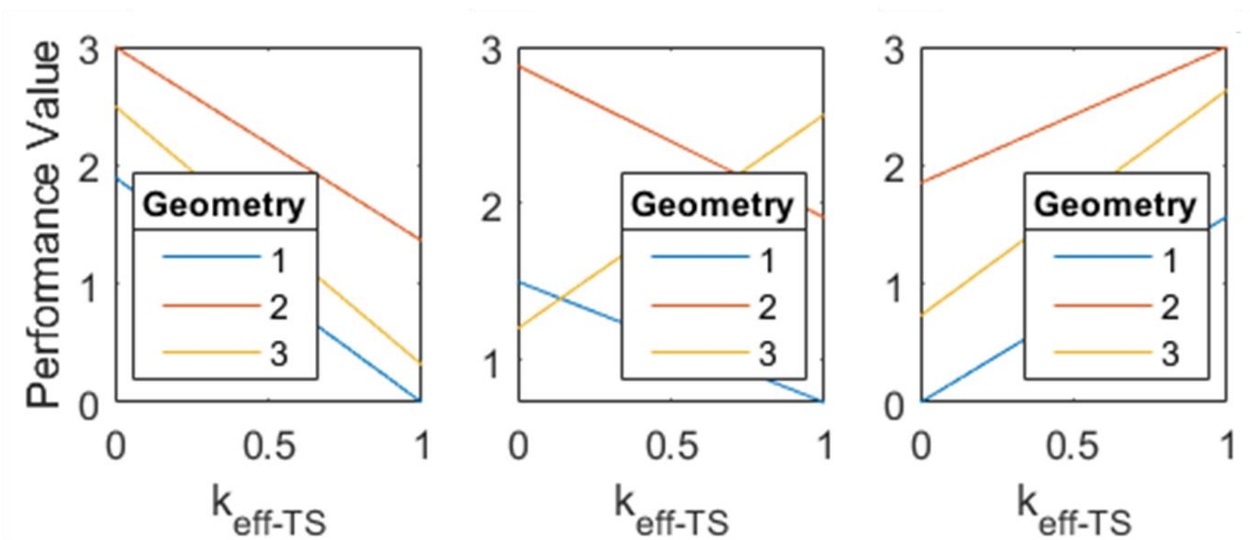

(a) (b) (c)

Figure 4.39 Machine performance versus k_{eff-TS} for three geometries with $k_{eff-ctrl}$ = 0 (a), 0.5 (b), and 1 (c).

Summary and Conclusions

The benefits of a three-stage co-optimization process were demonstrated using static FEA torque and flux linkage mapping with custom code-based transient models that enable advanced evolutionary control optimization algorithms to be implemented with broad parameterized sweeps of machine design parameters. Static FEA simulations were performed in Stage 1 at zero-speed conditions to determine an initial solution space, adjust nominal parameters as necessary, and establish a fundamental understanding of the correlation between various geometric parameters and operational quantities such as average torque, torque ripple, and current density. Exemplar performance functions were implemented to perform optimization of control conditions and the machine design with weighting factors that allow the designer to balance priority between torque ripple minimization and efficiency maximization. A design was selected for testing based on performance function evaluation.

References

[4.1] T. Burress, "Benchmarking State-of-the-Art Technologies", *2013 U.S. DOE Hydrogen and Fuel Cells Program and Vehicle Technologies Program Annual Merit Review and Peer Evaluation Meeting*, May 14th, 2013.

[4.2] J. Gieras, *Advancements in Electric Machines,* Springer London Limited, 2008.

CHAPTER FIVE: PROTOTYPE FABRICATION AND EXPERIMENTAL EVALUATION

Portions of this chapter will be published by Timothy Burress and Dr. Leon Tolbert:

T. Burress, L. M. Tolbert, “Multiple Objective Co-Optimization and Experimental Evaluation of Switched Reluctance Machine Design and Controls,” *IEEE International Electric Machine and Drives Conference*, San Francisco, California, May 15-18, 2023.

Abstract

A new modeling framework and optimization approach is proposed in Chapter 3 for co-optimization of both switched reluctance machine (SRM) design and control across the entire torque-speed range. Design down-selection was performed based on control and machine performance functions in Chapter 4. The final design is scaled in preparation for empirical validations of custom modeling codes and control performance functions. Fabrication, test setup, and test results are discussed in this chapter as modeling results are validated and the effectiveness of the proposed approach is confirmed.

Overview

A final design was selected in Chapter 4 based on performance function evaluations as broad sweeps of geometric parameters and control conditions were conducted. To reduce the cost and challenges of fabricating and setting up a large SRM for prototype testing, the final design was scaled to a 5 hp (3.7 kW) power level. After scaled design parameters are established, control optimization in Stage 3 is implemented to generate reference control conditions for the scaled prototype across the torque-speed operation range.

Fabrication and testing of the SRM prototype provides an evaluation of model accuracy and validation of the control optimization process. Accuracy of the models is evaluated by comparing simulated and empirical results. Testing at various torques and speeds demonstrates the effectiveness of the optimization approach throughout the entire operating range. Furthermore, test results confirm the feasibility of the proposed optimization approach that gives the machine and control designer the ability balance torque ripple minimization and efficiency maximization according to the needs of the targeted application.

Scaling for Prototype

The cost to fabricate a protype motor is largely impacted by the cost of having steel laminations laser cut for the stator and rotor cores. This cost is driven by the amount of time the laser cutting machine spends cutting the material, which is roughly proportional to the size of the machine. Furthermore, a large machine also constitutes more challenging requirements regarding lifting, safety containment, power supply, and drive hardware. The overall scope of this work is to demonstrate a co-optimization technique and the ability of an on-line controller to regulate the optimized waveforms, and this can be demonstrated regardless of machine size and performance. Therefore, to reduce prototyping costs and avoid other unnecessary challenges, the final design was scaled to a smaller size and a summary comparison of the original and scaled geometric parameters is provided in Table 5.1. Many of the parameters were determined based on the selection of the housing, bearing, and cooling system of the Hyundai Sonata Hybrid Starter-Generator to be used rather than designing and building a motor entirely from scratch. Key parameter changes include the reduction of the stator OD from 200 mm to 127.91 mm, rotor OD from 130 mm to 83.14 mm, stator/rotor stack length from 196.3 mm to 76.2 mm, rotor tooth length from 20 mm to 12.99 mm, and stator yoke thickness from 11 mm to 7 mm.

A summary comparison of original and scaled operational parameters of the final design selection is provided in Table 5.2. Key operational parameter changes include a reduction of the dc-link voltage from 375 V to 340 V, maximum power from 80 kW to 3.7 kW, and maximum torque from 280 Nm to 15 Nm. The reduction of maximum speed from 10,000 rpm to 6,000 rpm reduces balancing, alignment, and safety containment requirements. The phase current rating was lowered from 450 Arms to 12.5 Arms based on ratings of the selected power stage. The targeted fill factor was reduced from 0.6 to 0.35 because smaller motors typically have reduced fill factors as smaller slots present more difficulty for wire installation and slot liners have a similar thickness even though the slot size is considerably smaller. For these reasons, the targeted fill factor was reduced considerably to mitigate risk of progress delays during motor fabrication.

Based on the targeted current density, fill factor, and phase rating, equations (3.9) and (3.10) were used to assist in determining the appropriate winding configuration. To reduce complications during the winding process, an option was chosen with single strand of 20 AWG, versus multiple strands which add more difficulty during the winding process. The configuration with 54 turns, no parallel coils ($N_{par} = 1$), and four series coils ($N_{ser} = 4$) per phase was selected.

Table 5.1 Comparison of original and scaled geometric parameters of final design selection.

Parameter	Original	Scaled
Airgap	0.5 mm	0.32 mm
Stator OD	200 mm	127.91 mm
Stator ID	131 mm	83.78 mm
Stator and Rotor Length	196.3 mm	76.2 mm (3”)
Rotor OD	130 mm	83.14 mm
Rotor ID	23.01 mm	22.99 mm (0.905”)
Coil Area	215.62 mm^2	83.84 mm^2
Rotor Tooth Factor, RTF	1.1	1.1
Stator Tooth Factor, STF	1.1	1.1
Rotor OD, ROD	130 mm	83.14 mm
Rotor Tooth Length, RTL	20 mm	12.99 mm
Stator Yoke Thickness, Syoke	11 mm	7 mm

Table 5.2 Comparison of original and scaled operational parameters of final design selection.

Parameter	Original	Scaled
Vdc	375 V	340 V
Maximum Power	80 kW	5 hp (3.7 kW)
Maximum Torque	280 Nm	15 Nm
Maximum Speed	10,000 rpm	6,000 rpm
Peak Phase Current	900 A	25 A (drive rating)
Phase Current Rating	450 Arms	12.5 Arms
Copper Current Density	15 Arms/mm^2	23 Arms/mm^2
Current Density	9 Arms/mm^2	8.05 Arms/mm^2
Fill Factor, FF	0.6	0.35

Prototype Fabrication

Stator and rotor cores, shown in Figure 5.1, were fabricated by a laser cutting vendor using 0.35mm thick (29 gauge or 0.014”) M270-35A grade electrical steel. Slot liners made of Nomex 410 insulation paper were cut and installed prior to installation of the copper windings. Each coil consists of 54 turns of a single strand of 20 AWG magnet wire. A total of 12 coils were fabricated and installed, with four coils connected in series for each phase of the SRM. A thermistor was installed in the motor winding end-turns near a slot for temperature feedback. The stator and windings were vacuum impregnated with Dolph’s CC-1105 varnish, as shown in Figure 5.2. A comparison of the motor before and after varnish is shown in Figures 5.3 (a) and (b), respectively. Varnish or potting processes are always used for electric motors to help secure the windings, avoid winding degradation and failure due to vibration, and to promote heat transfer between wires and the stator itself. As shown in Figure 5.4, the stator was pressed into the housing and the rotor laminations, bearings, and custom spacer were installed on the rotor shaft. The rotor assembly was installed inside the stator (Figure 5.5(a)), and the motor was fully assembled (Figure 5.5(b)).

Test Setup

The SRM prototype was installed with a dynamometer test setup, shown in Figures 5.6 and 5.7, so empirical validations can be performed. Motor efficiency was calculated using the ratio of mechanical power measured with a torque and speed meter to input electrical power measured with voltage and current transducers. Instantaneous torque waveforms were processed to determine torque ripple and average torque. An SRM drive, shown in Figure 5.8, based on the architecture shown in Figures 2.7 and 2.8, was constructed using two conventional power modules since three-phase power modules with asymmetric half bridges are not available. A control board with a Texas Instruments C2800 digital signal processor was modified and programmed to implement and compare conventional SRM hysteresis control and the proposed predictive control methods. The SRM control board includes signal conditioning to facilitate three-phase current feedback from current transducers, and a separate resolver board is used for position feedback from a position resolver mounted on the SRM shaft. The control loop was executed at a rate of 40 kHz.

Figure 5.1 SRM prototype stator and rotor laminations.

Figure 5.2 Varnish and vacuum impregnation process.

(a) (b)

Figure 5.3 SRM stator (a) before and (b) after varnish.

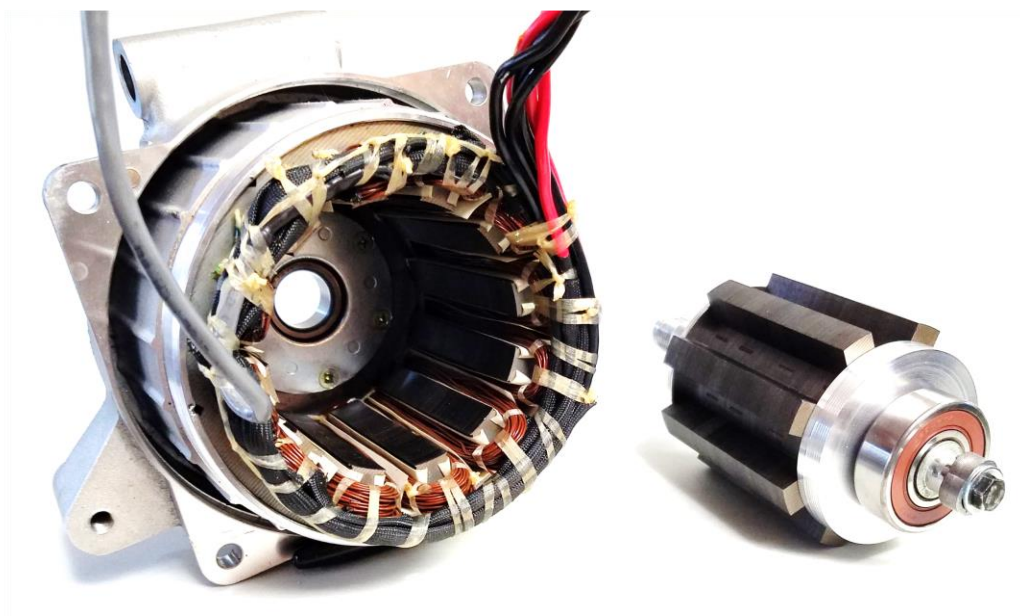

Figure 5.4 SRM stator pressed into housing and rotor fully assembled.

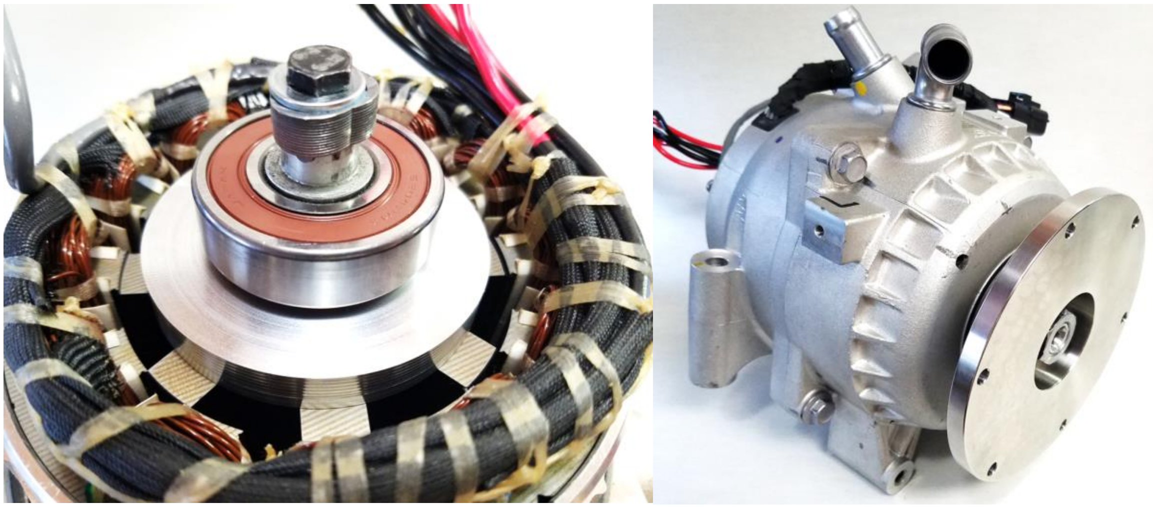

(a) (b)

Figure 5.5 (a) SRM rotor assembly installed and (b) motor fully assembled for testing.

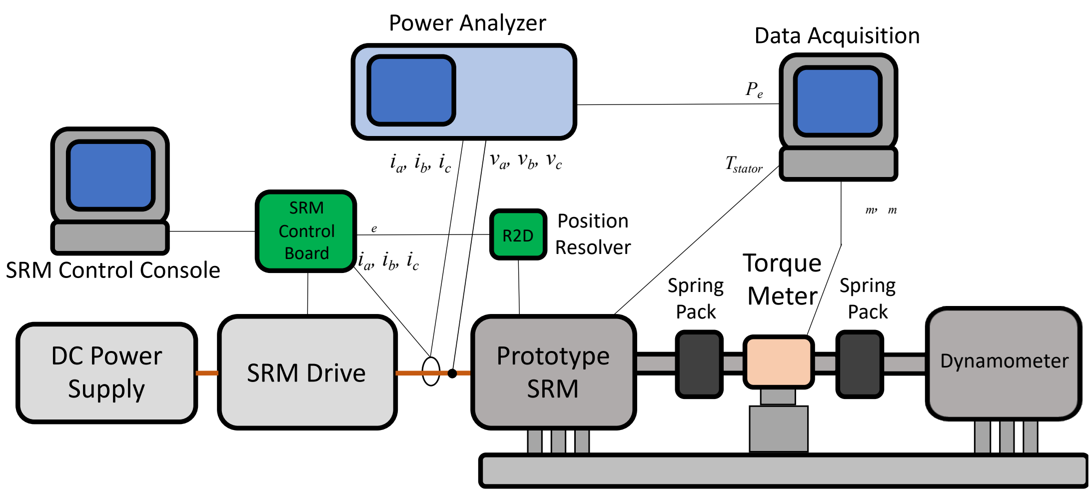

h

Figure 5.6 Setup implemented for SRM design and control empirical evaluation.

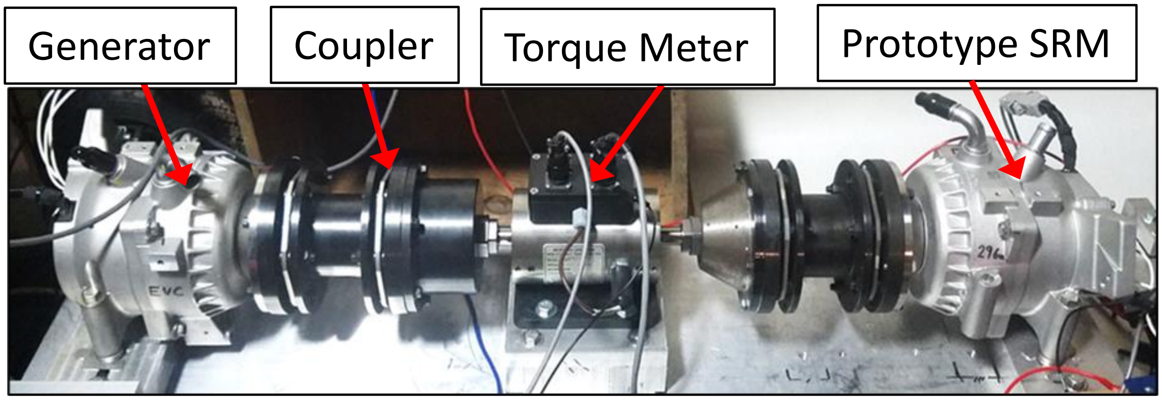

Figure 5.7 Test setup with protype SRM, torque meter, spring packs, and dynamometer.

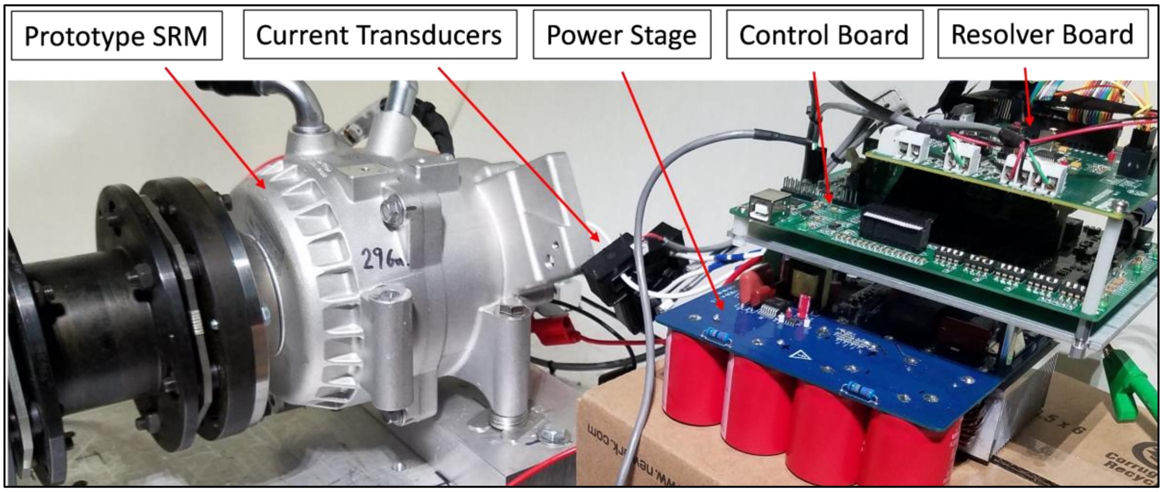

Figure 5.8 SRM prototype and SRM drive.

Test Results

Locked rotor torque measurements were made by using a mechanism to lock the SRM rotor shaft at various positions as DC current was applied. The measured locked rotor torque was about 2-5% lower than original FEA simulations depending on current level. Following locked rotor testing, static FEA simulations were conducted to assess torque and flux linkage as the airgap was varied in small increments and results are shown in Figure 5.9. An increase of the airgap by ~0.1 mm in FEA simulations resulted in a close match with experiments, as shown in Figure 5.10. This could be attributed to slight discrepancies between specified dimensions that were simulated and actual dimensions after laser cutting. Other causes for the discrepancy could be due to localized heating and associated degradation of magnetic properties that occurs as a result of laser cutting. Both phenomena would have the greatest impact at the airgap. Simulations were repeated with the new torque and flux-linkage mapping from 2D static FEA, and torque-speed maps of efficiency, torque ripple, and control conditions were generated for the $k_{eff-ctrl}$ = 0 and 1 conditions.

In general, minimum torque ripple control conditions correlate with more overlap between phases with a lower peak current while maximum efficiency control conditions correlate with less overlap and higher current across positions with higher torque-per-ampere. Simulated and measured voltage, current, and torque waveforms at 1,000 rpm and 8 Nm with $k_{eff-ctrl}$ = 0 (the minimal torque ripple control condition) are provided in Figures 5.11 and 5.12, respectively. While both oscilloscope waveforms and DSP waveforms are taken at the same torque and speed, it is important to note that the time scales for the oscilloscope data in the top plot and the DSP data in the bottom plot are not synchronized. Monitoring of the real time analog output of the torque transducer resulted in accurate average torque which matched the OEM torque readout. However, torque ripple was much lower than predicted as most torque transducers are not intended to measure instantaneous torque. Therefore, the experimental instantaneous torque was approximated by interpolating the simulated three-phase locked rotor torque based on measured three-phase currents and position.

Simulated and measured voltage, current, and torque waveforms at 6,000 rpm and 6 Nm with $k_{eff-ctrl}$ = 1 (the maximum efficiency control condition) are provided in Figures 5.13 and 5.14,

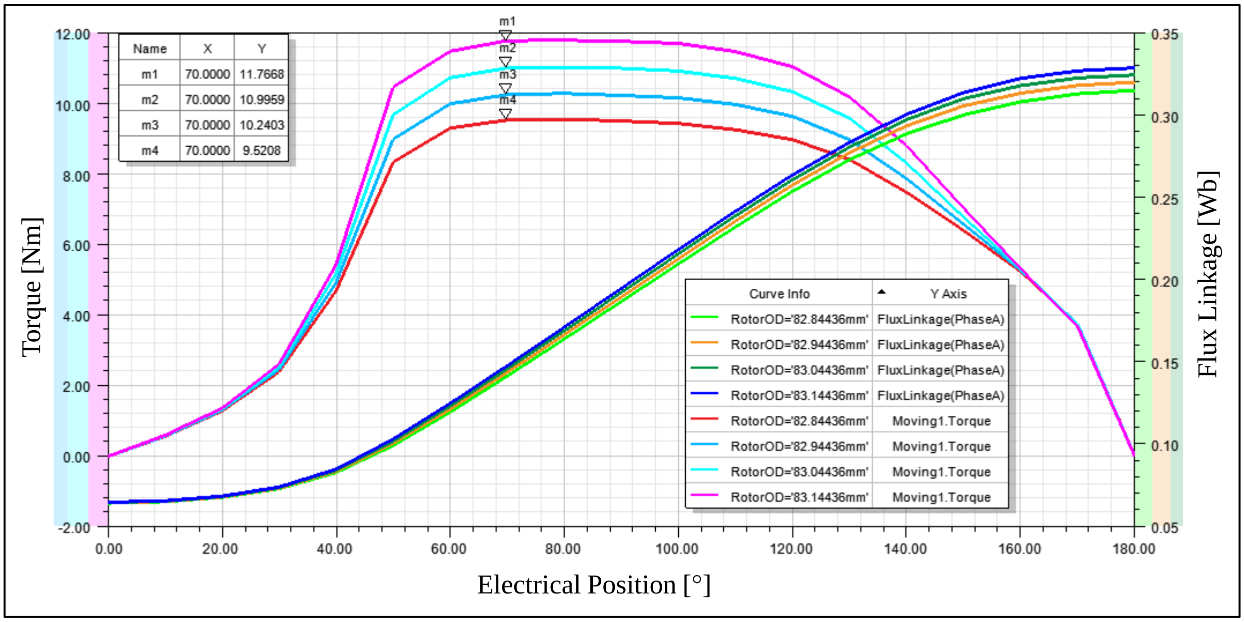

Figure 5.9 Torque and flux linkage versus position from static FEA simulations of scaled SRM prototype with slight variations in airgap.

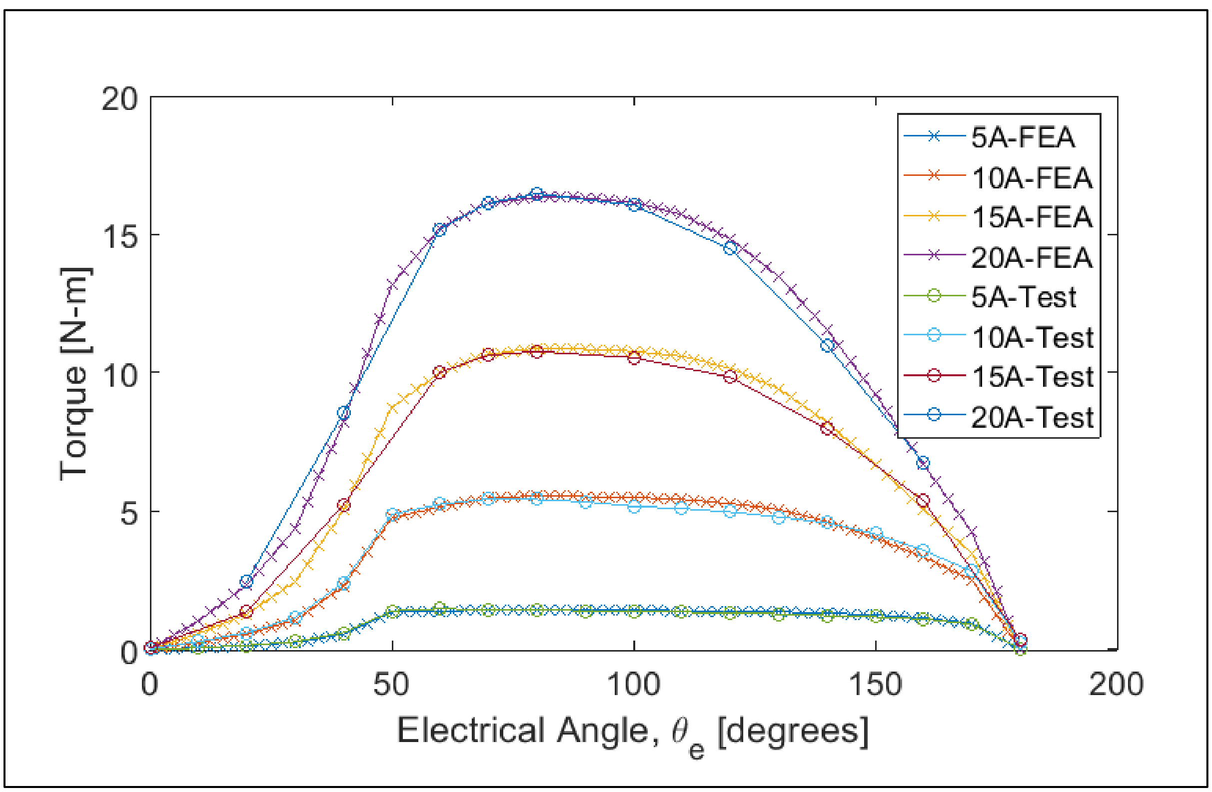

Figure 5.10 Measured and simulated SRM single phase locked rotor torque versus electrical angle for various currents.

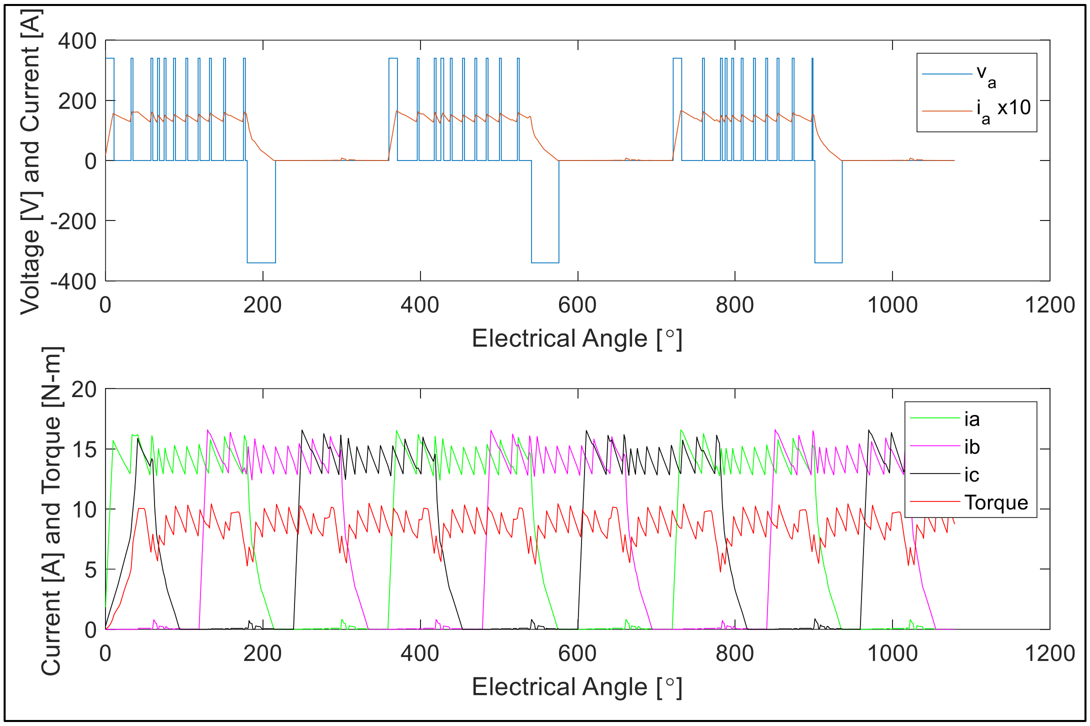

Figure 5.11 Simulated SRM voltage, current, and torque at 1,000 rpm and 8 Nm with $k_{eff-ctrl}$ = 0.

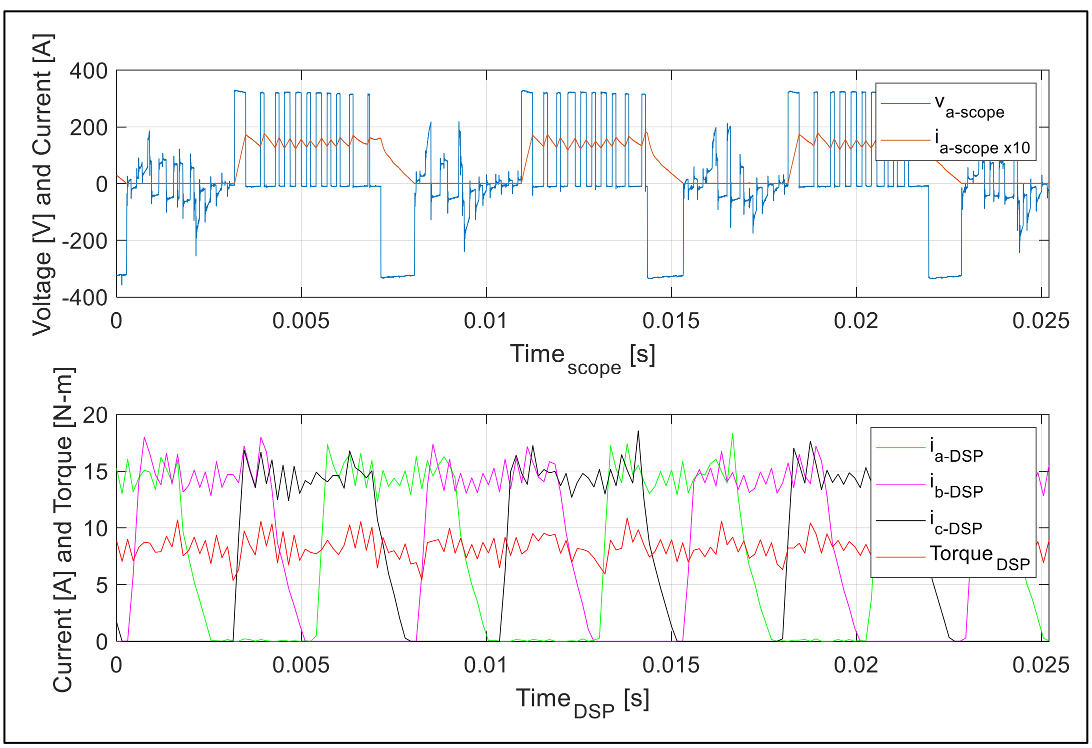

Figure 5.12 Measured SRM voltage, current, and experimental torque at 1,000 rpm and 8 Nm with $k_{eff-ctrl}$ = 0.

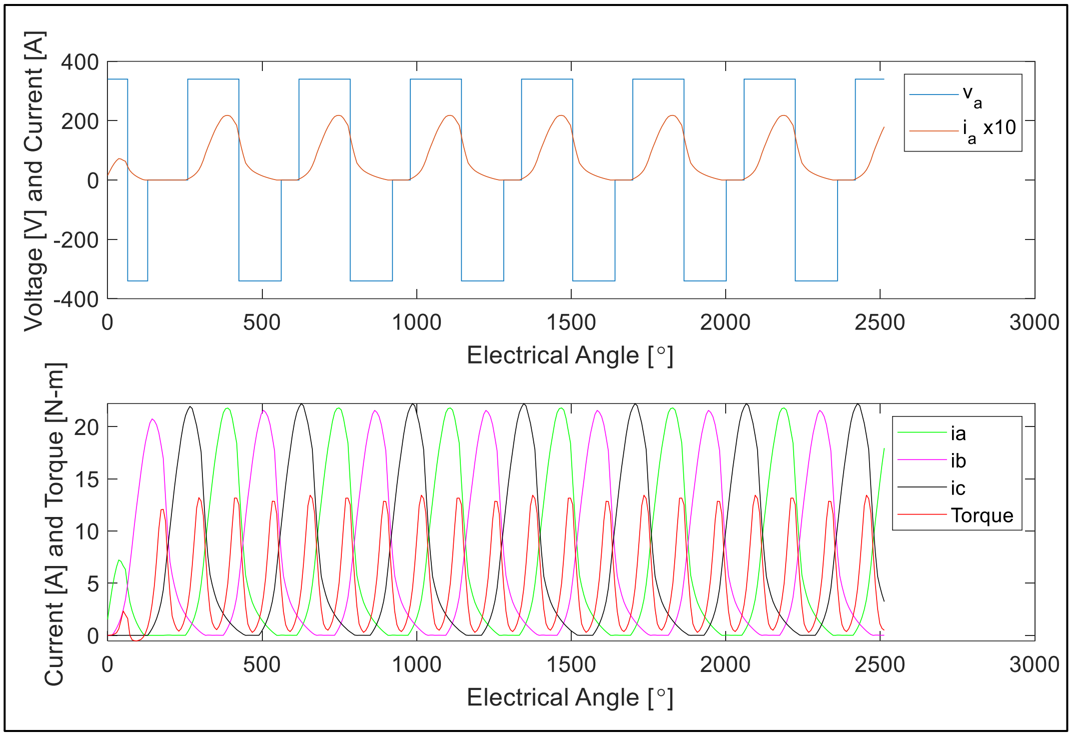

Figure 5.13 Simulated SRM voltage, current, and torque at 6,000 rpm and 6 Nm with $k_{eff-ctrl}$ = 1.

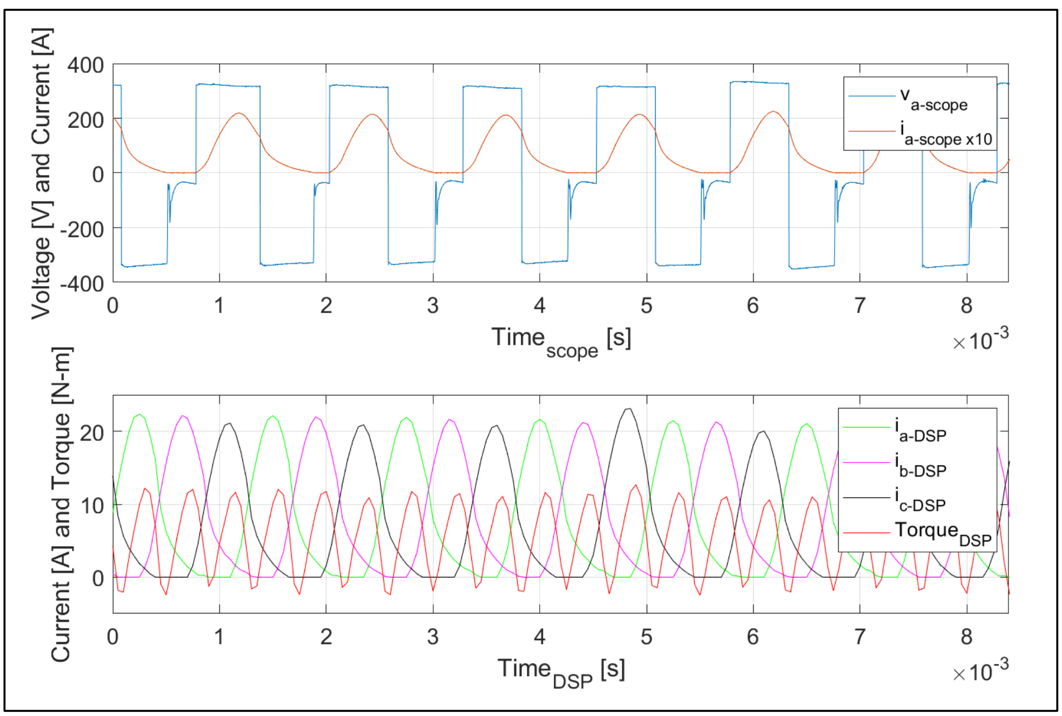

Figure 5.14 Measured SRM voltage, current, and experimental torque at 6,000 rpm and 6 Nm with $k_{eff-ctrl}$ = 1.

respectively. A slight variation is noticed when comparing the peaks of current waveforms, and this is attributed to the control loop frequency of 40 kHz. At 6,000 rpm the fundamental frequency of the phase voltage and current is 800 Hz, leading to a change in electrical position of ~7.2 degrees for every control loop cycle. Therefore, the actual applied pulse length differs slightly from cycle to cycle due to the random time difference between a phase 'on' or 'off' transition (i.e. based on the real position) and the measured position/current, time for processing, and corresponding update to the output state from the microprocessor. This behavior is also observed in simulation, in which the same control loop frequency was used. Even so, there is no significant impact noticed with machine operation. Overall, simulated waveforms match closely with measured waveforms.

Simulated and experimental torque ripple contours throughout the torque-speed range with $k_{eff-ctrl}$ = 0 are provided in Figures 5.15 and 5.16, respectively. Similarly, simulated and experimental torque ripple contours throughout the torque-speed range with $k_{eff-ctrl}$ = 1 are provided in Figures 5.17 and 5.18, respectively. For both control conditions, experimental torque ripple ranged from 8 to 15% higher than simulated torque ripple, and this discrepancy might be attributed to timing and switching characteristics of the DSP and power stage, instantaneous speed variation, and noise on the sampled current and position feedback.

Simulated and measured efficiency contour maps with $k_{eff-ctrl}$ = 0 are provided in Figures 5.19 and 5.20, respectively. Figures 5.21 and 5.22 show simulated and measured efficiency contours, respectively, for $k_{eff-ctrl}$ = 1. Close agreement can be observed throughout most of the torque-speed range. Discrepancies might be attributed to variations in winding temperature and loss predictions in the simulation.

Summary and Conclusions

The final solution from Stage 3 simulations discussed in Chapter 4 was scaled, fabricated, and tested to demonstrate the advantages of the proposed control and design optimization process as tests were conducted with control conditions with different optimization targets. The proposed framework was used to generate control conditions for two sets of tests, one with the optimization target minimum torque ripple and the other targeting maximum efficiency. Accuracy of the models

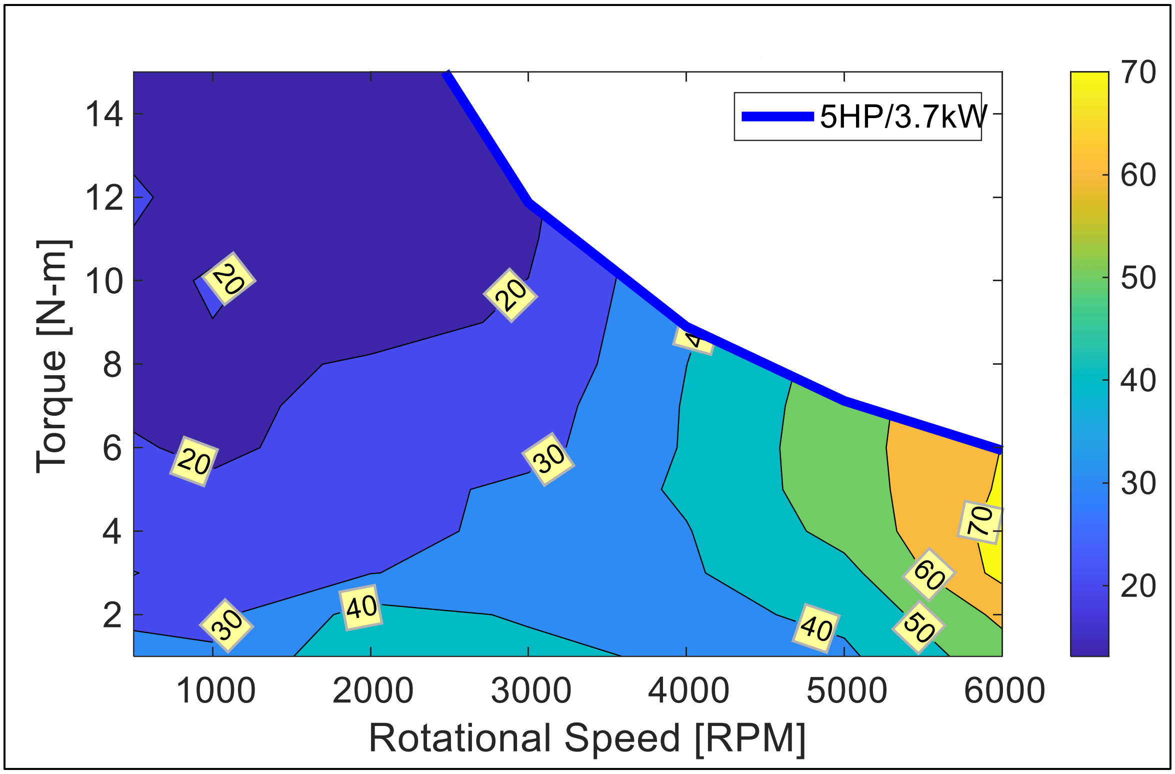

Figure 5.15 Simulated SRM torque ripple contours with $k_{eff-ctrl}$ = 0.

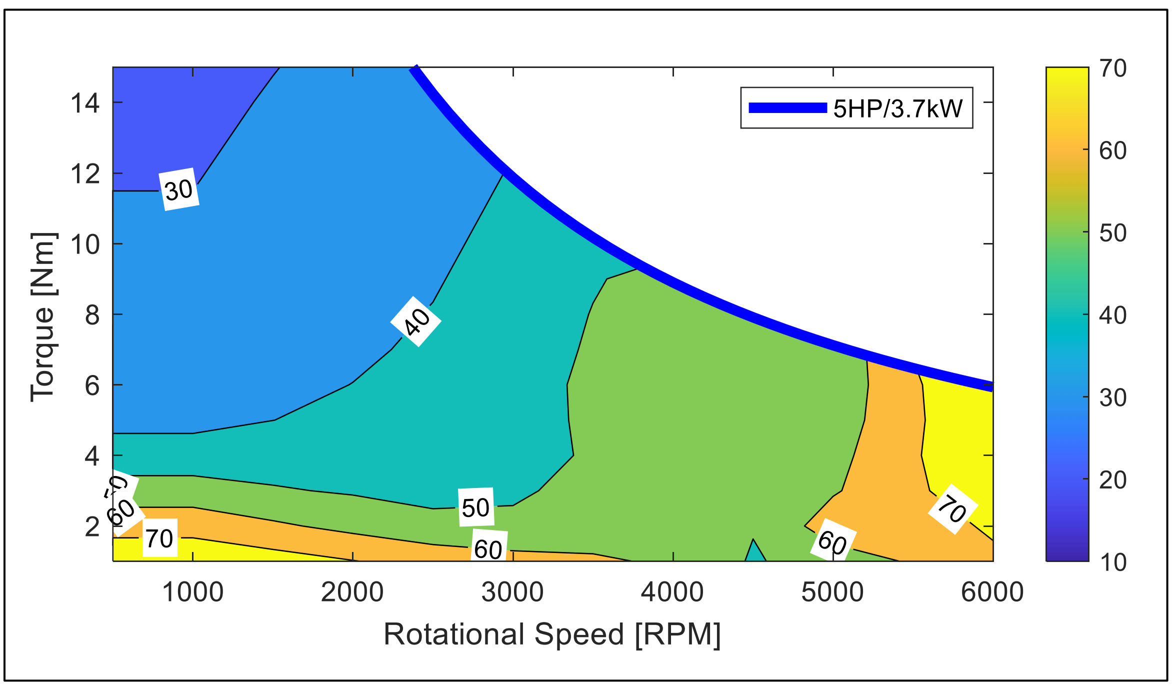

Figure 5.16 Experimental SRM torque ripple contours with $k_{eff-ctrl}$ = 0.

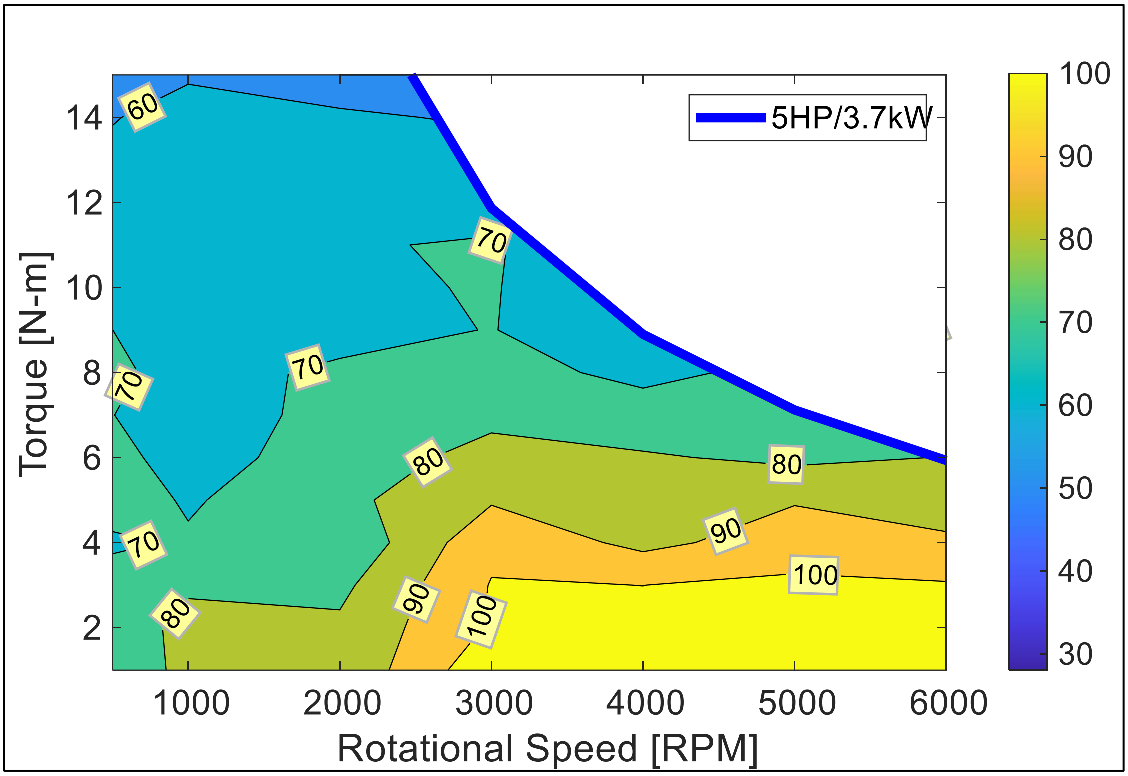

Figure 5.17 Simulated SRM torque ripple contours with $k_{eff-ctrl} = 1$.

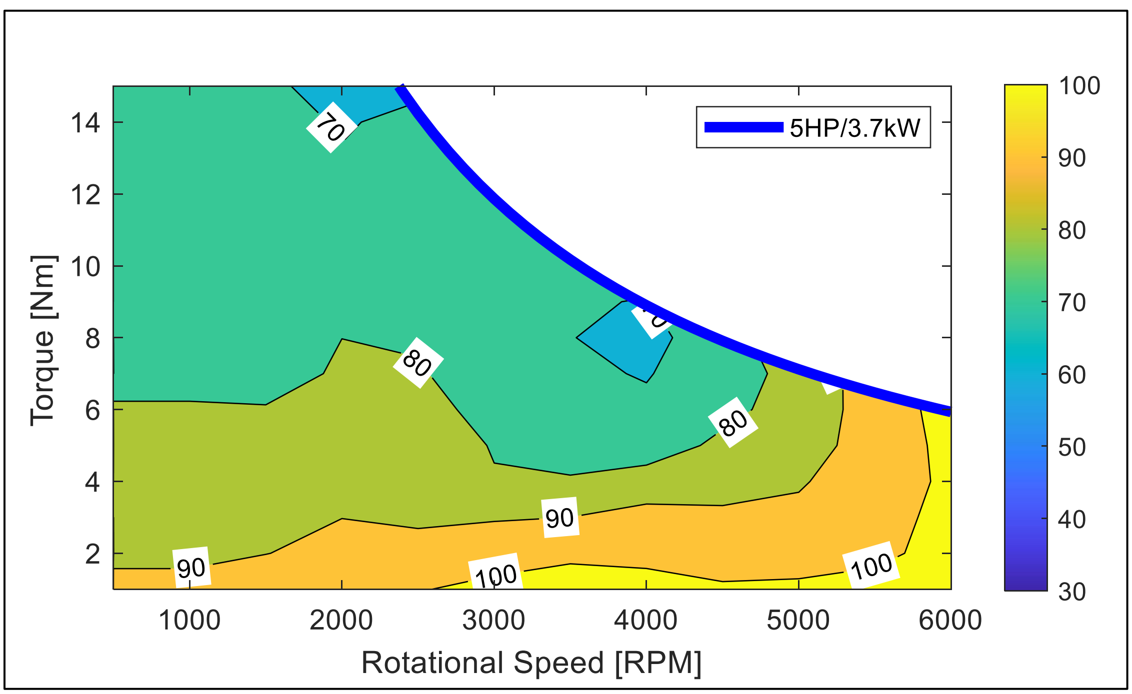

Figure 5.18 Experimental SRM torque ripple contours with $k_{eff-ctrl} = 1$.

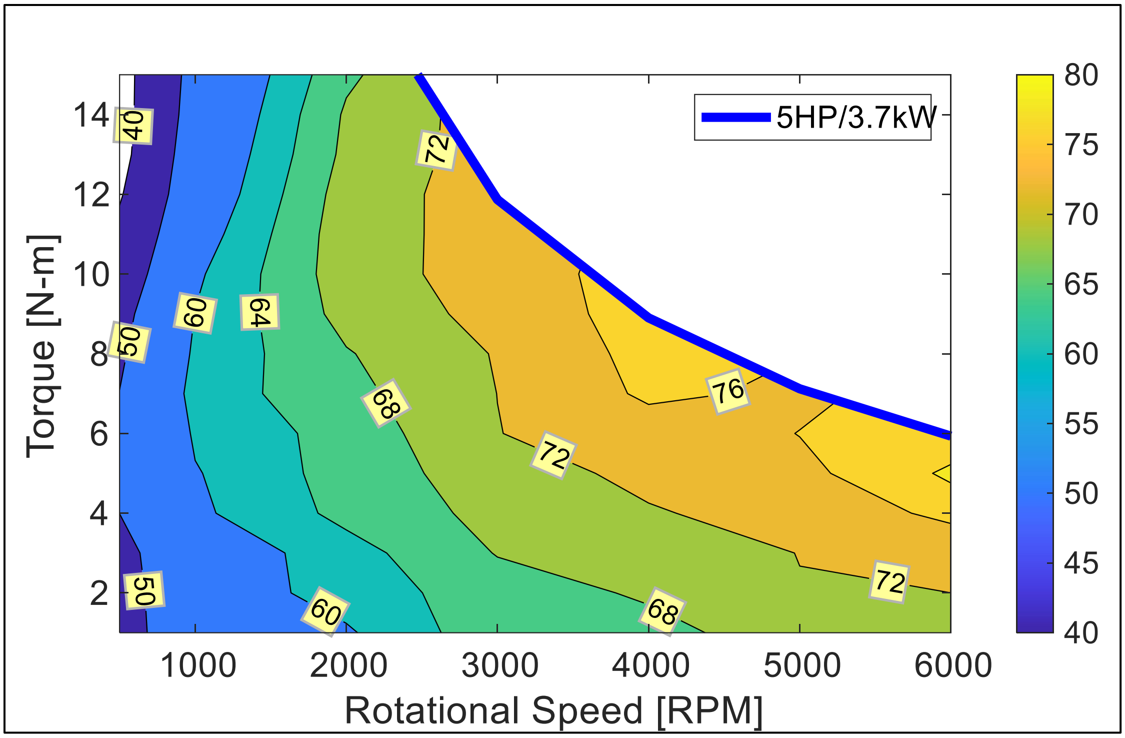

Figure 5.19 Simulated SRM efficiency contours with $k_{eff-ctrl} = 0$.

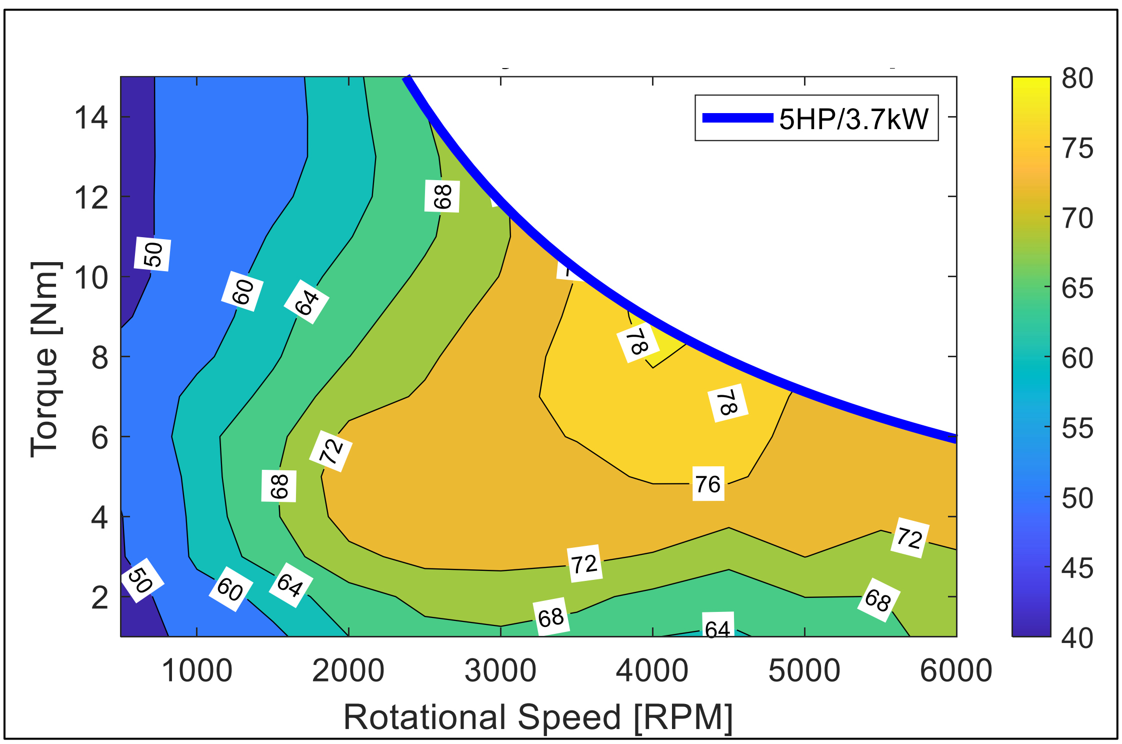

Figure 5.20 Measured SRM efficiency contours with $k_{eff-ctrl} = 0$.

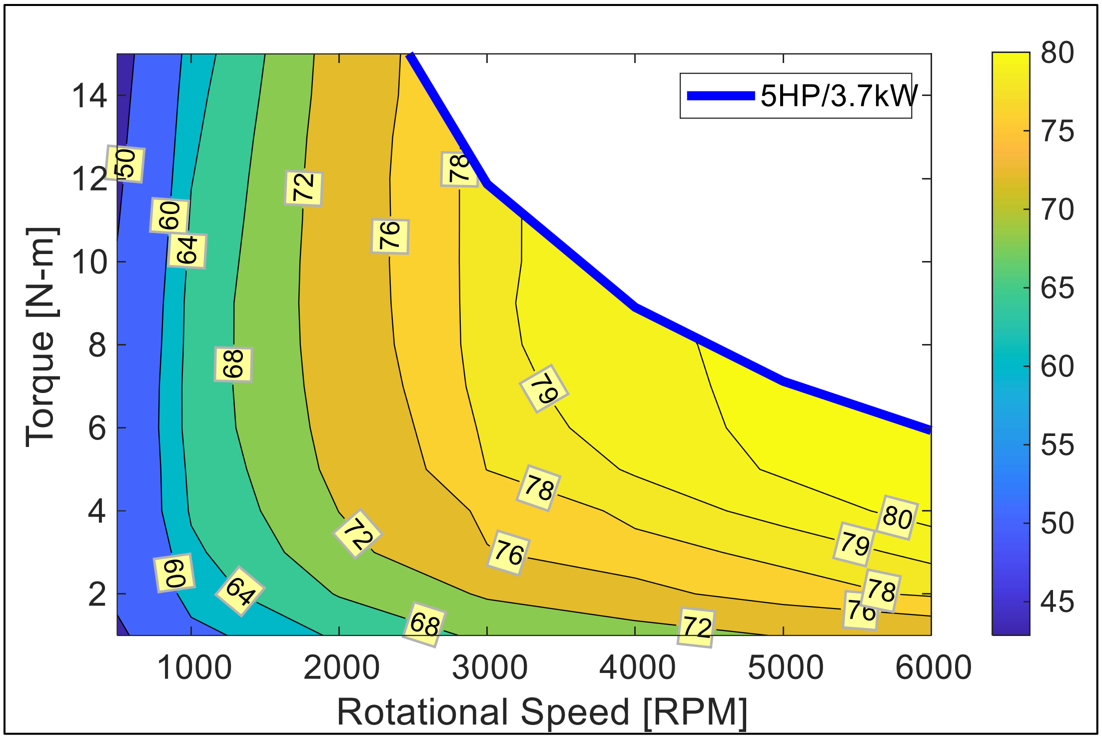

Figure 5.21 Simulated SRM efficiency contours with $k_{eff-ctrl}$ = 1.

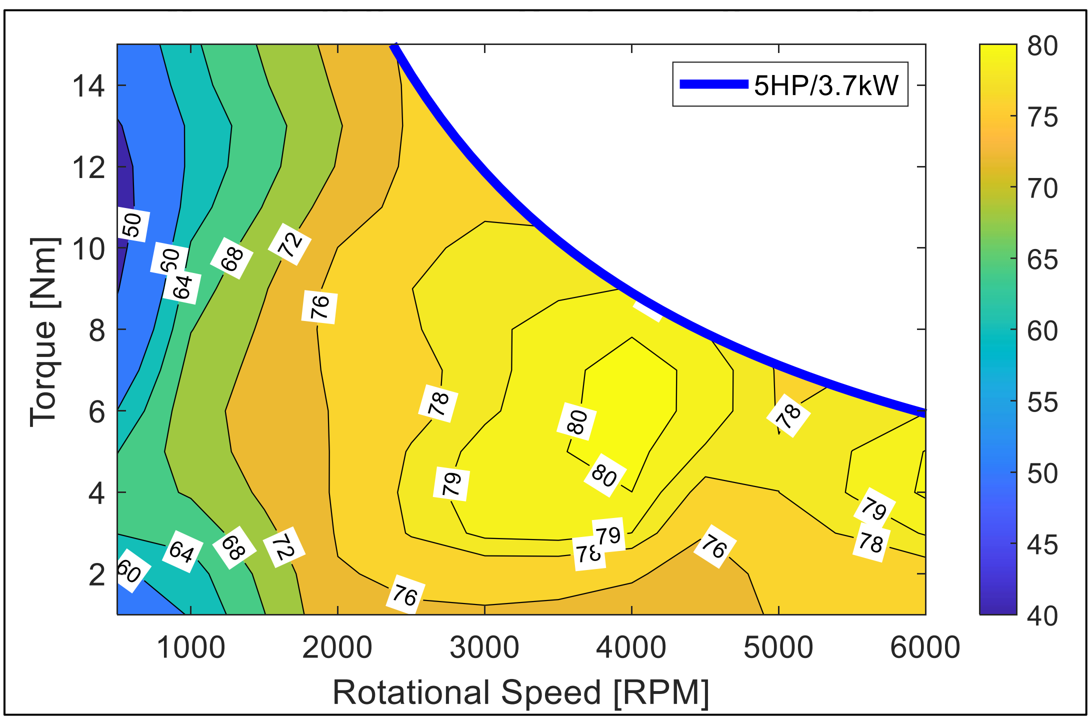

Figure 5.22 Measured SRM efficiency contours with $k_{eff-ctrl}$ = 1.

was confirmed by comparing simulated and empirical results, with experimental torque ripple within 8-15% of simulated torque ripple, and measured efficiency within 3% of simulated efficiency throughout much of the entire operation range. Test results from operation at various torques and speeds confirm the ability to balance design and control conditions with respect to different optimization targets.

References

[5.1] T. Burress, L. M. Tolbert, “Multiple Objective Co-Optimization and Experimental Evaluation of Switched Reluctance Machine Design and Controls,” *IEEE International Electric Machine and Drives Conference*, San Francisco, California, May 15-18, 2023.

CHAPTER SIX: CONCLUSIONS AND FUTURE WORK

Abstract

After a summary and conclusions from the preceding chapters are provided, the applicability and limitations of the proposed approach is discussed. Finally, contributions of this work are listed and suggestions for future work are provided.

Summary and Conclusions

The preceding chapters include an introduction and motivation for this research, a review of SRM design and control optimization methods in the literature, a proposed simulation framework and co-optimization approach, and scaled experimental evaluation to validate the models and demonstrate flexibility in control optimization. The motivation for researching alternatives to PM motors and a review of viable options is provided in Chapter 1. The SRM was chosen as a focus of research based on its low cost, easy manufacturability, moderate performance and efficiency, and its potential for improvement through advanced design and control optimization. Comprehensive comparisons of new and prevalent SRM design and control optimization methods are provided in Chapter 2. It was found that co-optimization of both SRM design and controls is not common, and key areas for improvement in methods for optimizing SRM design and control were identified. Among many things, this includes the need for computationally efficient transient models with the accuracy of FEA simulations and the need for co-optimization of both machine geometry and control methods throughout the entire operation range with multiple objectives such as torque ripple, efficiency, etc.

An optimization framework and multi-stage process is presented in Chapter 3 that includes robust transient simulators that use mappings from FEA in order to optimize SRM geometry, windings, and control conditions throughout the entire operation region with multiple objectives. Custom modeling codes use static finite element analysis (FEA) results to determine optimal current profiles and conventional control conditions for discrete speeds, torques, and torque ripple levels. Transient models rely on torque and flux-linkage lookup tables from 2D FEA to yield a decrease in computation time by a factor of at least 100 times in comparison with 2D transient FEA. This reduction in computational time greatly facilitates broad sweeps of both machine design and control parameters. A method for current profile optimization was proposed that uses particle swarm optimization to determine optimal control waveforms. Further, a general approach was proposed for evaluating the value of any control approach throughout the entire operation range with consideration of various characteristics and boundary conditions such as voltage and current constraints.

The Nissan LEAF primary traction drive electric machine was selected as the baseline reference, and a 12-8 SRM, nominal parameters, fixed parameters, and variable geometric parameters were identified for detailed optimization. In an exemplar implementation of the proposed framework and optimization process, a total of ~900 combinations of geometric parameters including stator tooth width, stator yoke thickness, rotor tooth width, rotor tooth length, and rotor outer diameter were analyzed in the first sweep and down-selections were implemented based on TCD ratio and average torque. Static FEA simulations were performed in Stage 1 at zero-speed conditions to determine an initial solution space, adjust nominal parameters as necessary, and establish a fundamental understanding of the correlation between various geometric parameters and operational quantities such as average torque, torque ripple, and current density. Exemplar performance functions were implemented in Stages 2 and 3 to perform optimization of control conditions and the machine design with weighting factors that allow the designer to balance priorities between torque ripple minimization and efficiency maximization. A design was selected for testing based on performance function evaluation.

The final design was scaled, fabricated, and tested to demonstrate the advantages of the proposed control and design optimization process as tests were conducted with control conditions with different optimization targets. The proposed framework was used to generate control conditions for two sets of tests, one with the optimization target minimum torque ripple and the other targeting maximum efficiency. Accuracy of the models was confirmed by comparing simulated and empirical results, with experimental torque ripple within 8-15% of simulated torque ripple, and measured efficiency within 3% of simulated efficiency throughout much of the operation range. Test results from operation at various torques and speeds confirm the ability to balance design and control conditions with respect to different optimization targets such as torque ripple and efficiency.

Applicability and Limitations of the Proposed Framework and Optimization Process

The proposed framework is particularly applicable when there are stringent design requirements such as high-power density, high-efficiency, minimal torque ripple, and/or minimal acoustic noise. A key consideration in the applicability of the proposed approach is the time associated with mapping. During mapping with magnetostatic 2D FEA, cases were solved in parallel and with 16 parallel solvers, the average solve time for each point was about 10 seconds. Examples of the number of sample points and total simulation time for mapping during Stages 1, 2, and 3 are provided in Table 6.1. Computational times vary with processing power and memory depth, and values in Table 6.1 correlate with that of a mid-range high-performance desktop computer which has 8 cores, 16 processors, and 64 GB of RAM. Additionally, all conditions consider mutual coupling, which involves a variation in multiple currents versus just one. It takes about 3.5 days to generate flux-linkage and torque maps for 1000 geometries as a function of 5 positions and 6 current combinations. A uniformly spaced grid was used during these mappings (labeled as 'Stage 3 Grided' in Table 6.1). The number of cases can likely be reduced significantly by having the map defined by more points in highly non-linear portions of the map and interpolating in more linear areas of the map, and computational time is estimated for this approach (labeled 'Stage 3 Scatted' in Table 6.1).

An example of the number of control conditions that would be needed for a typical control optimization effort in Stage 3 is provided in Table 6.2 for conventional control and for a control optimization approach with iterative solving, each with a total of 9800 and 100,000 cases, respectively. A summary of total solve time (including mapping time) for Stage 3 control optimization efforts is provided in Table 6.3 for 2D FEA and the proposed approach. Once flux-linkage mapping is complete, transient simulation time for the proposed method is much quicker as it takes about 1 second per case, whereas transient FEA takes about 1-3 minutes (an average of about 120 seconds) per case, roughly a factor of at least 100 times longer. It is important to note that the transient FEA software ran on 16 processors, whereas the code used in proposed approach was not parallelized and ran on only 1 processor. The transient code can be parallelized without extensive efforts by having multiple cases solved in parallel (versus parallelizing the solver itself). Two columns are shown for the proposed approach, the one that was implemented in Chapter 4

Table 6.1 Mapping time required for various proposed Stages.

	Stage 1	**Stage 2**	**Stage 3 Gridded**	**Stage 3 Scattered**
	No. of Sample Points For Mapping			
Phase Currents	2	4	10	
Total Currents	8	64	216	25
Positions	5	10	13	13
Total Points	40	640	2808	325
	Map Time			
1 Geometry [Hours]	0.11	1.78	7.8	0.9
10 Geometries [Hours]	1.11	17.78	78	9.03
100 Geometries [Days]	0.46	7.41	32.5	3.76
1000 Geometries [Days]	4.63	74.07	325.0	37.62

Table 6.2 Example of number of control conditions desired for Stage 3 control optimization simulations for different control techniques.

	Conventional Control	**Iterative (e.g. Current Profiling)**
Current or Torque Ref.	20	20
Control variable 1	7	500
Control variable 2	7	
Speeds	10	10
Control Combinations	9800	100000

Table 6.3 Computational time required for various quantities of geometries with 2D Transient FEA, the proposed code with gridded sample points/not parallelized, and proposed code with scattered sample points/parallelized code.

	2D Transient FEA		**Proposed (Gridded, Not Parallelized)**		**Proposed (Scattered, Parallelized)**	
	Conv. Control	**Iterative**	**Conv. Control**	**Iterative**	**Conv. Control**	**Iterative**
1 Geometry [Hours]	326.7	3,333.3	10.5	35.6	1.1	2.6
10 Geometries [Hours]	3,266.7	33,333.3	105.2	355.8	10.7	26.4
100 Geometries [Days]	1,361.1	13,888.9	43.8	148.2	4.5	11.0
1000 Geometries [Days]	13,611.1	138,889.9	438.4	1482.4	44.7	110.0

(‘Gridded, Not Parallelized’), and the other for a scattered mapping and parallelized transient code (‘Scattered, Parallelized’).

The time required (including mapping time) to determine optimal control conditions across the torque-speed region was about 6 hours using the proposed approach, whereas 2D transient FEA would take 327 hours (~14 days). Further, it is estimated that using a scattered mapping approach and parallelized transient code would reduce the total control optimization solve time from 6 hours to 1 hour. With this speed, it is feasible to perform this type of mapping for 100 geometries, in about 4 days. Computational time for the 2D FEA method and the proposed method scales directly with the number of geometries. The plots in Figures 6.1 and 6.2 show the total transient solve time (including mapping) versus the number of control and speed cases for 2D transient FEA and the proposed approach. For case numbers below ~100, transient FEA is the more efficient method when compared with the proposed approach implemented in Chapter 4. However, with scattered mapping and parallelized code, transient FEA only achieves less simulation time if there are only 25 cases or less. Even with conventional SRM control methods, the number of cases required for control optimization is far greater than 100, and therefore the proposed simulation structure is more advantageous regarding total solve time for machine design and control condition optimization. Furthermore, advanced control schemes, such as the proposed current profile optimization for minimal torque ripple, often require iterative simulations to determine optimal control conditions. Overall, it has been demonstrated that this approach has accuracy comparable to that of transient FEA while facilitating large scale design and control co-optimization.

Contributions

Contributions associated with the work described in this dissertation include:

1. A framework that includes an interconnected suite of SRM simulation tools including magnetostatic FEA, transient FEA, mechanical FEA, and the proposed control optimizers that use current fed or voltage fed modeling methods greatly facilitating various types of control and design co-optimization.
2. Flux linkage mapping technique using magnetic vector potential and ampere-turns with post process scaling according winding configuration.

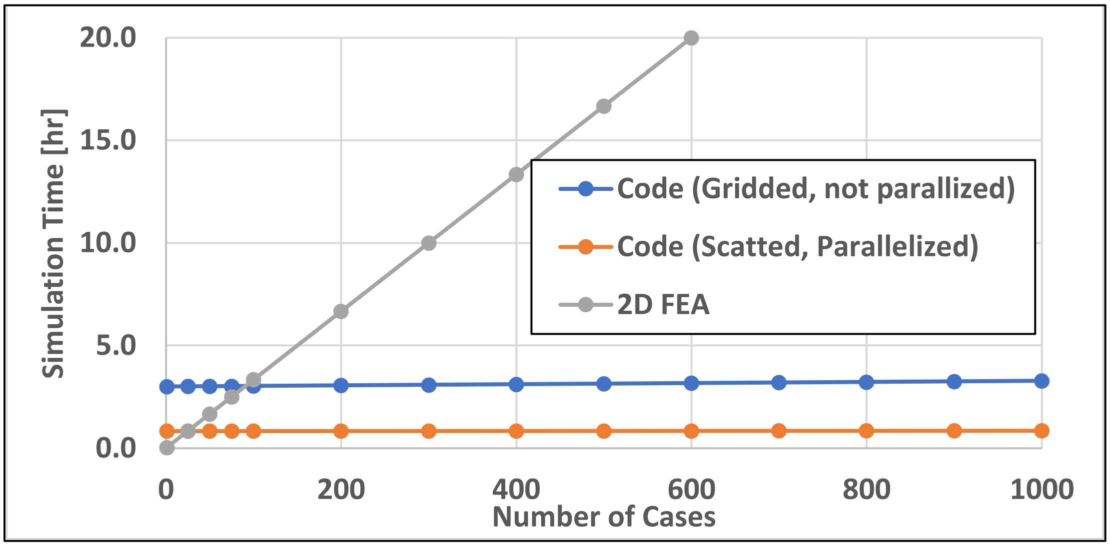

Figure 6.1 Total transient solve time versus moderate number of control and speed cases for transient FEA and the proposed approach.

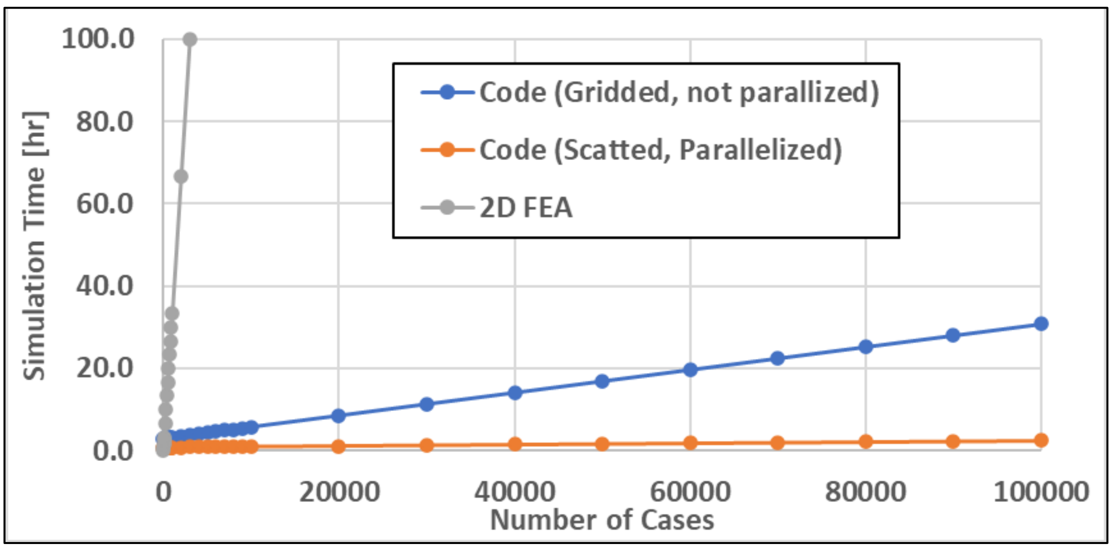

Figure 6.2 Total transient solve time versus large number of control and speed cases for transient FEA and the proposed approach.

3. The use of the torque to current density ratio (“TCD ratio”) and average torque at zero speed and corresponding performance function to indirectly consider impacts of coil cross-sectional area, steel saturation, and winding heat loss in the broad solution space of Stage 1.
4. A current profile optimization technique that uses particle swarm optimization to determine and balance the effectiveness of current profiles regarding torque ripple and efficiency with the consideration of voltage constraints throughout the torque-speed region. One key advantage of this approach is that the PSO code can determine the optimal torque waveform for non-zero torque ripple conditions versus a predefined torque waveform shape that is often assumed in torque ripple minimization schemes such as in torque sharing function methods.
5. Derivation of explicit formulas to determine winding properties including the number of strands in parallel per coil, $N_{strands}$, and the number of turns per coil, N_{turns}, based on assumed and targeted values for slot fill factor, FF, a given wire cross-sectional area, A_{wire}, coil cross-sectional area, A_{coil}, number of parallel branches in a phase, N_{par}, targeted nominal current density, J_0, and phase current rating, $I_{ph.}$
6. A core loss approximation method for the proposed modeling environment using only mapped flux linkages from static electromagnetic FEA sweeps.
7. A systematic design and control optimization method based on weighted fitness functions that provide the ability to balance torque, torque ripple, efficiency, and other metrics throughout the entire operation range for various types of control approaches including conventional control and current profiling methods.
8. A unique design process that involves down-selection steps prior to implementation of a new design and control optimization step allowing a wide range of design parameters to be considered in the initial solution space.

Proposed Future Work

Items recommend and being considered for future work include:

1. Improved core loss approximation using spatial-based flux mapping during flux linkage and torque mapping. While the proposed loss calculation method for stator and rotor back-iron losses closely matched transient FEA, some error was observed in tooth loss calculations as the mapped flux linkage did not capture localized flux density transients that occur near the

interface of stator and rotor teeth. To address these issues, a spatial-based mapping technique is proposed that maps flux density on a basis that is more coarse than the base mesh, but enough detail to represent localized rotating vectors and other anomalies.

2. Acoustic noise mitigation using the proposed framework. The initial mapping required for acoustic noise modeling was demonstrated in Chapter 4, as radial forces were mapped during 2D magnetostatic simulations and mechanical deformation, and stiffness were determined for each geometry using mechanical FEA. Using the mechanical stiffness, mapped forces, and other system physical properties, sound power calculations can be implemented during Stage 3 and acoustic noise mitigation can be achieved through co-optimization of both design and control in a similar manner in which torque ripple was minimized in Chapter 4.

VITA

Timothy Burress received B.S. and M.S. degrees in electrical engineering from The University of Tennessee, Knoxville, TN, USA, in 2004 and 2006, respectively. From 2004 to 2006, he was a Research Assistant at Oak Ridge National Laboratory (ORNL). Since 2006, he has been a Research and Development Staff member leading and supporting electric machine design, fabrication, and comprehensive testing of motors for transportation, defense, and other applications. He also specializes in the development and implementation of hardware and software for robust motor feedback control systems. Mr. Burress is a Senior IEEE member and currently serves as Working Group Chair of the IEEE Industry Applications Society (IAS) and Power Electronics Society (PES) Working Group for the development of Standard 11, the IEEE Standard for Rotating Electric Machinery for Rail and Road Vehicles.